

FUNDAMENTAL UNDERSTANDING OF SURFACE CHARACTERISTIC AND
CHROMIUM CONTAMINATION ON SOLID OXIDE FUEL CELL CATHODES

By

DONGJO OH

A DISSERTATION PRESENTED TO THE GRADUATE SCHOOL
OF THE UNIVERSITY OF FLORIDA IN PARTIAL FULFILLMENT
OF THE REQUIREMENTS FOR THE DEGREE OF
DOCTOR OF PHILOSOPHY

UNIVERSITY OF FLORIDA

2010

© 2010 Dongjo Oh

To my parents; wife, Chanyoung; and daughter, Narae

ACKNOWLEDGMENTS

I would like to thank my advisor, Dr. Eric Wachsman for his support and guidance throughout this experience. I really appreciate the opportunity that he has provided me. I also would like to thank Dr. Juan Nino, Dr. Susan Sinnott, Dr. Scott Perry, and Dr. Mark Orazem for their advice and participation as my committee member. I acknowledge Dr. Hee Sung Yun and Dr. Jiho Yoo for sharing their invaluable experience and guiding me toward a critical thinking and fundamental understanding of materials. Finally, my wife, Chanyoung, I always appreciate your support and generosity. You and our baby, Narae are the greatest gift for me that Jesus has sent to me.

TABLE OF CONTENTS

	<u>page</u>
ACKNOWLEDGMENTS.....	4
LIST OF TABLES.....	8
LIST OF FIGURES.....	9
LIST OF ABBREVIATIONS	14
ABSTRACT.....	16
CHAPTER	
1 INTRODUCTION	18
1.1 Dual Challenges of Energy and Climate Change.....	18
1.2 Solid Oxide Fuel Cell (SOFC)	18
1.3 Objectives	19
2 BACKGROUND	21
2.1 Basic Components and Operation Principle of SOFC	21
2.2 SOFC Performance	22
2.2.1 Equilibrium Voltage	22
2.2.2 Activation Overpotential	23
2.2.3 Ohmic Overpotential	25
2.2.4 Concentration Overpotential	26
2.2.5 Other Losses	29
2.3 Efficiency and Degradation	29
2.4 Overview of Cathode	31
2.4.1 Requirements	31
2.4.2 Oxygen Reduction Process	31
2.4.3 Mixed Ionic Electronic Conductor	32
2.4.4 $\text{La}_{1-x}\text{Sr}_x\text{Co}_y\text{Fe}_{1-y}\text{O}_{3-\delta}$ (LSCF)	34
2.5 Summary.....	35
3 EXPERIMENTAL	45
3.1 Electrical Conductivity Relaxation	45
3.1.1 Theoretical Background	45
3.1.2 Electrical Conductivity Measurement	48
3.1.3 Effect of Surface Roughness	48
3.2 Electrochemical Impedance	49
3.3 Temperature Programmed Isotopic Exchange.....	50
3.4 Materials Characterizations	51

4	MECHANISTIC UNDERSTANDING OF LSCF DEGRADATION	57
4.1	Introduction	57
4.2	Experimental	57
4.2.1	Sample preparation	57
4.2.2	Heat treatment.....	58
4.2.3	Characterization	58
4.3	Results and Discussion	60
4.4	Conclusions	67
5	IMPACT OF CO IMPREGNATION INTO LSCF CATHODE ON SOFC PERFORMANCE	74
5.1	Introduction	74
5.2	Experimental	75
5.2.1	AC Impedance Analysis	75
5.2.2	Electrical Conductivity Relaxation	76
5.2.3	Button Cell Fabrication and Tests	77
5.2.4	Catalyst Impregnation	79
5.2.5	Characterization	79
5.3	Results and Discussion	79
5.3.1	Effect of Co Impregnation on Electrode Impedance	79
5.3.2	Effect of Co Impregnation on Power Density of a Single Cell	81
5.3.3	Characteristic Dependence of Kchem on Oxygen Partial Pressure	83
5.4	Conclusions	85
6	MECHANISM OF CR VAPOR DEPOSITION ON SOFC CATHODES.....	94
6.1	Introduction	94
6.2	Experimental	95
6.2.1	Sample Preparation	95
6.2.2	Heat Treatment	96
6.2.3	Characterization	96
6.3.	Results and Discussion	97
6.3.1	XRD	97
6.3.2	Cr Vapor Deposition on LSCF	97
6.3.3	Dependence of A-site ions on Cr Vapor Deposition	101
6.3.4	Dependence of B-site ions on Cr Vapor Deposition	103
6.4.	Conclusions	107
7	DEGRADATION MECHANISM AND THEIR IMPACT ON OXYGEN REDUCTION KINETICS OF LSCF	117
7.1.	Introduction	117
7.2.	Experimental	117
7.2.1	AC Impedance.....	117
7.2.2	Electrical Conductivity Relaxation	118

7.2.3	Temperature Programmed Isotopic Exchange (TPX)	119
7.2.4	Characterization	120
7.3	Results and Discussion	120
7.3.1	AC Impedance.....	120
7.3.2	Electrical Conductivity Relaxation	121
7.3.3	Temperature Programmed Isotopic Exchange	123
7.3.4	Post ECR Characterization	126
7.4	Conclusions	128
8	VAPORIZATION OF DOPED ALKALINE EARTH METAL OXIDE	137
8.1	Introduction	137
8.2	Experimental	138
8.3	Results and Discussion	138
8.4	Conclusions	140
9	CONCLUSIONS.....	145
APPENDIX		
A	THEORETIC EQUILIBRIUM VOLTAGE.....	147
B	MEASUREMENT EFFECT OF NON-IDEAL STEP CHANGE IN ECR.....	149
C	MEASUREMENT OF THE SURFACE SENSITIVE RATE COEFFICIENT USING ISOTHERMAL ISOTOPIC SWITCHING.....	152
C.1	Introduction	152
C.2	Background.....	153
C.3	Experimental	154
C.4	Results and Discussion	155
C.5	Conclusions	157
D	TAPE CASTING SLURRY COMPOSITION.....	161
E	CR CONTAMINATION ON LSM82.....	162
F	K_{chem} and D_{chem} at 750C	163
G	SURFACE VARIATION OF LCCF AND LBCF.....	165
H	COBALT OXIDE DISPERSION ON LSCF SURFACE.....	166
	LIST OF REFERENCES.....	167
	BIOGRAPHICAL SKETCH.....	175

LIST OF TABLES

<u>Table</u>	<u>page</u>
3-1 List of instruments for material characterizations.....	56
5-1 Thermodynamic factors and $(3-\delta)/\delta$ of LSCF values at 800°C. ^{52, 94}	93
5-2 Characteristic dependencies of the apparent rate coefficients on pO_2 . ⁹⁵	93
6-1 Summary of tested ABO_3 perovskite materials	115
6-2 Chemical composition of Crofer22APU	115
6-3 Elemental atomic percents (%) of LSCF after heat treatment at 800°C for 50 hrs in the presence of Crofer22APU obtained using EDS.....	115
6-4 AES atomic percents of LSCF after heat treatment(HT) at 800°C for 50 hours	115
6-5 Elemental atomic percents of non-heat treated and heat treated samples*	116
7-1 Samples tested in TPX.....	136
7-2 Elemental atomic percents (%) of LSCF obtained using EDS	136
7-3 Elemental atomic percents (%) of LSCF after ECR test at 800°C for 400 hours obtained using AES	136
A-1 Thermodynamic properties at 298.15K and 1bar.....	148
D-1 Tape casting slurry composition.	161

LIST OF FIGURES

<u>Figure</u>	<u>page</u>
2-1 Schematic diagram of the cross section of a planar type SOFC.....	37
2-2 Typical current density and voltage characteristic of SOFC. j_L is the limiting current density. ⁴³	37
2-3 Contribution of chemical and electrical potential gradients to the equilibrium state at the electrochemical system.	38
2-4 The electrochemical energy change from equilibrium state as a result of applying activation overpotential.	39
2-5 Activation overpotential (η_{act}) as a function of current density and the effect of exchange current density (j_o) on activation overpotential.	40
2-6 Schematic diagram of the cross section for (a) electrolyte and (b) anode supported cell.	40
2-7 (a) Sketch of a diffusion layer between free stream and electrode and (b) concentration profiles across a diffusion layer at steady state. ¹⁰	41
2-8 Plot of concentration overpotential (η_{con}) as a function of current density.	41
2-9 The efficiency (ϵ) and fuel utilization curve of an SOFC as a function of cell voltage (E_{cell}) at 800°C. ²⁰	42
2-10 Active reaction sites (painted in red) for oxygen reduction. (a) Pure electronic conductors and (b) mixed ionic and electronic conductors. ²³	42
2-11 Unit cell of pseudo cubic perovskite of ABO_3 perovskite	43
2-12 Surface exchange coefficients of $La_{0.7}Ca_{0.3}CrO_{3-\delta}$ as a function of mole fraction of oxygen vacancy. ³⁰	43
2-13 Effect of B site transition metals on $La_{0.7}Sr_{0.3}BO_3$ cathode over potential. ⁴⁴	44
2-14 Oxygen nonstoichiometry (δ) of different LSCF composition as a function of temperature. ⁴⁵	44
3-1 Sample dimension and electrical connection between the sample and Lock in Amplifier.	53
3-2 Schematic of the effect of a rough surface on the boundary conditions.	53
3-3 The effect of roughness on the measurement of D_{chem} and K_{chem} (top), and surface roughness and actual surface area of samples (bottom).	54

3-4	Nyquist plot of an RC circuit.....	54
3-5	Core shell ionization and subsequent de-excitation via (c) Auger process and (d) characteristic X-ray emission. ⁵⁸	55
3-6	Schematic diagram of escape depth of Auger electron and characteristic X-ray. ⁵⁸	55
4-1	Brief description of sample preparation procedure.	68
4-2	Heat treatment set-up.	68
4-3	SEM micrographs of LSCF of (a) before heat treatment and after heat treatment at (b) 600°C, (c) 700°C, (d) 800°C and (e) 900°C for 50 hours in the absence of Fe-Cr alloy.....	69
4-4	Magnified images of the precipitates on LSCF surfaces after heat treatment at (a) 900°C for 50 hours, (b) 900°C for 50hours,(c) 860°C for 100 hours, and (d) 890°C for 100 hours.....	70
4-5	Differentiated Auger electron spectra of the (a) La _{MLL} , (b) Sr _{LMM} , (c) Co _{LMM} , (d) Fe _{LMM} , and (e) O _{KLL} before(blue solid line) and after (red dotted line) heat treatment at 800°C for 50 hours.	71
4-6	TEM bright field image of the cross section of precipitate (left side) and EDS line scan of selected elements (right side)	71
4-7	SEM micrographs of LSCF surfaces after heat treatment for 50 hours at (a) 800°C/ N ₂ , (b) 800°C/0.1% O ₂ (c) 890°C/N ₂ and (d) 890°C/0.1% O ₂	72
4-8	Schematic diagram of (a) the formation of oxygen vacancies and (b) formation of cation and anion vacancies simultaneously.	72
5-1	Sketch of deposition of nano size particles on cathode surface via wet impregnation.....	86
5-2	Schematic of AC impedance measurements.	86
5-3	Equivalent circuit to fit the measured impedance data.	87
5-4	Current density and voltage measurement setup	87
5-5	AC Impedance spectra of LSCF/GDC/LSCF symmetric cell.....	88
5-6	Impedance plots for symmetric cell of plain LSCF electrode and Co impregnated LSCF electrode at 800°C in air.	88
5-7	Comparison of total electrode ASRs as a function of temperatures	89

5-8	Measurement of cell voltage as a function current density at (a) 600°C, (b) 550°C and (c) 500°C. (d) Maximum power densities as a function of temperatures.	90
5-9	Impedance of a button cell for plain LSCF and Co impregnated cathode at 600°C	90
5-10	The area specific resistance of electrode and electrolyte for plain and Co impregnated LSCF cathode cells.	91
5-11	(a) SEM micrograph of LSCF/GDC/Ni-GDC button cell and (b) magnified images of Co impregnated LSCF after cell test.	91
5-12	(a) D_{chem} and K_{chem} , (b) D_{self} and K_o , and (c) D_v at 800°C as a function of pO_2	92
6-1	Schematic of experimental design for heat treatment.	109
6-2	XRD patterns of tested perovskite materials	109
6-3	Surfaces of LSCF (a) before and (b-d) after heat treatment in the presence of Crofer22APU at 800°C 50 hrs. The leading edge distances between LSCF and Crofer22APU sheets were (b) direct contact, (c) 0.1 cm, and (d) 0.5 cm. All images are the same scale.....	110
6-4	XRD patterns of fresh and heat treated LSCF on Crofer22APU sheet at 800°C for 50hours. (b ~ d) Enlarged patterns for better comparison. * is the XRD pattern measured using a low angle mode.	111
6-5	Surfaces of LCCF, LBCF, LSCF and SCF after heat treatment in the presence of Crofer22APU at 800°C for 50 hours. The leading edge distances between samples and Crofer22APU sheet were 0.1 cm and 0.5 cm for the left and right hand sides, respectively.	112
6-6	Surfaces of tested after heat treatment in the presence of Crofer22APU at 600°C and 400°C (Leading edge distance 0.1 cm).....	113
6-7	SEM micrographs of LSM surfaces of (a) before and (b) after heat treatment at 800°C for 50 hours in the presence of Crofer22APU (Leading edge distance 0.1 cm).	113
6-8	(a) SEM micrograph of LSM after heat treatment in the presence of Crofer22APU at 1050°C for 50 hours, and EDS spectra for (b) the flat region and (c) particle (Leading edge distance 0.1 cm).....	114
7-1	Equivalent circuit to fit the measured impedance data	130

7-2	(a) A schematic of the experimental set up used for temperature programmed isotopic exchange and (b) the pre-heat treatment and measurement conditions	130
7-3	AC Impedance spectra of LSCF/GDC/LDCF in air at 800°C.....	131
7-4	Area specific resistance of LSCF at 800°C in air as a function of aging time (a) in the (a) presence and (b) absence of K type thermocouple in the reactor.....	131
7-5	(a) Normalized electrical conductivity relaxation curve after switching oxygen partial pressure from 43 to 67% at t =0 and (b) variation of relaxation curves with aging at 800°C.....	132
7-6	Degradation of Kchem and Dchem in Cr contaminated environment at 800°C	132
7-7	Effect of total surface area on oxygen exchange profiles which are measured by TPX. SA refers to the surface area.....	133
7-8	TPX result of heat treated LSCF at 800°C for 400 hours with and without exposure to Crofer22APU in comparison to fresh LSCF.....	134
7-9	SEM micrographs of polished LSCF surfaces (a) before and (b) after ECR at 800°C for 400 hours.	135
8-1	Schematic of experimental set up.	142
8-2	SEM micrographs of (a) as-polished and (b) heat treated LSCF in the presence of Crofer22APU.....	142
8-3	(a) LSM surface after heat treatment at 1050°C for 50 hours in the presence of Crofer22APU sheet. EDS spectra for (b) the newly formed particle after heat treatment and (c) as polished LSM sample.	143
8-4	(a) Surface of LSM after heat treatment at 800°C for 50 hours in the presence of BaO powder and Crofer22APU. (b) Spot mode EDS spectra for the particle.	144
B-1	Reactor flush time measurement set up using mass spectrometer. The flow from ECR to mass spec was limited to 30 sccm by the ball flow meter.....	150
B-2	Measured reactor flush time using mass spectrometer (a) and a fit using Eq B-3 (b).....	151
C-1	Time dependent relaxation profile of normal oxygen (^{16}O), oxygen isotope (^{18}O) and scrambled oxygen ($^{16}\text{O}+^{18}\text{O}$) at 700°C.....	158

C-2	Normalized concentrations of desorbed oxygen from the sample and incorporated oxygen.....	158
C-3	K_{chem} measured by ECR in this study and literatures ^{52, 94} , converted using the thermodynamic factor, at 800°C.....	159
C-4	Normalized relaxation curves of incorporated oxygen isotope at different temperatures.....	159
C-5	Arrhenius plot of surface exchange coefficient ($pO_2= 0.01$).....	160
E-1	(a) As-polished LSM82 surface and (b) heat treated LSM82 at 800°C for 50hrs in the presence of Crofer22APU.....	162
F-1	D_{chem} and K_{chem} at 750°C as a function of pO_2	163
F-2	Degradation of K_{chem} at 750°C.....	164
G-1	Differentiated Auger electron spectra for pre (blue) and post (red) heat treated samples at 800°C for 50 hrs. (a) LCCF and (b) LBCF.....	165

LIST OF ABBREVIATIONS

AES	Auger electron spectroscopy
AFM	Atomic force microscopy
ASR	Area specific resistance
BET	Brunauer, Emmett, and Teller surface area measurement
BOP	Balance of Plant
DPB	Di-n butyl phthalate
ECR	Electrical conductivity relaxation
EDS	Energy dispersive spectroscopy
FIB	Focused Ion beam
GDC	Gd ₂ O ₃ doped CeO ₂
LBCF	La _{0.6} Ba _{0.4} Co _{0.2} Fe _{0.8} O ₃
LCCF	La _{0.6} Ca _{0.4} Co _{0.2} Fe _{0.8} O ₃
LSCF	La _{0.6} Sr _{0.4} Co _{0.2} Fe _{0.8} O ₃
LSM	La _{0.6} Sr _{0.4} MnO ₃
MIEC	Mixed ionic and electronic conductor
PEG	Polyethylene glycol
PVB	Polyvinyl butyral
SCF	SrCo _{0.2} Fe _{0.8} O ₃
SECA	Annual solid state energy conversion alliance
SEM	Scanning electron microscopy
SOFC	Solid oxide fuel cell
TEM	Transmission electron microscopy
TPB	Three phase boundary
TPX	Temperature programmed isotopic exchange

XRD	X-ray diffraction
YSZ	Y ₂ O ₃ stabilized ZrO ₂
ΔpO_2	Oxygen partial pressure gradient
η_{act}	Activation overpotential
η_{con}	Concentration overpotential
η_{ohm}	Ohmic overpotential

Abstract of Dissertation Presented to the Graduate School
of the University of Florida in Partial Fulfillment of the
Requirements for the Degree of Doctor of Philosophy

FUNDAMENTAL UNDERSTANDING OF SURFACE CHARACTERISTIC AND
CHROMIUM CONTAMINATION ON SOLID OXIDE FUEL CELL CATHODES

By

DONGJO OH

May 2010

Chair: Eric. D Wachsman

Major: Materials Science and Engineering

A solid oxide fuel cell (SOFC) is a highly efficient and environmental-friendly energy conversion device. But the progress toward commercialization continues to be a slow struggle mostly due to high operation temperatures (800~1000°C). Lowering operation temperatures can bring manufacturing costs down and provide high conversion efficiency, and less difficulty in sealing and heat management. However, substantial increase in internal losses, especially activation overpotential, lowers SOFC performance with reduced operation temperatures. Because the activation overpotential is mostly attributed to the oxygen reduction reaction (ORR) on the cathode, tremendous works have been done in order to improve the cathode performance and understand the ORR mechanisms and degradation mechanisms.

A heterogeneous reaction is primarily affected by the interaction between surface and adsorbed species. Therefore, the surface composition and structure are one of the most important factors affecting the cathode performance. Nevertheless, compositional and structural variations of cathode surfaces at high temperatures have not gained much attention. The objective of this study is, firstly, to better understand the surface

structure of cathode materials at high temperatures, and, secondly, to improve the SOFC cathode performance based on this knowledge.

$\text{La}_{0.6}\text{Sr}_{0.4}\text{Co}_{0.2}\text{Fe}_{0.8}\text{O}_3$ has been widely used for SOFC cathodes. Chemical and structural variations of $\text{La}_{0.6}\text{Sr}_{0.4}\text{Co}_{0.2}\text{Fe}_{0.8}\text{O}_3$ (LSCF) surfaces under oxidizing environment were investigated. Cr contamination free LSCF showed the formation of submicron-sized SrO_x precipitates on the grain surface. This caused the reduced concentration of transition metals in B sites. The addition of cobalt oxide on the surface of LSCF was found to improve the cathode performance.

In contrast, Cr vapor deposition caused the formation of larger SrCrO_4 particles on the LSCF surface along grain boundaries, and Sr-deficient matrix. The structural analysis identified the phase transition from rhombohedral to cubic perovskite in due to Sr deficiency. A defect chemistry model was presented based on observed phenomena. Electrical conductivity relaxation, AC impedance spectroscopy and temperature programmed isotopic exchange (TPX) were conducted to study the impacts of Cr contamination on the cathode performance.

It was found that Cr contamination was a chemical process for Co-Fe based materials and an electrochemical process for Mn based materials. Unstable Co^{4+} and Fe^{4+} lead to the formation of a nucleation agent for the chemical reaction. By contrast, stable Mn^{4+} does not lead to the formation of a nucleation agent. At last, a new hypothesis for the vaporization of Sr from $\text{La}_{0.6}\text{Sr}_{0.4}\text{Co}_{0.2}\text{Fe}_{0.8}\text{O}_{3-\delta}$ (LSCF) was proposed based on previous observations, and the evidence for Sr vaporization was provided.

CHAPTER 1 INTRODUCTION

1.1 Dual Challenges of Energy and Climate Change

The development of clean and sustainable energy sources has recently gained speed due to increased worldwide attention on decreasing oil supplies and climate change.¹⁻³ Due to the potential worldwide impact from these problems, global efforts are required. For example, there was an historic *Summit on Climate Change* in Copenhagen in December 2009. 115 world leaders participated in the summit and recognized the catastrophic impacts of climate change. The summit, however, ended in failure without a strong agreement to reduce green house gas emission because of the conflict of national interests. Decades of activities of wealthy countries are most likely responsible for current climate change while the impacts from the regulations of green house gas emission are more profound for poor countries. Green house gas emissions are closely tied to national economic growth. Poor countries do not want to kick away the ladder to reach wealthy countries by reducing emissions. Political efforts are the best option to slow down the momentum for global warming in the short term. Long-term solutions will require the development of clean and sustainable energy technology.

1.2 Solid Oxide Fuel Cell (SOFC)

A fuel cell is an energy conversion device that converts chemical fuels directly into electrical energy, thus providing high efficiency and reduced emission of pollutants, including green house gases.⁴⁻⁸ In addition, the absence of moving parts allows quiet operation and long life times. The fuel cell is different from the rechargeable battery since its size can range from small to large and it can be recharged quickly by refueling. There are various fuel cell types such as polymers, aqueous alkalis, phosphoric acids,

molten carbonates, and solid oxides. The solid oxide fuel cell (SOFC), which uses a solid oxide electrolyte, are marked by fewer problems in electrolyte management, extended life time, highest efficiencies, low materials costs, fuel flexibility, and a high grade of waste heat.^{9, 10} The SOFC has a high potential for application in stationary power plants and auxiliary power units of vehicles.

There have been several successful demonstrations.^{6, 11} However, the progress toward a commercialization of the SOFC is a slow struggle. One of the biggest hurdles is high manufacturing costs. The high cost of SOFC stack is in part due to high operating temperatures. SOFCs operate at higher temperatures than the other types due to the solid oxide electrolyte, which leads to high material costs. The cost breakdown model shows that the SOFC stack is the one of the major components, while the remaining balance of plant (BoP) equipment such as fuel and air supply and power electronic control system holds a minor share of the manufacturing cost.¹² Below 800°C LaCrO₃ based ceramic interconnects, which contributes over 80% of material cost for the stack, can be replaced with cheaper metallic interconnects.¹³ Furthermore, reduced operation temperatures improves thermodynamic conversion efficiency for reformed gas and improves the sealing and heat management situation.⁹ However, a rapid decrease in SOFC performance must be overcome in order to reduce operation temperatures.

1.3 Objectives

A heterogeneous reaction is primarily determined by interaction between surface and gas phases. As a result, surface chemical composition is an important factor affecting the oxygen reduction reaction on cathodes. The chemical composition of metal oxide surfaces may significantly differ from that of a bulk due to broken bonding at the

surface. The chemical variation of the surface of $\text{La}_{0.6}\text{Sr}_{0.4}\text{Co}_{0.2}\text{Fe}_{0.8}\text{O}_{3-\delta}$ (LSCF), which has been widely used for intermediate temperature (600-800°C) range SOFCs, was investigated. It was found that the catalytically inactive elements tended to segregate to the surface or near-surface region under oxidizing condition. Based on these results, additional catalyst material was dispersed on the surface by impregnation and the effect was examined.

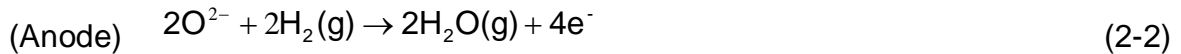
In the meanwhile, utilization of metallic interconnects is advantageous for cost reduction. However, most interconnects contain high concentration of Cr (10~30%) and out-diffused Cr is known to be evaporated into CrO_3 or $\text{CrO}_2(\text{OH})_2$ at high temperatures under oxidizing conditions.¹⁴ As these Cr vapor species are transported into the cathode or electrolyte, they may affect the catalytic activity of cathodes. This study investigated the effect of Cr contamination on the performance of $\text{La}_{0.6}\text{Sr}_{0.4}\text{Co}_{0.2}\text{Fe}_{0.8}\text{O}_3$ cathode, and the reaction mechanism between cathodes and Cr vapor species in order to provide fundamental knowledge on the long term stability of SOFC.

CHAPTER 2 BACKGROUND

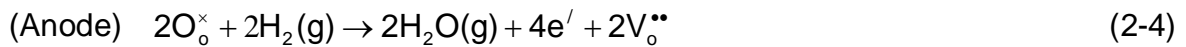
2.1 Basic Components and Operation Principle of SOFC

The basic components of a single cell are a cathode, anode, and electrolyte as described in Figure 2-1. The solid state electrolyte is a pure ionic conductor, which spatially separates air from fuel gases and prevents direct combustion between them. The cathode and anode refer to the electrodes where oxygen is reduced into oxygen ions and hydrogen is oxidized into water vapor in combination with oxygen ions, respectively. While the electrolyte must be dense, the two electrodes are porous in order to increase reaction areas and improve mass transport of reactants.

The overall reaction for the SOFC is spontaneous. Once oxygen and fuel gases are delivered to the anode and cathode, respectively, there is a net chemical driving force for oxygen transport due to an oxygen partial pressure gradient (Δp_{O_2}) across the electrolyte. Provided that hydrogen is used as a fuel, the two electrochemical half reactions taking place at the cathode and anode are



Or by using the Kröger-Vink notation,¹⁵



where $V_o^{\bullet\bullet}$ represents the oxygen vacancies in the lattice and O_o^{\times} represents the oxygen anions in regular oxygen anion sites. The overall reaction is



The internal flow of oxygen ions through the electrolyte must be balanced by the flow of electronic charge through an external circuit, providing useful work.

2.2 SOFC Performance

2.2.1 Equilibrium Voltage

Theoretical thermodynamics limits the maximum voltage that a single cell can produce. The chemical free energy change (ΔG) during the overall reaction in Eq. 2-5 is

$$\Delta G_{\text{Rxn}} = \sum G_{\text{Product}} - \sum G_{\text{Reactant}} = 2G_{\text{H}_2\text{O}(\text{g})} - 2G_{\text{H}_2(\text{g})} - G_{\text{O}_2(\text{g})} \quad (2-6)$$

where G is the chemical energy of corresponding species. Under a non-standard state, G can be written as

$$G = G^\circ + R \cdot T \cdot \ln p \quad (2-7)$$

G° is the chemical energy at standard state, R is the gas constant, T is the absolute temperature, and p is the pressure. The chemical energy change is associated with electrical energy by

$$E = n \cdot F \cdot \Delta G \quad (2-8)$$

where E is the voltage, n is the number of electron transferred during the reaction, and F is Faraday's constant. Thus the equilibrium voltage (E_{Eq}) can be written as¹⁶

$$E_{\text{Eq}} = E_T^0 - \frac{RT}{nF} \ln \left(\frac{p_{\text{H}_2\text{O}}^2}{p_{\text{O}_2} \cdot p_{\text{H}_2}^2} \right) \quad (2-9)$$

where E_T^0 is the voltage at standard state and temperature T , and T is the absolute temperature. Eq. 2-9 is known as the Nernst equation. E_{Eq} has been also called Nernstian voltage or open circuit voltage (OCV). At 800°C, the equilibrium voltage of a single cell is approximately 1.13 V (Appendix A).

At equilibrium, the SOFC produces the maximum output voltage but no current. The cell voltage starts to decrease from the equilibrium voltage as the current density increases due to losses from internal cell resistances. Figure 2-2 summarizes the theoretic behavior of the current density and voltage. The key performance of an SOFC is given by its power density, which is how much electrical energy an SOFC can produce per unit time and unit area. There are four major internal losses: the activation overpotential (η_{act}), the ohmic overpotential (η_{ohm}), the concentration overpotential (η_{con}), and the loss (E_L) due to the partial electronic conductivity of electrolytes or imperfect gas sealing. The output voltage measured (V) can be written as

$$V = E_{Eq} - \eta_{act} - \eta_{ohm} - \eta_{con} - E_L \quad (2-10)$$

In the following section, the nature of internal losses is explained.

2.2.2 Activation Overpotential

Activation overpotential is attributed to the limit of electrode reaction kinetics. Even though the reaction is spontaneous ($\Delta G_{Rxn} < 0$), the rate is finite because of the activation barrier (E_A). Only species that have gained sufficiently high energies to overcome the activation threshold are able to jump to the next state as Figure 2-3a describes.¹⁷

According to statistical thermodynamics, the probability of finding a species (P) in the activated state at temperature T is given by

$$P = e^{-\frac{E_A}{RT}} \quad (2-11)$$

where E_A is the activation energy, R is the gas constant, and T is the absolute temperature. The forward (J_F) and backward reaction (J_B) rate can be written by

$$J_F = C_R \cdot f_F \cdot e^{-\frac{E_A}{RT}} \quad (2-12)$$

$$J_B = C_P \cdot f_B \cdot e^{-\frac{E_A - \Delta G_{Rxn}}{RT}} \quad (2-13)$$

where C_R and C_P are the concentration of reactants and products at the surface, respectively. f_F and f_B are the frequency of activated species moving forward and backward, respectively. ΔG_{Rxn} is the chemical free energy change. The net reaction rate (J) is

$$J = J_F - J_B = C_R \cdot f_F \cdot e^{-\frac{E_A}{RT}} - C_P \cdot f_B \cdot e^{-\frac{E_A - \Delta G_{Rxn}}{RT}} \quad (2-14)$$

Since the reaction at electrode involves charge transfer, the rate is connected to current density (j) by Faraday's law (Eq. 2-15)

$$j = n \cdot F \cdot J = n \cdot F \cdot C_R \cdot f_F \cdot e^{-\frac{E_A}{RT}} - n \cdot F \cdot C_P \cdot f_B \cdot e^{-\frac{E_A - \Delta G_{Rxn}}{RT}} \quad (2-15)$$

where j is the current density, n is the number of electron transferred during the reaction, and F is Faraday's constant. In an electrochemical system, the accumulation or depletion of charged species creates the electrical potential gradient ($\Delta\Phi$), and exerts additional force on charged species as seen in Figure 2-3b by

$$\Delta\tilde{G} = \Delta G + n \cdot F \cdot \Delta\Phi \quad (2-16)$$

where \tilde{G} is the electrochemical potential. Eq. 2-15 then becomes

$$j = n \cdot F \cdot J = n \cdot F \cdot C_R \cdot f_F \cdot e^{-\frac{E_A}{RT}} - n \cdot F \cdot C_P \cdot f_B \cdot e^{-\frac{E_A - \Delta G_{Rxn} + nF\Delta\Phi}{RT}} \quad (2-17)$$

When $-\Delta G_{Rxn} + nF\Delta\Phi = 0$, the system reaches the equilibrium as Figure 2-3c describes and no current flows as the rates of forward and backward reactions are the same. The current density at equilibrium state is called the exchange current density (j_0). That is,

$$j_0 = j_f = j_b = n \cdot F \cdot C_R \cdot f_F \cdot e^{-\frac{E_A}{RT}} \quad (2-18)$$

The rate of forward and backward reaction can be manipulated by adjusting the electrical potential as described in Figure 2-4. The applied potential for the reduction of the forward reaction is called activation overpotential (η_{act}). The current density as a result of applying activation overpotential can be written as

$$j = j_o \cdot \left(e^{\frac{\alpha \cdot n \cdot F \cdot \eta_{act}}{RT}} - e^{-\frac{(1-\alpha) \cdot n \cdot F \cdot \eta_{act}}{RT}} \right) \quad (2-19)$$

where α is the transfer coefficient, of which the value depends on the symmetry of the activation barrier. Eq. 2-19 is known as the Butler-Volmer equation, which defines the relation between the activation overpotential and current density. Figure 2-5 plots the activation overpotential as a function of current density according to Eq. 2-19. In the figure an increase in exchange current reduces the activation overpotential. Since the exchange current density is a function of the reactant and activation barriers in Eq. 2-18, improvement of the exchange current density can be achieved by using appropriate catalysts and increasing reactant concentrations.

2.2.3 Ohmic Overpotential

The origin of ohmic overpotential is the ohmic resistances of cell components against the transport of charged species. The overall ohmic overpotential can be expressed by

$$\eta_{ohmic} = (ASR_{electrodes} + ASR_{electrolyte} + ASR_{contact}) \cdot j \quad (2-20)$$

where j is the current density and ASR are the area specific resistances, which refers to the resistance normalized by area. Generally the electrode is a good electronic conductor, and so ohmic overpotential mostly arises from electrolyte. There is a relationship between ASR, sample dimension and resistivity (Eq. 2-21).

$$ASR = R \cdot A = \rho \cdot L = (1/\sigma) \cdot L \quad (2-21)$$

where R is the resistance, A is the area, ρ is the resistivity, L is the thickness and σ is the conductivity. Two approaches have been widely employed to reduce ohmic losses: (1) reducing electrolyte thickness via thin film technique and anode supported cell design (2) reducing resistivity by using faster oxygen ionic conductor. In an anode supported cell, the anode provides the mechanical support so the electrolyte thickness can be much thinner compared to an electrolyte supported cell as described in Figure 2-6. In addition, some materials such as doped CeO_2 and doped Bi_2O_3 have higher ionic conductivity compared to stabilized ZrO_2 .¹⁸ Application of those materials for the electrolyte has been demonstrated for high performance SOFC in the intermediate temperature range.

Recently contact resistance has received growing attention. In the level of small size cell test, the magnitude of contact resistance is insignificant. However, with larger area stacked cell, the use of metal interconnects can lead to the formation of less conductive secondary phases at the interface between electrode and interconnect.¹⁹ Moreover, unbalanced compressive pressure over a large area due to warpage may lead to poor contact and a substantial increase in contact resistance. Proper system design and development of contact materials to provide uniform and reliable electrical contact is important to keep contact resistance mitigated in the large scale cell.

2.2.4 Concentration Overpotential

The theoretical calculation of activation overpotential and equilibrium voltage assumes that the reactant concentration remains constant. However, as Figure 2-7a describes, the concentration in the region in the vicinity of electrode surface varies due to electrode reaction, which consumes reactants and produces products. The loss due to reduced concentration of reactants is the origin of concentration overpotential. Mass

transport through the diffusion layer is governed by a concentration gradient and diffusivity. At a steady state condition as described in Figure 2-7b, the diffusion flux (J_{diff}) can be described using Fick's 1st law (Eq. 2-22).

$$J_{Diff} = -D \frac{\Delta C}{\Delta x} = -D \frac{C_R^* - C_R}{\delta} \quad (2-22)$$

where D is the apparent diffusivity of reactants in the diffusion layer, C_R and C_R^* are the concentrations of reactants in the free stream and at the electrode surface respectively, and δ is the thickness of the diffusion layer.¹⁰

The diffusion flux reaches maximum value when C_R^* approaches zero. Since the diffusion flux is associated with current density by Faraday's law, the maximum or limiting current density (j_L) is

$$j_L = n \cdot F \cdot D \cdot \frac{C_R}{\delta} \quad (2-23)$$

j_L refers to the theoretical limit of current density that SOFC can produce.

Reduced concentration of reactants at the electrode surface leads to an increase in activation overpotential and equilibrium voltage. The magnitude of the increase in activation overpotential is

$$\eta_{con}(act) = \eta_{act}(C_R^*) - \eta_{act}(C_R) \quad (2-24)$$

Inputting the C_R^* into Eq. 2-19 gives

$$j = j_o \cdot \frac{C_R^*}{C_R} \cdot e^{\frac{\alpha \cdot n \cdot F \cdot \eta_{act}}{RT}} - j_o \cdot \frac{C_P^*}{C_P} \cdot e^{\frac{-(1-\alpha) \cdot n \cdot F \cdot \eta_{act}}{RT}} \quad (2-25)$$

At high current density, where depletion of reactants is significant when the forward

reaction on the electrode surface is substantially fast, $\frac{\alpha \cdot n \cdot F \cdot \eta_{act}}{RT} \gg 1$

So Eq. 2-33 can be simplified into

$$\eta_{\text{act}} \approx \frac{R \cdot T}{\alpha \cdot n \cdot F} \ln \left(\frac{j \cdot C_R}{j_o \cdot C_R^*} \right) \quad (2-26)$$

Inputting Eq. 2-26 into 2-24 yields

$$\eta_{\text{con}}(\text{act}) = \frac{R \cdot T}{\alpha \cdot n \cdot F} \ln \left(\frac{C_R}{C_R^*} \right) \quad (2-27)$$

This can be expressed in terms of j_L based on the relationship between C_R and j_L in Eq. 2-22 and 2-23.

$$\eta_{\text{con}}(\text{act}) = \frac{R \cdot T}{\alpha \cdot n \cdot F} \ln \left(\frac{j_L}{j_L - j} \right) \quad (2-28)$$

Meanwhile, equilibrium voltage also drops due to reduced concentration of reactant. In the same manner above, this provides

$$\eta_{\text{con}}(E_{\text{eq}}) = E_{\text{eq}}(C_R) - E_{\text{eq}}(C_R^*) = \frac{R \cdot T}{n \cdot F} \ln \left(\frac{j_L}{j_L - j} \right) \quad (2-29)$$

The summation of Eq. 2-28 and 2-29 provides the overall concentration overpotential, which can be written as

$$\eta_{\text{con}} = \frac{R \cdot T}{n \cdot F} \left(1 + \frac{1}{\alpha} \right) \ln \left(\frac{j_L}{j_L - j} \right) \quad (2-30)$$

If the concentration overpotential is plotted as a function of current density according to Eq. 2-30, it shows rapid increase as the current density approaches the limiting current density as seen in Figure 2-8. In order to reduce concentration overpotential, the limiting current density needs to be increased. Eq. 2-23 provides that the limiting current can be increased by efficient delivery of fuels and oxygen from appropriate design of the interconnect and porous electrode structure.

2.2.5 Other Losses

The equilibrium voltage given in the Nernst equation (Eq. 2-9) assumes a pure ionic conductor, in which electronic conduction is zero. If there is a partial electronic conduction across the electrolyte, the equilibrium voltage is lower than the ideal case. The ratio of ionic and electronic conduction can be expressed as a transference number (t). The electronic (t_e) and ionic (t_i) transference numbers are defined as

$$t_e = \frac{\sigma_e}{\sigma_e + \sigma_i} \quad (2-31)$$

$$t_i = \frac{\sigma_i}{\sigma_e + \sigma_i} \quad (2-32)$$

where σ_e and σ_i are the electronic and ionic conductivity, respectively. The summation of t_e and t_i must be the unity. Using the transference number, the loss in equilibrium voltage (E_L) can be written as

$$E_L = E_{Eq} \times t_e \quad (2-33)$$

Thus, loss in the equilibrium voltage is increased with electronic conduction. For example, doped CeO_2 is a fast oxygen ion conductor. However, Ce has a multi-valent state so that there is a partial electronic conduction at reduced condition. Therefore, it is difficult for a cell using a thin doped CeO_2 electrolyte to obtain an ideal equilibrium voltage. In order to overcome this problem, there have been attempts to make bi-layers, which consist of a fast ionic conductor and a pure ionic conductor (ZrO_2 or Bi_2O_3).^{20, 21}

2.3 Efficiency and Degradation

The efficiency ($\epsilon_{\text{thermodynamic}}$) of the SOFC can be defined as^{20, 21}

$$\epsilon_{\text{thermodynamic}} = \frac{\text{Useful energy}}{\text{Total energy}} = \frac{\Delta G}{\Delta H} = 1 - \frac{\Delta S}{\Delta H} \quad (2-34)$$

Using thermodynamic data in Table A-1, the efficiency of electrochemical conversion is approximately 0.8 at 800°C. However, the efficiency in practical SOFC operation is lower than that because of fuel utilization. When the cell voltage approaches E_{Eq} , fuel consumption is reduced and unused fuels in the exhaust reduce the fuel-cell efficiency. The fuel utilization efficiency (ϵ_{fuel}) can be written as

$$\epsilon_{fuel} = \frac{j/nF}{J_{fuel}} \quad (2-35)$$

where j is the current density, J_{fuel} is the rate at which fuel is supplied to the cell. The overpotential is another factor affecting the efficiency. In the previous section, the cell voltage was shown to decrease due to the overpotential. As a result the efficiency of the SOFC is further decreased. The voltage efficiency ($\epsilon_{voltage}$) is defined as

$$\epsilon_{voltage} = \frac{V}{E_{Eq}} \quad (2-36)$$

Generally the total cell efficiency is represented by the product of the thermodynamic, fuel utilization, and voltage efficiency (Eq. 2-37).

$$\epsilon = \epsilon_{thermodynamic} \cdot \epsilon_{voltage} \cdot \epsilon_{fuel} \quad (2-37)$$

This indicates that the conversion efficiency depends on the operating conditions such as current density or voltage. Figure 9 shows the efficiency of the cell as a function of cell voltage. As the output voltage is close to the equilibrium voltage. The ideal efficiency ($\epsilon_{thermodynamic} \cdot \epsilon_{voltage}$) increases with increasing output voltage but the fuel utilization efficiency drops as the voltage approaches to the equilibrium voltage. Therefore, SOFC operation conditions need to be carefully decided to get high efficiency.

The long term stability of the system is of the utmost importance for practical application. Solid State Energy Conversion Alliance, which is initiated by Department of Energy, has set 2.0% per 1000 hours as a degradation rate of SOFC system by 2010 and planned to further reduce the degradation rate. The power density of the cell is current density multiplied by voltage. Therefore, the degradation rate of the cell is proportional to increase in internal losses in constant current density mode. Since the activation overpotential is the dominant factor affecting the overall internal loss, reducing the degradation of cathodes is necessary to minimize the degradation of SOFC.

2.4 Overview of Cathode

2.4.1 Requirements

The requirements for a SOFC cathode are²²

- High catalytic activity for oxygen reduction.
- High electronic and ionic conductivity under oxidizing condition
- Chemical compatibility with neighboring cell components
- Matched thermal expansion coefficient
- Good stability at high temperature
- Good adhesion to electrolyte surfaces
- Simple fabrication
- Adequate porosity
- Low cost

2.4.2 Oxygen Reduction Process

In order for oxygen reduction to occur, reactants, electron (e^-), oxygen vacancies ($V_o^{\bullet\bullet}$) and oxygen gas molecule (O_2), must be supplied simultaneously according to Eq. 2-3. Thus, reduction of oxygen takes place at the three phase boundary (TPB) of air, cathode, and electrolyte phase as Figure 2-10a shows. The overall reaction of oxygen reduction may involve a number of elementary steps such as

- Gas phase diffusion
- Adsorption of molecular oxygen ($O_2(g) + S_{ad} \rightarrow O_2(ad)$)
- Dissociation into atomic oxygen ($O_2(ad) \rightarrow 2O(ad)$)
- Charge transfer ($O(ad) + 2e^- \rightarrow 2O^{//}(ad)$)
- Incorporation of oxygen ions ($O^{//} + V_O^{**} \rightarrow O_o^x$)

Determining the rate limiting step for the oxygen reduction reaction may provide guidelines for improving catalytic activity. A number of papers have been devoted to the mechanistic study of oxygen reduction.²³⁻²⁵ However, there still remains uncertainty and disagreement about the sequence of steps as well as the rate determining step. This is in part due to differences in cathode compositions and microstructure, complex reaction process, heterogeneity of surface, and experimental conditions between different research groups.^{25, 26}

2.4.3 Mixed Ionic Electronic Conductor

For a pure electronic conductor such as Pt or $La_{1-x}Sr_xMnO_3$ (LSM), the number of active reaction sites is proportional to three phase boundary (TPB) length. One method to reduce cathode overpotential is to extend the TPB length by mixing the electronically conductive cathode and ionically conductive electrolyte, which is called a composite cathode. Another method is to replace the electronic conductor with a mixed ionic and electronic conductor (MIEC) material which conducts oxygen ions as well as electrons. Due to the large amount of oxygen vacancies of the electrodes, oxygen gas can be reduced into ions over the electrode surface, giving rise to extensive active reaction sites (Figure 2-10b). A composite cathode between the MIEC and electrolyte was found to further improve oxygen reduction kinetics.²⁷

ABO_3 perovskite-structured oxides are typical MIECs, wherein A site and B site cations have 12 and 6 coordination to oxygen ions, respectively. The ideal structure of

cubic perovskite is illustrated in Figure 2-11. As long as a tolerance factor (Eq. 2-34) lies in the proper range ($0.7 < t < 1.0$), the perovskite structure can be maintained.

$$t = \frac{(r_A + r_O)}{\sqrt{2}(r_B + r_O)} \quad (2-34)$$

where t is the tolerance factor, r_A , r_B , and r_O are the ionic radii of A, B and oxygen respectively. When the tolerance factor is between approximately 0.89 and 1, the perovskite is likely to adopt cubic structure. Out of that range, the structure can be slightly distorted, having lower symmetry such as rhombohedral and orthorhombic.⁸

Many studies have attempted to elucidate the relationship between the catalytic property and constituents of materials.³⁰⁻³⁶ It was shown that oxygen vacancies and B site transition metals were the critical factors affecting catalytic activity of ABO_3 perovskite materials.^{28, 29} Figure 2-12 shows that the surface exchange coefficient (k), which refers to apparent rate of oxygen reduction reaction, increases with oxygen vacancy concentration.³⁰ In the figure, open and closed symbols refer to reduction and oxidation runs, respectively. The surface exchange coefficient (k) and exchange current density (j_o) are related with each other by³¹

$$j_o = n \cdot F \cdot k \cdot [O] \quad (2-35)$$

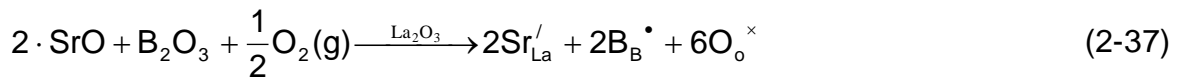
where $[O]$ is the oxygen concentration in the lattice. Thus, increased k indicates reduction in activation overpotential.

For SOFC cathodes, a mixture of rare and alkaline earths, and transitional metals have been widely tested for A and B sites ions, respectively. Recently, Co based perovskite materials such as $La_{1-x}Sr_xCoO_3$ and $Ba_{1-x}Sr_xCoO_3$ have been shown to display better performance than other cathode materials as shown in Figure 2-13. It was found that the electronic state and binding energy of transition metals were deeply

correlated to catalytic activities.^{24, 32, 33} There is no chemical reaction between Co based perovskite cathodes and Gd doped CeO₂ (GDC) electrolytes, but a higher thermal expansion coefficient (TEC) than GDC electrolyte is a critical problem.³⁴⁻³⁶ The TEC mismatch can lead to a substantial increase in interfacial resistance due to delamination. In order to match the TEC between the cathode and electrolyte while maintaining the catalytic activity, a mixture of Co and Fe in B site has been tested.

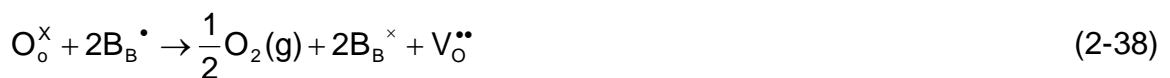
2.4.4 La_{1-x}Sr_xCo_yFe_{1-y}O_{3-δ} (LSCF)

La_{1-x}Sr_xCo_yFe_{1-y}O_{3-δ} (LSCF) is a typical MIEC. It provides high oxygen reduction capability and its TEC matches that of the GDC electrolyte. The structure of LSCF is not cubic but orthorhombic or rhombohedral perovskite depending on composition. La³⁺ is partially substituted by Sr²⁺ in order to create either oxygen vacancies or holes. The reaction can be described by



where B is the transition metal on the B site. Energetically the relative magnitude of the oxygen vacancy formation energy and valence stability of the transition metals determines the proportion of ionic and electronic compensation. At room temperatures, electronic compensation through Eq. 2-37 is pronounced.

The concentration of oxygen vacancies further increases at higher temperatures. This is due to the reduction of transition metals according to



The stability of the transition metals and bonding strength between metal-oxide ions determines the onset temperatures at which oxygen nonstoichiometry rapidly increases.³⁷ The effect from the amount of dopant on the A and B sites on the concentration of oxygen vacancies is shown in Figure 2-14. It shows that oxygen vacancy concentration in LSCF increases with amount of the Sr dopant. An increase with temperatures represents the reduction of transition metals.

While LSCF offers improved power densities than pure electronic conductors, it does not exhibit stable performance over long term period of time. Simner et al.³⁸ found the degradation of cell performance during 500 hours at 750°C as a result of substantial increase in electrode resistance. Similar degradation behavior of LSCF cathode was also reported by Kim et al.³⁹ In a practical application, SOFCs need to be operated in “stack”, in which metal interconnects connects several single cells in series to produce higher voltage. Since such metal interconnects contain high concentration of Cr, the interaction between LSCF cathode and Cr vapor from metal interconnects can lead to more significant degradation in cathode performance.⁴⁰

2.5 Summary

This chapter covers basic background and operation principle of SOFCs. The key performance of SOFC is explained by voltage and current density characteristic, followed by various overpotentials. During SOFC operation, the activation overpotential, which is primarily determined by the oxygen reduction reaction on cathodes, is the dominant loss. Therefore, improvement of catalytic activity and stability of cathode materials can contribute to enhancement in cell performance. As a mixed ionic electronic conductor (MIEC), LSCF cathodes have been widely used for a solid oxide fuel cell cathode due to the high ionic and electronic conducting properties^{22, 41} They

have also exhibited enhanced catalytic activity for oxygen reduction compared to the pure electronic conductor.⁴² However, an attempt to reduce operating temperatures causes the reduced rate of oxygen reduction reaction (ORR), which results in a substantial increase in activation overpotential. In addition, LSCF cathodes exhibited substantial degradation during the long term test.

Materials performance and properties are deeply related to materials structures. Especially, a heterogeneous reaction is primarily affected by surface structure and composition. Therefore, investigation of the chemical and structural variations of LSCF at high temperatures can contribute to better understand degradation mechanisms and improve cathode performance.

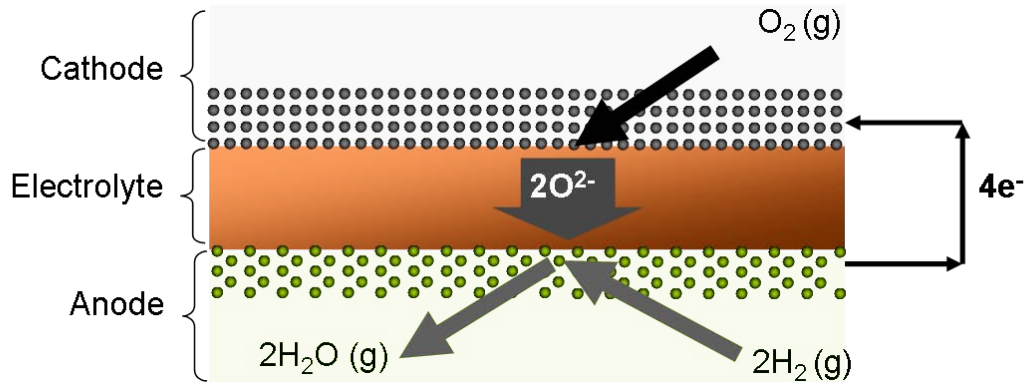


Figure 2-1. Schematic diagram of the cross section of a planar type SOFC.

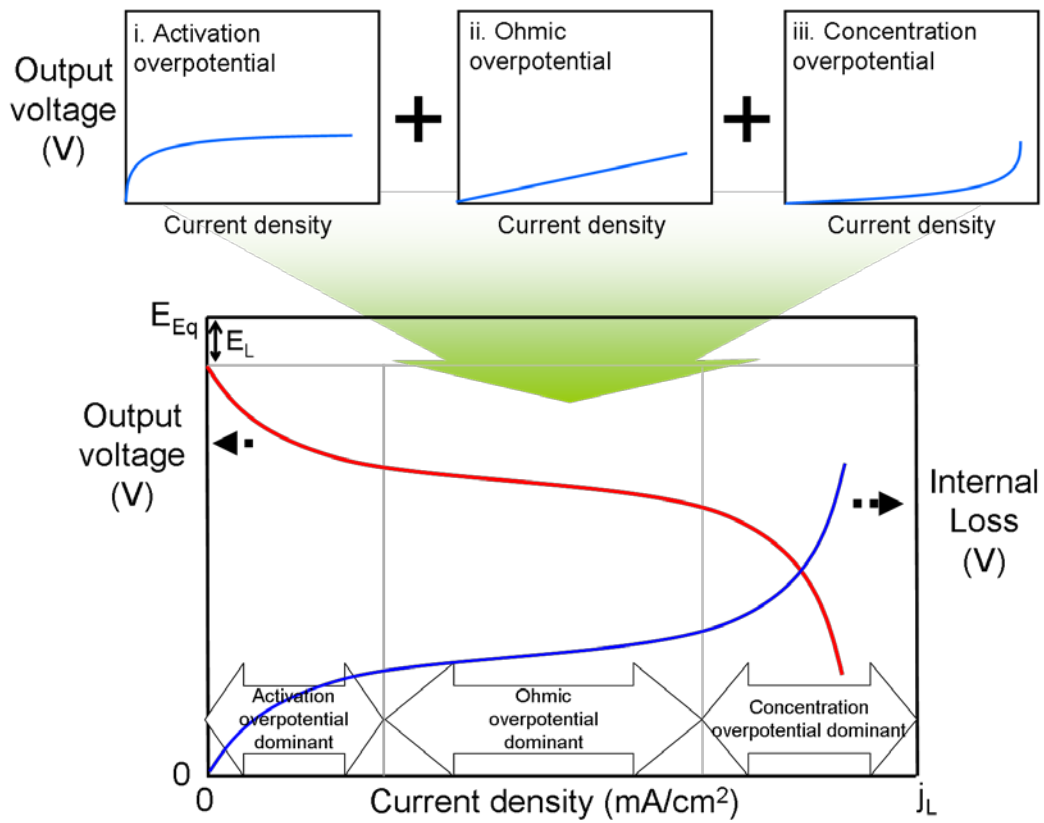


Figure 2-2. Typical current density and voltage characteristic of SOFC. j_L is the limiting current density.⁴³

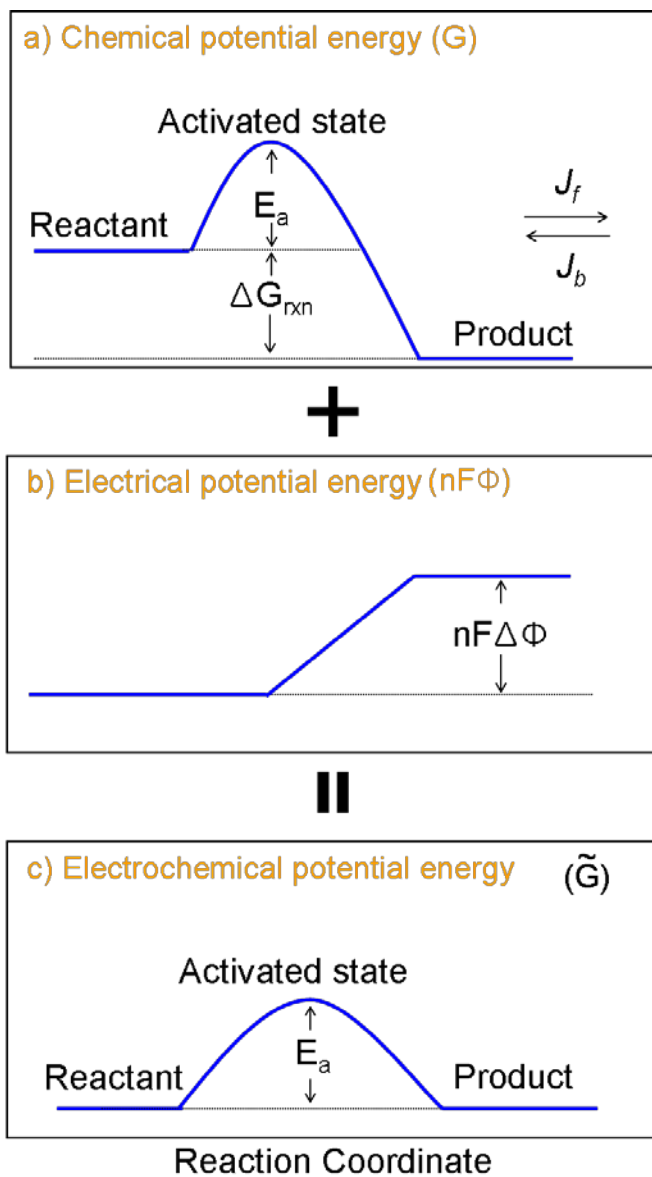


Figure 2-3. Contribution of chemical and electrical potential gradients to the equilibrium state at the electrochemical system.

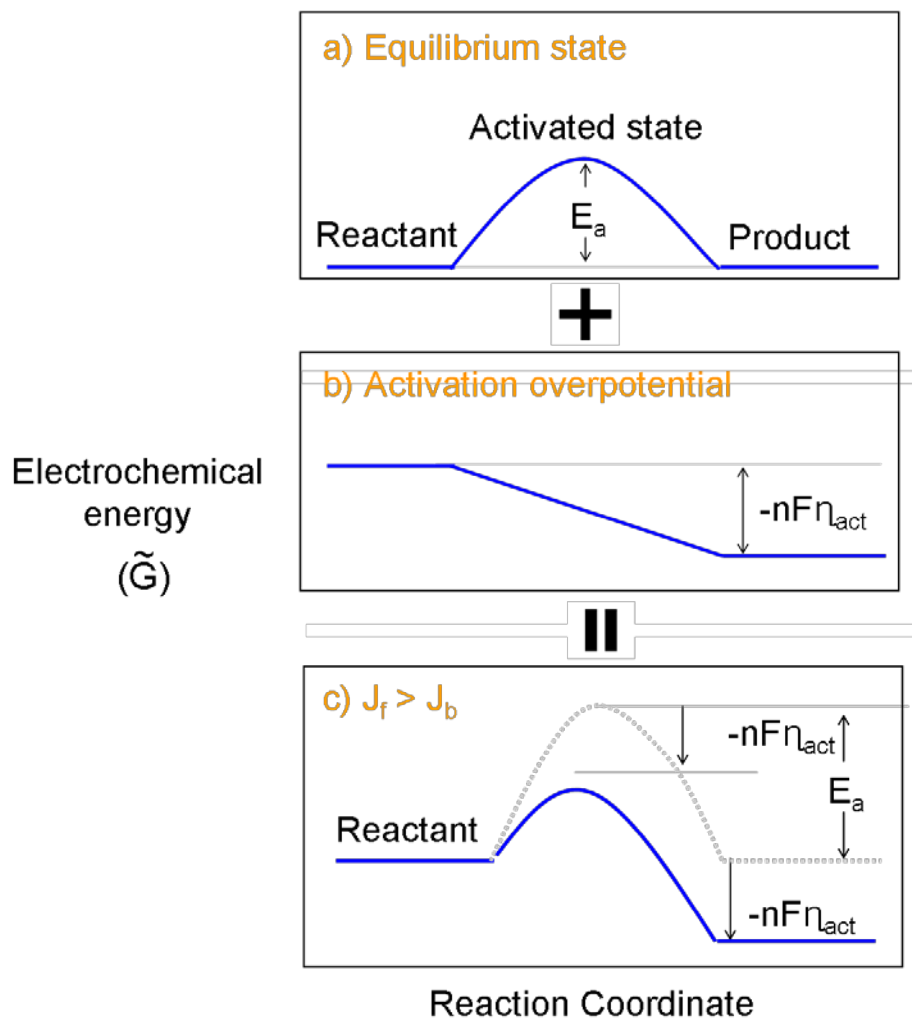


Figure 2-4. The electrochemical energy change from equilibrium state as a result of applying activation overpotential.

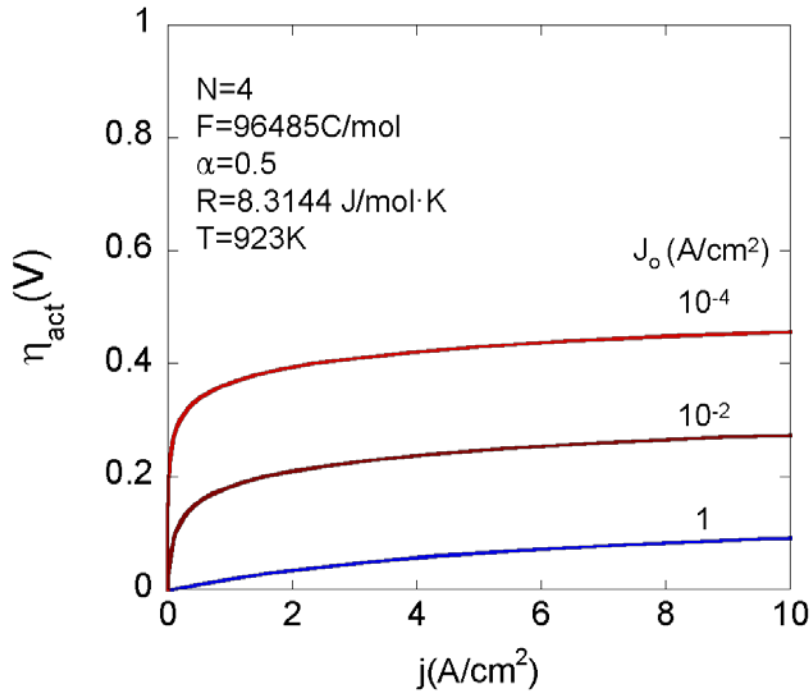


Figure 2-5. Activation overpotential (η_{act}) as a function of current density and the effect of exchange current density (j_0) on activation overpotential.



Figure 2-6. Schematic diagram of the cross section for (a) electrolyte and (b) anode supported cell.

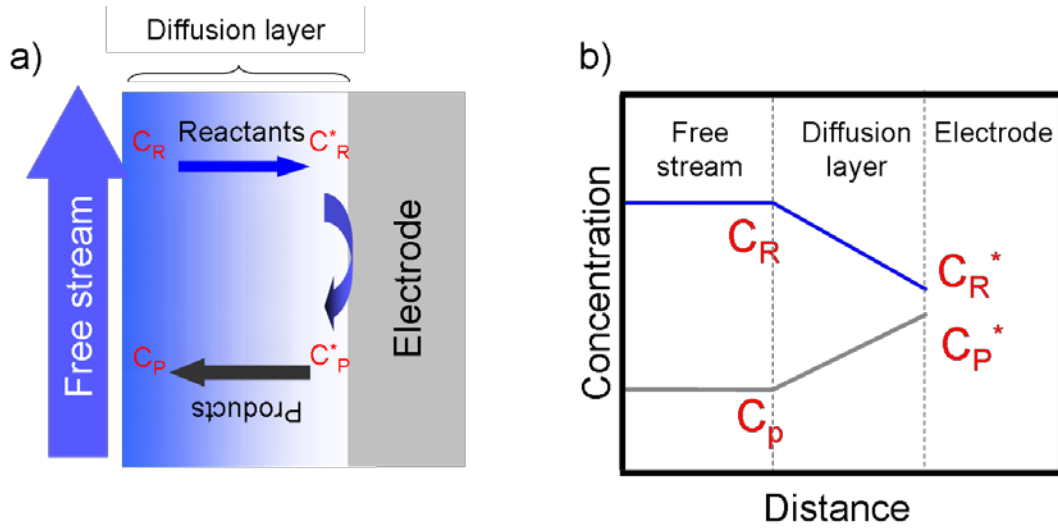


Figure 2-7. (a) Sketch of a diffusion layer between free stream and electrode and (b) concentration profiles across a diffusion layer at steady state.¹⁰

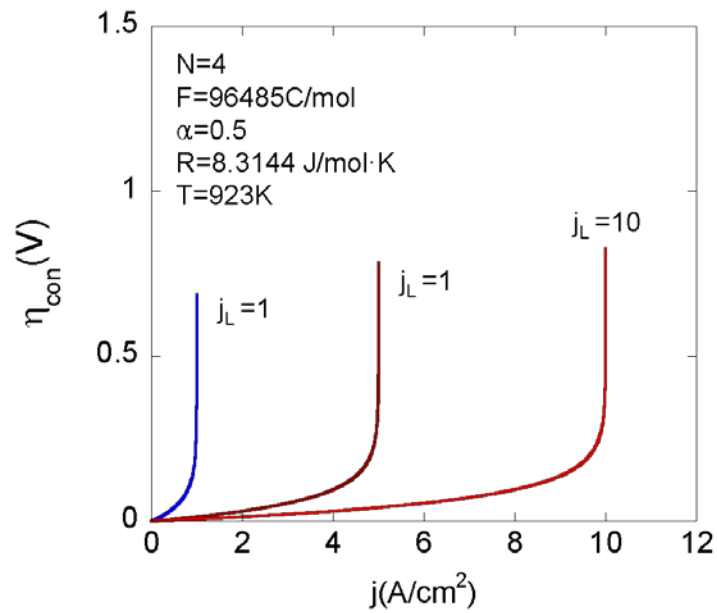


Figure 2-8. Plot of concentration overpotential (η_{con}) as a function of current density.

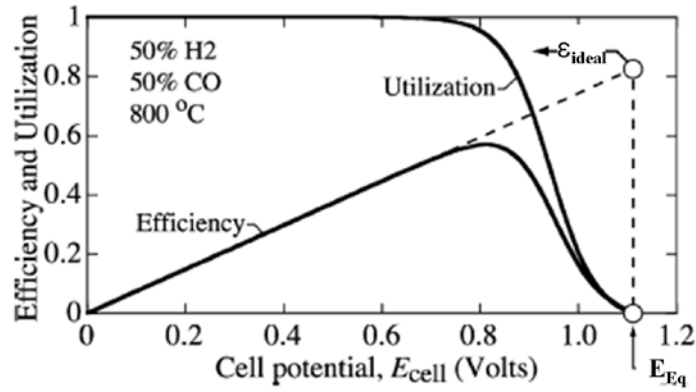


Figure 2-9. The efficiency (ϵ) and fuel utilization curve of an SOFC as a function of cell voltage (E_{cell}) at 800°C.²⁰

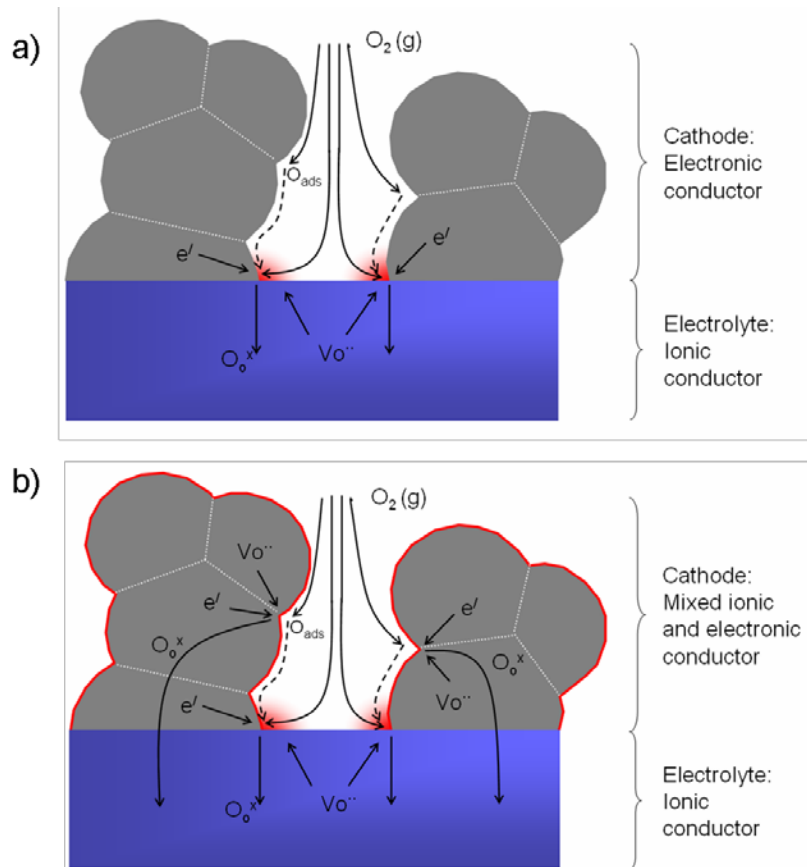


Figure 2-10. Active reaction sites (painted in red) for oxygen reduction. (a) Pure electronic conductors and (b) mixed ionic and electronic conductors.²³

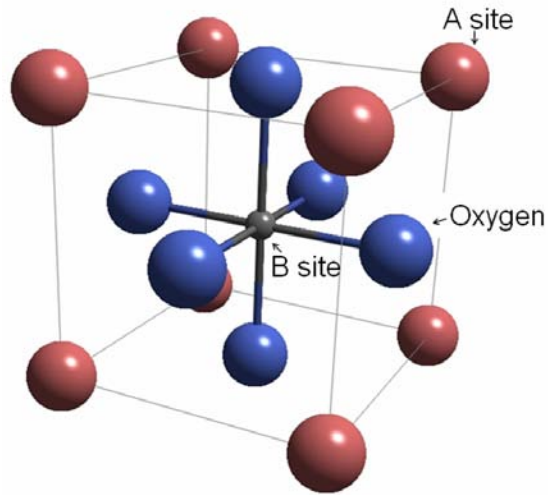


Figure 2-11. Unit cell of pseudo cubic perovskite of ABO_3 perovskite

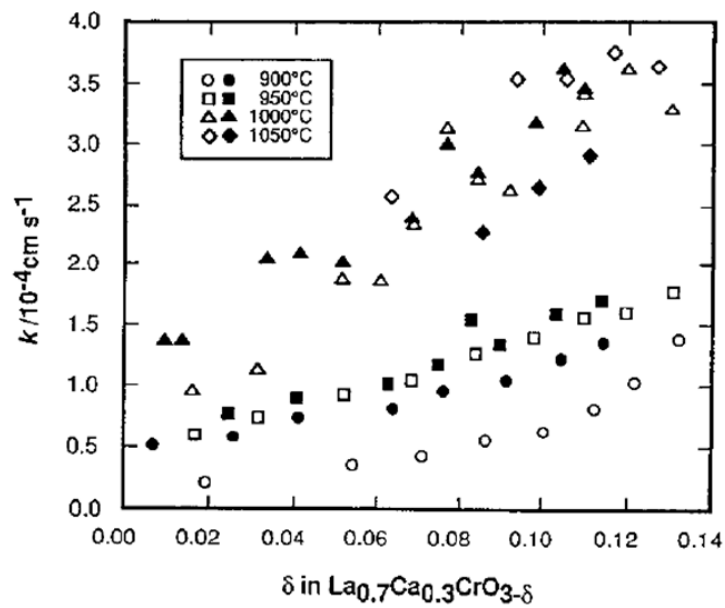


Figure 2-12. Surface exchange coefficients of $La_{0.7}Ca_{0.3}CrO_{3-\delta}$ as a function of mole fraction of oxygen vacancy.³⁰

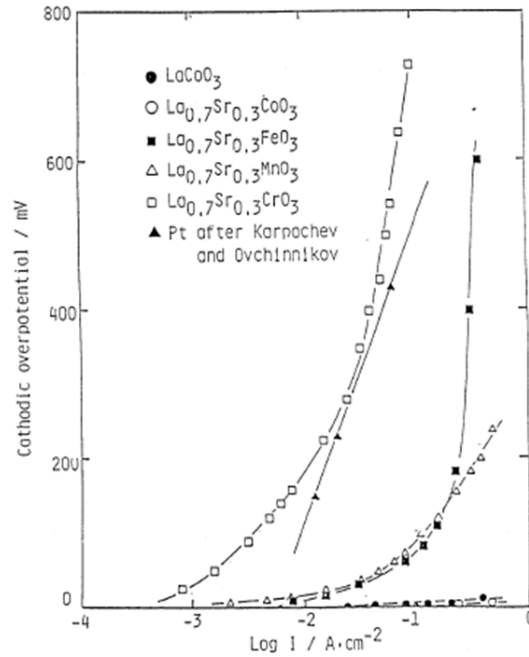


Figure 2-13. Effect of B site transition metals on $\text{La}_{0.7}\text{Sr}_{0.3}\text{BO}_3$ cathode over potential.⁴⁴

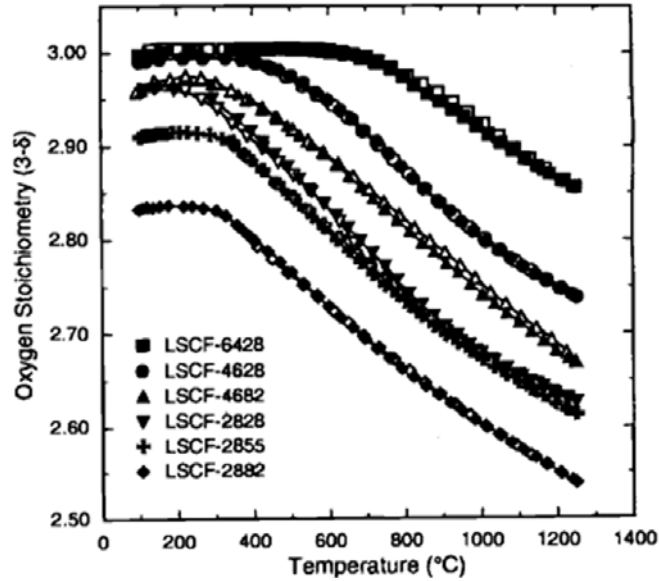


Figure 2-14. Oxygen nonstoichiometry (δ) of different LSCF composition as a function of temperature.⁴⁵

CHAPTER 3
EXPERIMENTAL

3.1 Electrical Conductivity Relaxation

3.1.1 Theoretical Background

Electrical conductivity relaxation measures the transient electrical conductivity change of the sample in response to a step change of oxygen partial pressure. The measured data is fit to obtain the chemical diffusion coefficient of oxygen in the lattice and the chemical exchange coefficient on the surface.⁴⁶⁻⁴⁹ The kinetic model applied for ECR is the solution to non-steady state diffusion, which is known as Fick's 2nd law. When the thickness (2x) of the sample is much smaller than both the width (2y) and the length (2z), the spatial and time dependence of the oxygen concentration can be described by

$$\frac{\partial C}{\partial t} = D_{\text{chem}} \frac{\partial^2 C}{\partial x^2}, \quad -l \leq x \leq l \quad (3-1)$$

where C is the oxygen concentration, t is the time, and D_{chem} is the chemical diffusion coefficient. The initial and boundary conditions are given in Eqs. 3-2 and 3-3, which mean that the sample is initially at an equilibrium, and the derivative of oxygen concentration with respect to position at the center of the sample ($x = 0$) is zero, respectively.

$$C(x) = C_0, \quad \text{when } t = 0 \quad (3-2)$$

C_0 is the initial equilibrium concentration.

$$\left. \frac{\partial C}{\partial x} \right|_{x=0} = 0 \quad (3-3)$$

The oxygen exchange process at the surface is assumed to proceed at a rate proportional to the difference between the concentration at the new equilibrium and the

transient surface concentration. This provides boundary condition at the surface (Eq. 3-4).

$$-D_{\text{chem}} \left. \frac{\partial C}{\partial x} \right|_{x=\pm l} = K_{\text{chem}} (C_{\infty} - C_t) \quad (3-4)$$

K_{chem} is the chemical exchange coefficient that refers to the apparent surface reaction coefficient. On the basis of initial and boundary conditions, the mathematical solution to Eq. 3-1 is given by⁵⁰

$$\frac{C_t - C_0}{C_{\infty} - C_0} = 1 - \sum_{m=1}^{\infty} \frac{2 \cdot L \cdot \cos\left(\frac{\alpha_m \cdot x}{l}\right) \cdot \exp\left(-\frac{\alpha_m^2 \cdot D_{\text{chem}} \cdot t}{l^2}\right)}{(\alpha_m^2 + L^2 + L) \cdot \cos \alpha_m} \quad (3-5)$$

l is half the thickness of the sample. Subscripts 0, t , and ∞ represent initial, transient and final equilibrium times, respectively. α_m is the positive root of the transcendental

equation $\alpha_m \tan \alpha_m = \frac{l \cdot K_{\text{chem}}}{D_{\text{chem}}} = L$. The integration of Eq. 3-5 in the range of $-l \leq x \leq l$

provides the total amount of diffusing oxygen species over the entire sample.

$$g(t) = \frac{M_t}{M_{\infty}} = 1 - \sum_{m=1}^{\infty} \frac{2 \cdot L^2 \cdot \exp\left(-\frac{\alpha_m^2 D_{\text{chem}} \cdot t}{l^2}\right)}{(\alpha_m^2 + L^2 + L) \cdot \alpha_m^2} \quad (3-6)$$

M_t and M_{∞} are the total amount of diffused components up to time t , and at the new equilibrium, respectively.

For $(A^{3+}_{1-x}A^{2+}_x)BO_3$ ($B=Co, Fe, Ni$), the relative mass change can be correlated to the electrical conductivity change via defect chemistry. The overall electro-neutrality condition is

$$n + [D'] + [V_{A^{3+}}^{///}] + [V_B^{///}] = p + [V_O^{**}] \quad (3-7)$$

where n and p are the electron and hole concentrations, respectively. $[D']$, $[V_{A3+}''']$, $[V_B''']$, and $[V_o''']$ are the concentrations of A site dopant, A site vacancy, B site vacancy and oxygen vacancy, respectively. In the high pO_2 region, where $[D'] \gg n + [V_{A3+}'''] + [V_B''']$, Eq. 3-7 can be written in a simpler form.⁵¹

$$[D'] = p + [V_o'''] \quad (3-8)$$

Since $[D']$ is constant, the following equation is satisfied.

$$\frac{[V_o''']_t - [V_o''']_o}{[V_o''']_\infty - [V_o''']_o} = \frac{p_t - p_o}{p_\infty - p_o} \quad (3-9)$$

The electrical conductivity of a p-type conductor is defined as

$$\sigma = p \cdot F \cdot \mu \quad (3-10)$$

where σ is the electrical conductivity, F is Faraday's constant, and μ is the mobility.

Assuming that the mobility is constant in small ΔpO_2 ranges, Eq. 3-9 can be written as

$$\frac{[V_o''']_t - [V_o''']_o}{[V_o''']_\infty - [V_o''']_o} = \frac{p_t - p_o}{p_\infty - p_o} = \frac{\sigma_t - \sigma_o}{\sigma_\infty - \sigma_o} \quad (3-11)$$

From the site relationship of oxygen vacancies and oxygen in the lattice (Eq. 3-12),

$$[V_o'''] + [O_o^x] = 3 \quad (3-12)$$

M_t / M_∞ can be re-written in terms of an electrical conductivity change as given by

$$\frac{M_t}{M_\infty} = \frac{[O_o^x]_t - [O_o^x]_o}{[O_o^x]_\infty - [O_o^x]_o} = \frac{[V_o''']_t - [V_o''']_o}{[V_o''']_\infty - [V_o''']_o} = \frac{p_t - p_o}{p_\infty - p_o} = \frac{\sigma_t - \sigma_o}{\sigma_\infty - \sigma_o} \quad (3-13)$$

Technically measurement of electrical conductivity changes is easier and more accurate compared to measurement of small mass changes at high temperatures. Therefore, the

electrical conductivity changes are measured and fit by Eq. 3-6 in order to obtain D_{chem} and K_{chem} .

3.1.2 Electrical Conductivity Measurement

The Lock in amplifier serves as a voltage source. By connecting a large external resistor in series as shown in Figure 3-1, a constant current is applied to the sample according to

$$i = \frac{V_{\text{Lock in amplifier}}}{R_{\text{sample}} + R_{\text{external}}} \approx \frac{V_{\text{Lock in amplifier}}}{R_{\text{external}}}, \text{ when } R_{\text{external}} \gg R_{\text{sample}} \quad (3-14)$$

where V is the output voltage from the Lock in amplifier, and R_{sample} and R_{external} are the resistances of the sample and external resistor, respectively. From Ohm's law the electrical conductivity of the sample was obtained according to

$$\sigma_{\text{sample}} = \frac{V_{\text{measured}}}{i} \cdot \frac{c}{a \cdot b} \quad (3-15)$$

where V_{measured} is the measured voltage at a given current (i). From Figure 3-1, a , b , and c define sample geometries of thickness, width, and measurement distance respectively.

3.1.3 Effect of Surface Roughness

Apparent rate coefficients for oxygen diffusion in the lattice and oxygen exchange reaction at the surface have been reported.^{46-49, 52} Generally there are agreements in reported values of the oxygen diffusion coefficients, but the oxygen surface exchange coefficients have presented a rather wide range of differences. This is in part due to different sample preparation. Figure 3-2 schematically describes the effect of surface roughness on the boundary conditions at the surface. In the figure, J_1 and J_2 are the total amount of diffused and exchanged oxygen and at the surface, respectively. A_1 and A_2 are the areas of the sub-surface and the top surface. J_1 and J_2 should be same if the

desorption is neglect. For a flat surface, the area of A_1 and A_2 are equivalent, and therefore this requirement is same as the boundary condition used in the derivation of kinetic model for electrical conductivity relaxation (Eq. 3-4). By contrast, A_2 is much larger than A_1 when the surface is rough. In this case, Eq. 3-4 is no longer adequate but the boundary condition needs to include the contribution of the higher surface area. As a result, when the sample having a rough surface is tested, it is likely to be an overestimated value in the form of $K \cdot A_2/A_1$.

Figure 3-3 compares D_{chem} and K_{chem} of polished and unpolished LSCF samples at 800°C. The sample dimension was approximately 2x2x20 mm³, therefore the two dimensional diffusion model was applied to fit the data. The pO₂ steps were 10→21→44% with a total flow rate of 500 ccm. While D_{chem} is roughly constant between the two samples, K_{chem} from the unpolished sample is approximately five times higher than that of the polished sample. The surface area of the unpolished sample, which was measured using atomic force microscope, was five times larger than that of the polished sample. It shows that an overestimated value due to surface roughness is close to a factor of A_2/A_1 . Therefore, for accurate measurement of the apparent oxygen exchange coefficient, the sample must have a flat surface, or the surface roughness and area need to be measured.

3.2 Electrochemical Impedance

Electrochemical impedance spectroscopy is a widely used technique for deconvoluting different reaction processes.⁵³ It measures a time dependent current in response to a small sinusoidal voltage perturbation. In a complex plane, impedance (Z) is given by

$$Z = Z_o e^{i\phi} = Z_o (\cos\phi + i\sin\phi) = Z_{\text{real}} + Z_{\text{img}} \quad (3-16)$$

where Z_o is the ratio of V_o and i_o , the amplitude of voltage and current, respectively. ϕ is the phase shift, $Z_o \cos\phi$ is a real component, and $i \cdot Z_o \sin\phi$ is an imaginary component.

A plot of Z_{real} on the x-axis and Z_{img} on the y-axis is called a Nyquist plot. Figure 3-4 shows an example of a Nyquist plot for an electric circuit, in which a resistor and a capacitor are connected in parallel. The capacitor and resistor are pure imaginary and real components, respectively. The capacitor works as a short circuit at high frequencies and current flows via the resistor at low frequencies. In the intermediate frequency range, impedance is the sum of imaginary and real components. It is important to understand the behavior of an RC circuit because many electrochemical reactions exhibit similar behavior.

3.3 Temperature Programmed Isotopic Exchange

In a dynamic equilibrium, the net flux of oxygen exchange between metal oxide and surrounding gas is zero, but there is continuous exchange. Temperature programmed isotopic exchange technique (TPX) is designed to distinguish lattice oxygen, which comes out of a sample, from gaseous oxygen, which incorporates into a sample, in a dynamic equilibrium condition. This is done by using oxygen isotope ($^{18}\text{O}_2$) in conjunction with a mass spectrometry (MS). One can assume that a pre-heat treated sample in normal oxygen ($^{16}\text{O}_2$) possesses only ^{16}O in the lattice and surface. If the feed stream is switched from $^{16}\text{O}_2$ to $^{18}\text{O}_2$ at room temperature, $^{18}\text{O}_2$ incorporates into the sample while $^{16}\text{O}_2$ comes out of the lattice. However, due to slow exchange kinetics, essentially no change in MS signals is observed at room temperatures, and thereby the input concentration of $^{18}\text{O}_2$ is the same as the output concentration of $^{18}\text{O}_2$. Since the

oxygen exchange kinetics are a function of temperature, oxygen exchange reaction increases with increasing temperatures. The onset temperature is called the temperature where the concentration of $^{18}\text{O}_2$ substantially drops. At this temperature, the MS signal of $^{16}\text{O}_2$ and $^{16}\text{O}^{18}\text{O}$ (scrambled species) starts to increase. In TPX analysis, comparison of the catalytic activity for oxygen reduction is made by comparing the onset temperature. A lower onset temperature implies a higher catalytic activity. Details of theoretical background can be found elsewhere.⁵⁴ Note that TPX tests a powder sample. Therefore, it can avoid the impact of electrical connections and sintering, which may affect surface catalytic activity.⁵⁵ In addition, TPX is a surface sensitive technique due to high surface area of powder sample.

3.4 Materials Characterizations

The instruments which were used in this study for material characterizations and their purpose of usage are listed in Table 3-1. Two chemical analyses were applied in this study: Energy dispersive spectroscopy and Auger electron spectroscopy. While the former provides the chemical composition of a bulk, the latter gives a surface composition. As the Core-level electron is removed by X-ray photo ionization or electron-impact ionization (Figure 3-5a), the atom is left in an excited state, and subsequently de-excitation occurs (Figure 3-5b). The energies of electrons in the shells are quantized and therefore, the energy difference between electron shells is a specific value for each element. In the Auger process, an outer level electron fills the core level and the excess energy ejects another electron in an outer level with a specific kinetic energy (Figure 3-5c). This electron is called Auger electron.⁵⁶⁻⁵⁸ In the characteristic X-ray process, the difference in the energy level is emitted as a photon of electromagnetic radiation (Figure 3-5d). The Auger electron and characteristic X-ray present

substantially different escape depth as illustrated in Figure 3-6. As an Auger electron has low kinetic energy, an escape depth of Auger electron is less than a few nanometers. Therefore, Auger electron spectroscopy, which is based on Auger process, is a surface sensitive technique. And Energy dispersive spectroscopy, which is based on characteristic X-ray process, provides bulk composition.

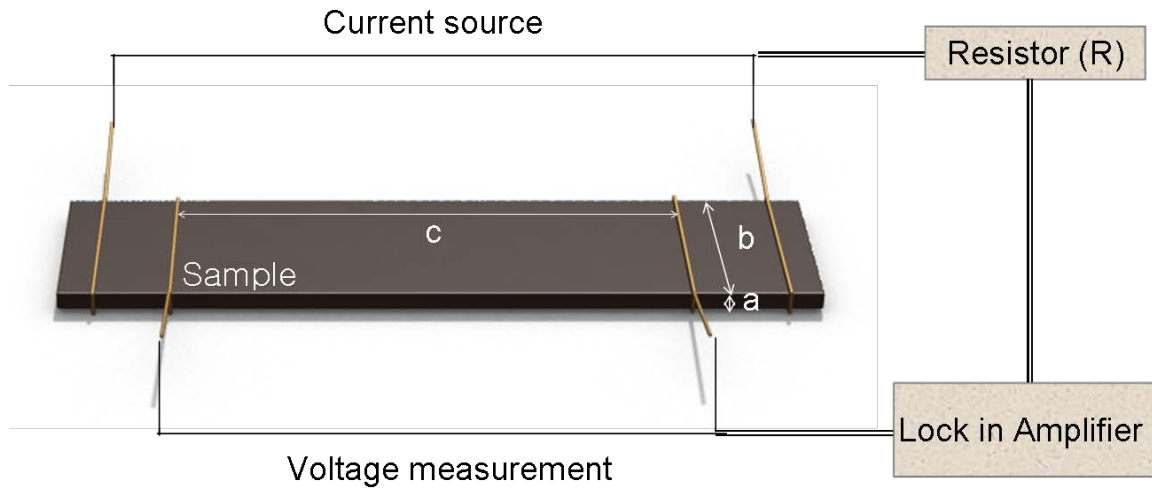


Figure 3-1. Sample dimension and electrical connection between the sample and Lock in Amplifier.

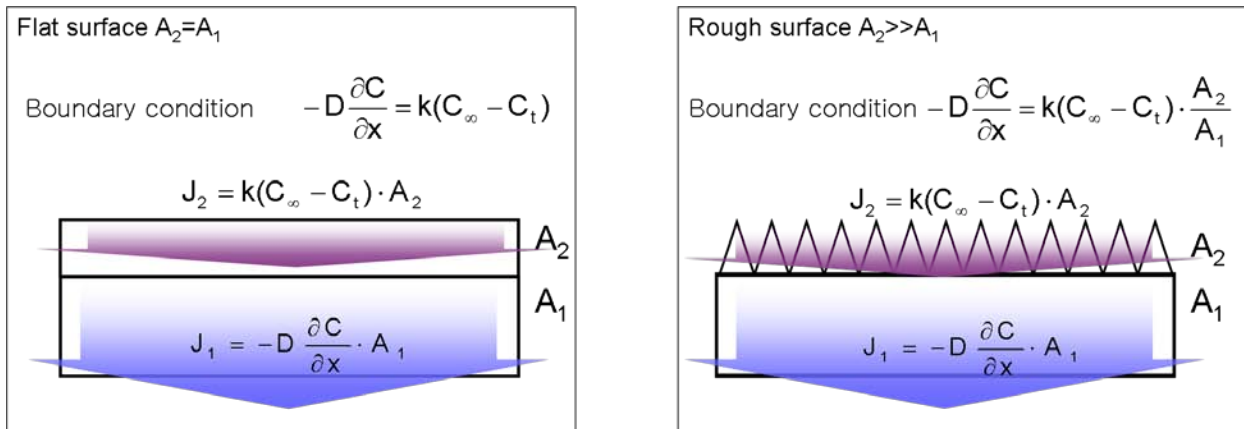
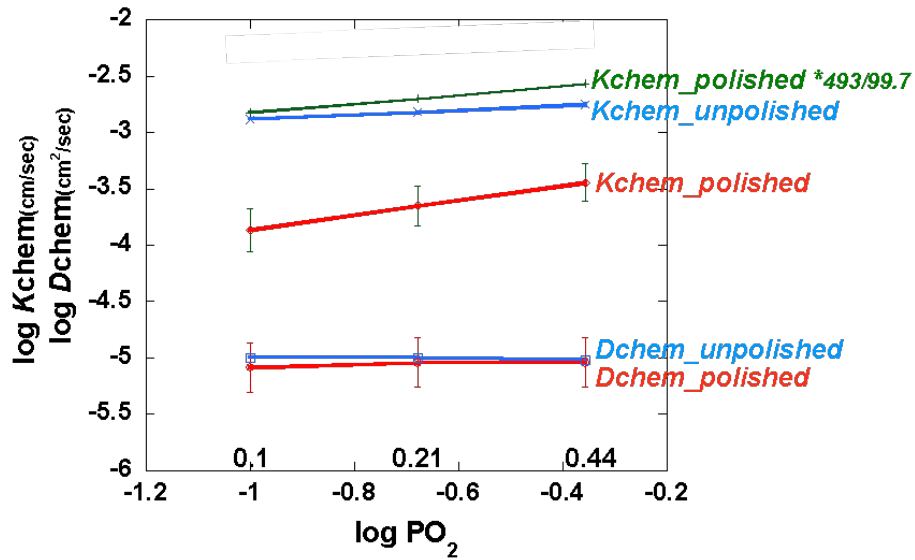


Figure 3-2 Schematic of the effect of a rough surface on the boundary conditions.



	RMS roughness (nm)	Image surface area (μm^2)
Unpolished sample	420	493
Polished sample	2.3	99.7

Figure 3-3. The effect of roughness on the measurement of D_{chem} and K_{chem} (top), and surface roughness and actual surface area of samples (bottom).

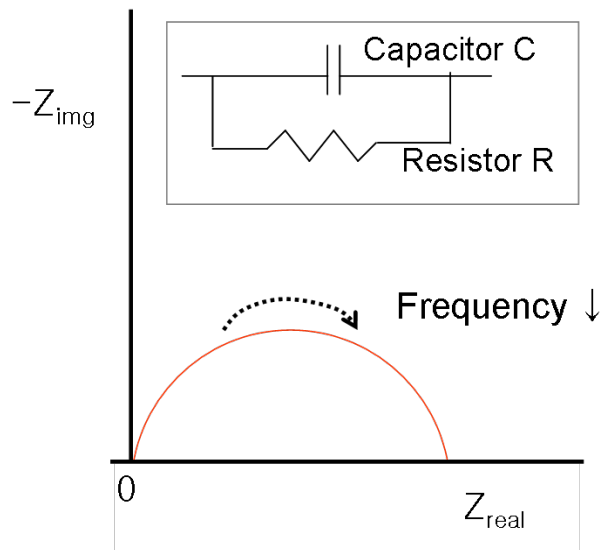


Figure 3-4. Nyquist plot of an RC circuit.

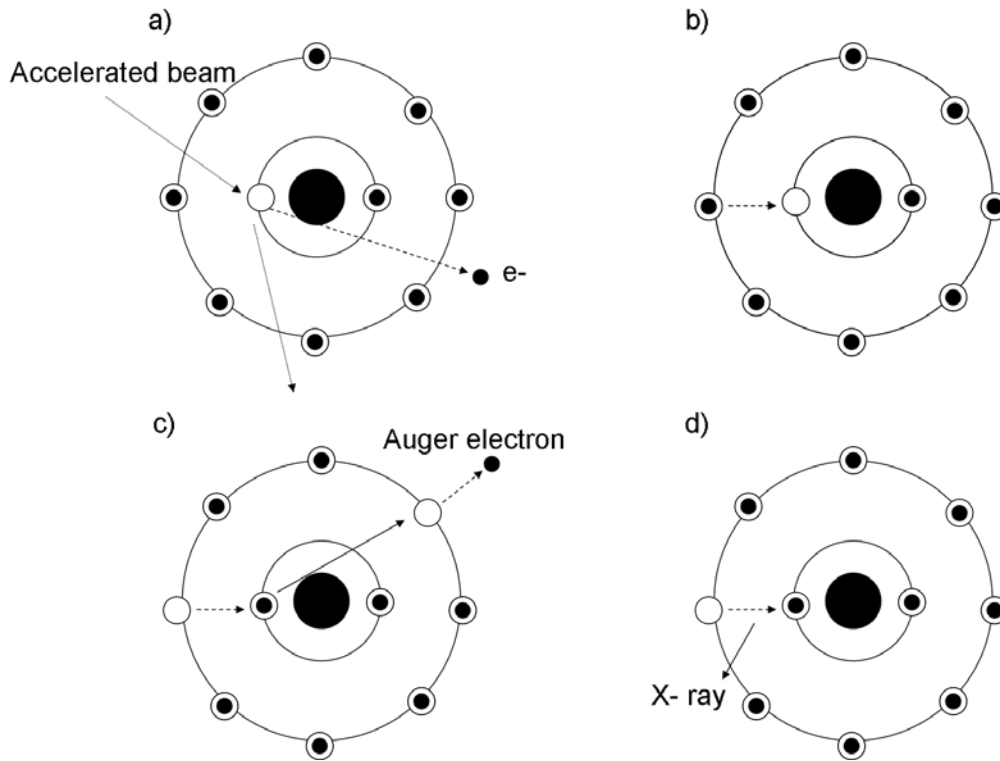


Figure 3-5. Core shell ionization and subsequent de-excitation via (c) Auger process and (d) characteristic X-ray emission.⁵⁸

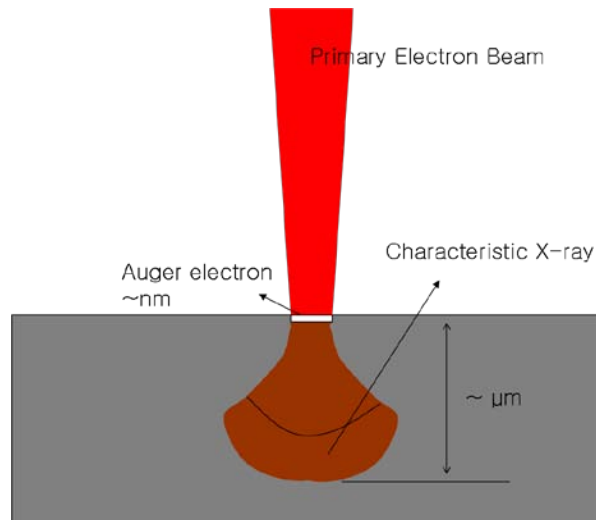


Figure 3-6. Schematic diagram of escape depth of Auger electron and characteristic X-ray.⁵⁸

Table 3-1. List of instruments for material characterizations.

Instrument	Purpose	Model and company
AES	Chemical analysis of top surface	Perkin-Elmer PHI 660 Scanning Auger Multiprobe
AFM	Surface roughness	Digital Instruments Dimension 3100
BET	Surface area of powder	Quantachrome NOVA 1200
FIB	Preparation of TEM specimen	Dual Beam - Focused Ion Beam (FIB) Strata DB 235
SEM	Surface morphology	JEOL JSM 6400 / 6335F
TEM	Analysis of the cross section for nano precipitate	JEOL TEM 2010F
EDS	Chemical analysis	
XRD	Crystal structure of secondary phases and synthesized powders	XRD Philips APD 3720 Philips MRD X'Pert System

CHAPTER 4 MECHANISTIC UNDERSTANDING OF LSCF DEGRADATION

4.1 Introduction

$\text{La}_{0.6}\text{Sr}_{0.4}\text{Co}_{0.2}\text{Fe}_{0.8}\text{O}_3$ (LSCF) has been widely used as a solid oxide fuel cell cathode. Due to partial substitution of Sr for La and reduction of transition metals, it has a substantial oxygen vacancy concentration at high temperatures, and therefore exhibits high ionic and electronic conductivity. However, several studies report that Sr in LSCF tends to segregate to electrode surfaces or interfaces.^{38, 59-61} As a result, the transition metal concentration was found to substantially decrease in the outermost surface layers. It is generally believed that B site transition metals play a critical role for catalytic activity of ABO_3 perovskite materials,^{26, 66-68} and heterogeneous interaction is primarily determined by surface composition and structure.⁶² Consequently, the formation of Sr enriched layer on LSCF surfaces can be a potential degradation mechanism of LSCF cathode-based cells.

Long-term stability is an important requirement for the commercialization of SOFCs. Thus, the development of LSCF for a practical SOFC cathode requires an understanding of Sr enrichment behavior on the surface. In the work presented herein, surface chemical compositional changes of LSCF at high temperatures were investigated by Auger electron spectroscopy (AES) and transmission electron microscopy (TEM). Dense and polished LSCF samples were examined to clearly identify surface morphological changes.

4.2 Experimental

4.2.1 Sample preparation

Figure 4-1 describes the sample preparation procedure. A dense LSCF sample

was prepared for analysis. It was prepared by pressing $\text{La}_{0.6}\text{Sr}_{0.4}\text{Co}_{0.2}\text{Fe}_{0.8}\text{O}_{3-\delta}$ powder (Praxair Specialty Ceramics, USA) uni-axially and sintering a pellet at 1400°C for 4 hours in air. The density of the sintered body measured by the Archimedes method was $\sim 97\%$ of the theoretical value (6.36 g/cm^3). The sintered body was cut and then polished with a series of SiC papers and diamond abrasives (Leco) down to $1 \mu\text{m}$. Several samples were mounted on a holder, which has a flat surface, using crystal bond. Crystal bond is an adhesive that melts at around 100°C , so it needed to be heated on a hot plate prior to application. After polishing, samples were detached either by re-heating above 100°C or submerging in acetone. By doing so, sample handling was much easier and multiple samples were polished simultaneously. All samples were cleaned with DI water and acetone before heat treatments. Final sample thicknesses were around 1 mm.

4.2.2 Heat treatment

Samples were located on a quartz plate in the middle of a quartz reactor as seen in Figure 4-2. They were exposed to stagnant air between $600\text{-}900^{\circ}\text{C}$ in the absence of Fe-Cr alloy. As K-type thermocouples (TC) could be a source of Cr contamination, the thermocouple was placed outside of the quartz reactor. Heat treatment was conducted for 50 hours and 100 hours in air, and heating and cooling rates were established at $5^{\circ}\text{C}/\text{min}$. LSCF was also heat treated in N_2 and $0.1\% \text{ O}_2$ for 50 hrs at 800 and 890°C . Gas flow rate was controlled by mass flow controller (MKS) and the total flow rate was fixed at 10 SCCM.

4.2.3 Characterization

X-ray diffraction patterns of the samples before and after heat treatment were measured (Philips APD 3720) with Cu-K α radiation ($\lambda=1.54\text{\AA}$). Low angle mode XRD

(Philips MRD X'Pert System) was applied in order to analyze the structural variation of the surface region. All data were compared to the literature and the Joint Committee on Powder Diffraction Standards database (JCPDS).

The morphological and compositional change was characterized using scanning electron microscopy (SEM, JSM 6335F) combined with energy dispersive spectroscopy (EDS, Oxford, UK). ZAF correction was used for semi-quantitative analysis, where Z is the atomic number, A is the absorption correction factor, and F is the fluorescence correction factors. The standard materials used in the analysis are quartz(SiO_2), Wollastonite(CaSiO_3), Cr, Fe, Co, SrF_2 , BaF_2 , and LaB_6 were used for O K, Ca K, Cr K, Fe K, Co K, Sr L, Ba L, and La L, respectively. The cross sectional specimen of the precipitate, which was formed on the surface region after heat treatment, was prepared by focused ion beam (FIB, FEI Strata DB235) and analyzed using transmission electron microscopy (TEM, JEOL 2010F) and EDS.

Surface chemical composition of LSCF before and after heat treatment was measured by Auger electron spectroscopy (AES, AES Perkin-Elmer PHI 660). The accelerating voltage was 10 kV and the scanned energy ranges were between 50 to 2050 eV, which covered the characteristic peaks of La_{MNN} (625 eV), Sr_{LMM} (1649 eV), Co (775 eV), and Fe_{LMM} (703 eV). These characteristic peaks were selected in order to minimize interference with each other. Obtained AES spectrum was differentiated, and elemental atomic percents were calculated based on the differentiated data using AugerScan 3.2.0 software (RBD Instrument). The atomic percents are calculated according to

$$\text{Atomic \%} = \frac{I_a/S_a}{\sum I_m/S_m} \quad (4-1)$$

where I is the peak intensity and S is the relative elemental sensitivity factor for the Auger line used. Relative sensitivity factors, which are provided by RBD instruments, are 0.06, 0.045, 0.19, 0.13, and 0.35 for La_{MNN} , Sr_{LMM} , Fe_{LMM} , Co_{LMM} and O_{KLL} , respectively. This study calculated the relative change based on the ratio of atomic percents before and after heat treatment which were normalized by oxygen concentration. The enrichment factor was calculated according to

$$\text{Enrichment Factor (E.F.)} = \frac{[X_{\text{cation}} / X_{\text{oxygen}}]_{\text{post HT}}}{[X_{\text{cation}} / X_{\text{oxygen}}]_{\text{pre HT}}} \quad (4-2)$$

4.3 Results and Discussion

In Figure 4-3 are representative SEM micrographs of the LSCF surfaces before and after heat treatment in air. Before heat treatment, LSCF exhibited dense and flat surfaces as shown in Figure 4-3a. However, after heat treatment, submicron precipitates were formed on the surfaces. These precipitates were more pronounced and exhibited higher areal density with increasing heat treatment temperatures from 600-900°C. Interestingly, in the figure, the precipitates were not formed along the grain boundaries but on grain surfaces at 800 and 900°C. The magnified images in Figure 4-4 show more clearly the shapes of the precipitates, which are different from grain to grain. The typical shapes of precipitates are rods, triangles, or irregular polygons. For the rod type, the direction of the precipitate was either well-aligned in one direction or vertically crossed. The precipitates were found not only on polished surfaces but also on unpolished surfaces as shown in Figure 4-4d. It shows that the direction of precipitates was well aligned along the facets of the grains. This observation indicates that the formation of precipitates corresponds to the surface orientation of the underlying grains. The characteristic of rod type precipitates is close to the Widmanstatten morphology, of

which an incoherent curved interface exhibits a fast growth rate while a semi-coherent facet has slower growth.⁶³ However, the formation of precipitates observed in this study is different from the Widmanstätten morphology in that the precipitates grow out of the surface.

Chemical analysis was conducted using EDS after heat treatment and the results were compared to the as-fresh sample. As Table 4-1 shows, EDS data indicates roughly constant atomic percents of all elements before and after heat treatment. This indicates that the bulk composition remains unchanged and the formation of precipitates is limited to the top surface or near the surface region. AES analysis was performed to investigate the compositional change of the surface region. Figure 4-5 shows differentiated AES spectra of La_{MNN}, Sr_{LMM}, Co_{LMM}, Fe_{LMM} and O_{KLL} for as-fresh and heat treated LSCF. After heat treatment, a substantial increase in peak intensity was observed in Sr while that of La, Co and Fe was decreased. The elemental atomic percents obtained from AES are given in Table 4-1. While the concentration of cations varied, the oxygen concentration remained essentially constant after heat treatment. The enrichment factor, which represents the relative change of concentrations in the surface region, is calculated based on Eq. 4-2. Sr concentration doubled while Fe concentration halved. It should be stressed that the concentration of Co, which has been thought to be catalytically active, was not detected on the surface.

Chemical analysis of the precipitate was conducted using transmission electron microscopy (TEM). Figure 4-6a is a bright field image of the cross section of the precipitate on the LSCF surface. The TEM micrograph shows the presence of a transition region below the precipitate on the top surface, which is marked by the

brightest region in the figure. The EDS line scan was performed from the inner bulk region to the precipitate on the surface as shown in Figure 4-6a. It shows that the intensity of Sr peak increases in the precipitate region compared to that in bulk and the oxygen peak decreases slightly. By contrast, the peak intensities of other cations decrease substantially in the precipitate. This means that the precipitate is a Sr-O. The decrease of Sr intensity in sub-surface regions indicates that Sr diffuses from the sub-surface region to the surface region.

Figure 4-7 shows the pO_2 dependence of the formation of precipitates. Samples were heat treated at 800°C for 50 hrs in pure N_2 and 0.1% O_2 , which was balanced by Ar. Compared to heat treated samples in air at the same temperature (Figure 4-3d), the formation of precipitates was reduced considerably in 0.1% O_2 (Figure 4-7a). And the formation of precipitates was not found in pure N_2 (Figure 4-7b). Such trends were consistently observed when samples were heat treated at higher temperatures in same environments. Figures 4-7c and 4-7d show the heat treated LSCF surface at 890°C in N_2 and 0.1% O_2 , respectively. It shows also the reduced formation of Sr-O precipitates. This indicates that in addition to temperatures, the oxygen partial pressure is a critical factor affecting the formation of Sr-O precipitates on LSCF surfaces.

Sr enrichment on the LSCF surface after heat treatment at 800°C is evident. As a result, the transition metal concentration decreases. This is in good agreement with previous works. Bucher et al.⁵⁹ found Sr enrichment on the surfaces of LSCF after measuring surface exchange coefficients at $600\text{-}700^\circ\text{C}$. Similarly, Heide⁶⁰ observed Sr enrichment on $\text{La}_{1-x}\text{Sr}_x\text{Co}_y\text{Fe}_{1-y}\text{O}_3$ surfaces after heat treatment at 1000°C in 1% O_2 . While these previous studies on Sr enrichment mostly postulated the formation of SrO

layers on the surface based on the results from chemical analysis, this study clearly shows the formation of submicron-sized Sr-O precipitates on the surface using SEM and TEM. The formation of AO precipitates on the surface was previously shown in other ABO₃ perovskite materials,⁶⁴⁻⁶⁶ but the formation of the Sr-O precipitate on LSCF surfaces was visualized for the first time in the present study.

Generally, elemental enrichment and precipitation is related to defect structures, especially the presence of point defects.⁷⁴⁻⁷⁷ As La_{1-x}Sr_xCo_yFe_{1-y}O₃ exhibits a substantial oxygen deficiency above 600°C,^{34, 45} oxygen vacancies may contribute to Sr-O precipitation. Even though oxygen vacancies improve the oxygen reduction reaction on the surface and oxygen diffusion in the lattice, their presence reduces the stability of the structure by increasing repulsive forces between like atoms. The effect of oxygen vacancies on bonding strength was experimentally demonstrated by Wang et al.⁶⁷ They found that the elastic modulus of ceria decreases drastically as the oxygen vacancy concentration increases. This is because oxygen vacancies weaken the attractive forces. The formation of oxygen vacancy in the lattice can be written as Eq. 4-3 using Kroger-Vink notation.

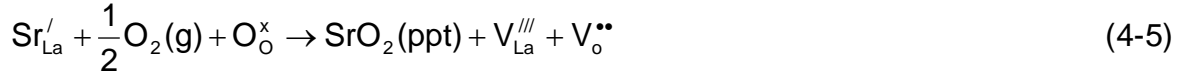


Figure 4-8a shows the schematic of the (100) plane of a cubic perovskite structure. Due to originally broken bonding, atoms on the surface are unstable compared to those in bulk. If oxygen ions are removed from the lattice according to Eq. 4-3, the shielding effect between cations will be removed and atoms in the surface region will become more unstable. Thus, in order to reduce the excess surface energy corresponding to unstable surfaces, it is probable that some cations near the surface region precipitates

on the surface, yielding cation vacancies in the lattice as demonstrated in Figure 4-8b. As the binding of A-O is generally weaker than the binding energy of B-O in the ABO_3 perovskite structure, the precipitation of A site cations will be more energetically favorable than the precipitation of B site cations.^{68, 69} Therefore, enriched Sr in LSCF is likely to precipitate into Sr-O to reduce the excess surface energy caused by oxygen vacancy formation.

LSCF was heat treated at the same temperatures over various pO_2 ranges from pure N_2 to air. At lower pO_2 , LSCF exhibits a higher oxygen vacancy concentration, resulting in increased probability for precipitate formation. However, LSCF shows reduced formation of Sr-O precipitates with decreasing pO_2 . A similar pO_2 dependence of elemental enrichment was reported by Dufour et al.⁷⁰ They found that the ratio of Ba to Ti on the surfaces of $BaTiO_3$ became doubled after heat treatment at $1300^\circ C$ in air, but the ratio was decreased to 1.4 when surfaces were heat treated in N_2 . This indicates reduced Ba enrichment at lower pO_2 . Szot et al.⁶⁸ studied the nature of the surface layer in ABO_3 perovskite structure materials such as $SrTiO_3$ and observed the formation of A-O layers at elevated temperatures, which is known as the Ruddlesden-Popper (RP) phase.⁷¹ They propose that the RP phase is likely to be more stable at high pO_2 and therefore the formation of A-O layers can be inhibited at reduced pO_2 . The formation of Sr-O precipitates on LSCF surfaces can be understood by a two-step mechanism: (i) the formation of oxygen vacancies, and (ii) subsequent precipitation of enriched Sr. Step (i) increases with decreasing pO_2 but step (ii) occurs at oxidizing conditions, i.e. at high pO_2 . As LSCF exhibits a high oxygen vacancy concentration in oxidizing conditions, the overall reaction is likely to be controlled by step (ii). Königstein et al.⁷² reported that

thermodynamically stable compounds of Sr-O are SrO and SrO₂. The step (ii) for Sr-O precipitation, then, can be written as



The crystal structure of precipitates was analyzed using low angle XRD but the presence of either SrO or SrO₂ could not be identified due to the limited amount of the secondary phase. So, it can not be concluded decisively which reaction is more dominant. However, the reaction increasing hole concentration is likely to be thermodynamically unfavorable because the formation of holes increases the concentrations of Co⁴⁺ and Fe⁴⁺, which are unstable species at high temperatures.⁸ A further systematic quantum mechanical study is required to conclude the dominant reaction mechanism.

Recently, Simner et al.³⁸ measured power density of anode-supported cells utilizing LSCF cathodes over long term periods at 750°C and observed decrease in the cell performance. Similarly, Tietz et al.⁷³ also reported substantial degradation of LSCF cathode based cells during long term testing. Obviously the formation of Sr-O precipitates on the surfaces of LSCF cathodes can contribute to such degradation of cell performance during the test. The oxygen reduction reaction at the cathode consists of a series of elementary steps such as

- i. Gas phase diffusion
- ii. Adsorption of molecular oxygen ($\text{O}_2(\text{g}) + \text{s}_{\text{ad}} \rightarrow \text{O}_2(\text{ad})$)
- iii. Dissociation into atomic oxygen ($\text{O}_2(\text{ad}) \rightarrow 2\text{O}(\text{ad})$)

- iv. Charge transfer ($O(ad) + 2e' \rightarrow 2O''(ad)$)
- v. Incorporation of oxygen ions ($O'' + V_O^{**} \rightarrow O_o^x$)

where s_{ad} is the oxygen adsorption sites on the surface. Sr-O is an electronically insulator.⁷⁴ The collected data of the surface exchange coefficients and the oxygen tracer diffusion coefficients of various metal oxides evidence that the electronic species on the surface are essential for oxygen exchange reaction.⁴² It is expected that the formation of Sr-O precipitate on the surface of LSCF forms a passive layer, reducing the concentration of electronic species and inhibiting oxygen reduction reaction, especially charge transfer. In addition, for ABO_3 perovskite materials, it is generally believed that B site transition metals play a critical role for catalytic activity.^{26, 66-68} Takeda et al.⁴⁴ measured the cathodic polarization of $La_{0.7}Sr_{0.3}MO_3$ (M=Cr, Mn, Fe, Co) and found that $La_{0.7}Sr_{0.3}CoO_3$ exhibited the lowest polarization at 800 °C in air. Kilner et al.³¹ investigated the dependence of surface exchange coefficients (K_o) on the composition of $La_{0.8}Sr_{0.2}Mn_{1-y}Co_yO_3$ and found that K_o increased with increasing Co concentration. Kan et al.⁵⁴ studied the effect of catalyst impregnation on the catalytic activity for oxygen exchange for $La_{0.8}Sr_{0.2}MnO_3$ (LSM). They found oxygen exchange reaction was improved with the addition of Co on LSM surfaces via wet impregnation. The results in literatures indicate that Co is a catalytically active element for oxygen reduction reaction. Consequently, deficiency of catalytically active transition metals due to Sr enrichment is likely to further reduce oxygen reduction reaction. Thus, Sr-O precipitation on LSCF surfaces can cause substantial increases in non-ohmic resistance. It can also lead to increases in ohmic resistance if Sr is enriched at the interface of LSCF and other cell components, forming secondary phases such as $SrZrO_3$ or $SrCrO_4$.^{46, 85}

4.4 Conclusions

LSCF surfaces exhibit substantial compositional variations in oxidizing condition at elevated temperatures. This heterogeneous surface structure involves Sr enrichment and subsequent precipitation into submicron sized Sr-O on the surface. A two-step mechanism was proposed for Sr-O precipitation: (i) the formation of oxygen vacancies, and (ii) subsequent precipitation of enriched Sr. As LSCF exhibits high oxygen nonstoichiometry at elevated temperatures, it is likely that step (ii) controls the overall reaction. Sr-O is electrically insulating and Sr enrichment results in the depletion of transition metals. Consequently, the heterogeneous surface structure can lead to substantial degradation of the surface catalytic activity for LSCF.



Figure 4-1. Brief description of sample preparation procedure.

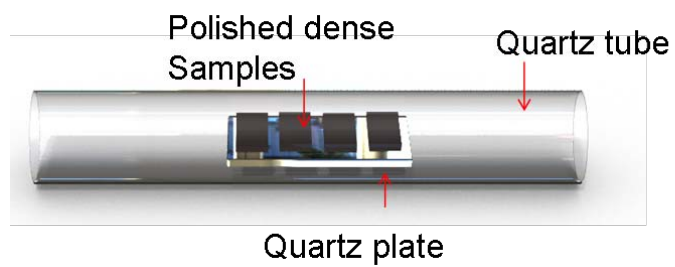


Figure 4-2. Heat treatment set-up.

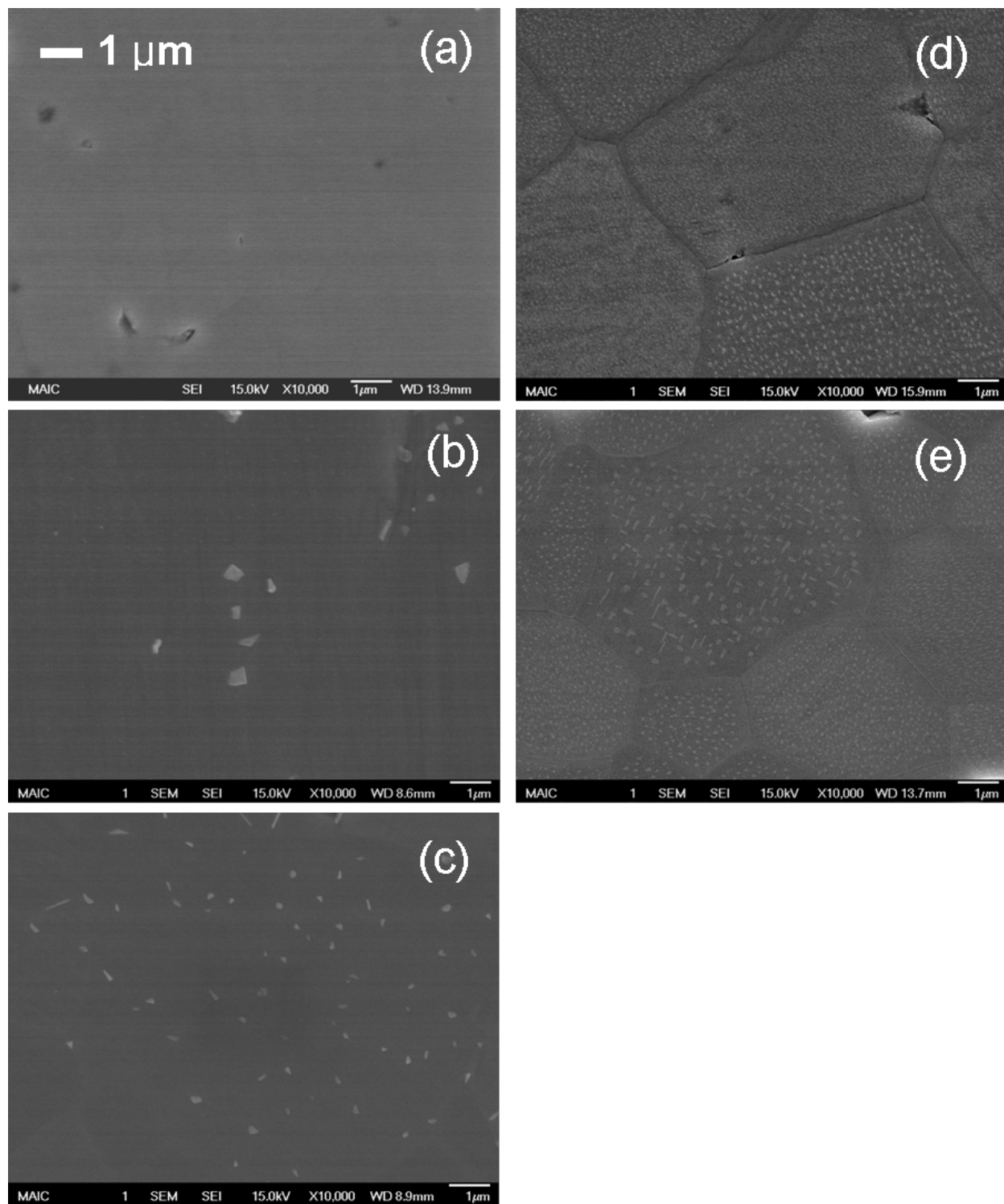


Figure 4-3. SEM micrographs of LSCF of (a) before heat treatment and after heat treatment at (b) 600°C, (c) 700°C, (d) 800°C and (e) 900°C for 50 hours in the absence of Fe-Cr alloy.

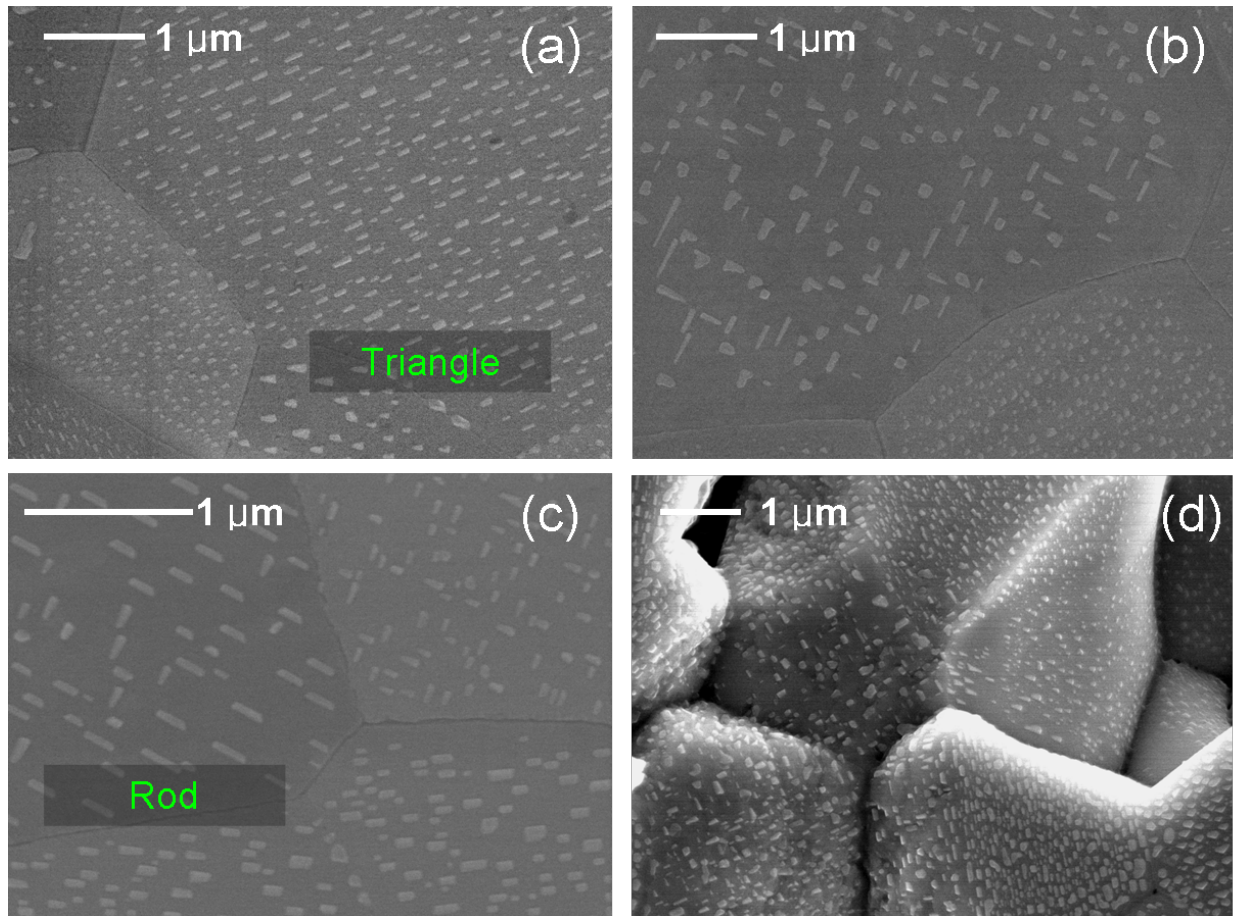


Figure 4-4. Magnified images of the precipitates on LSCF surfaces after heat treatment at (a) 900°C for 50 hours, (b) 900°C for 50 hours, (c) 860°C for 100 hours, and (d) 890°C for 100 hours.

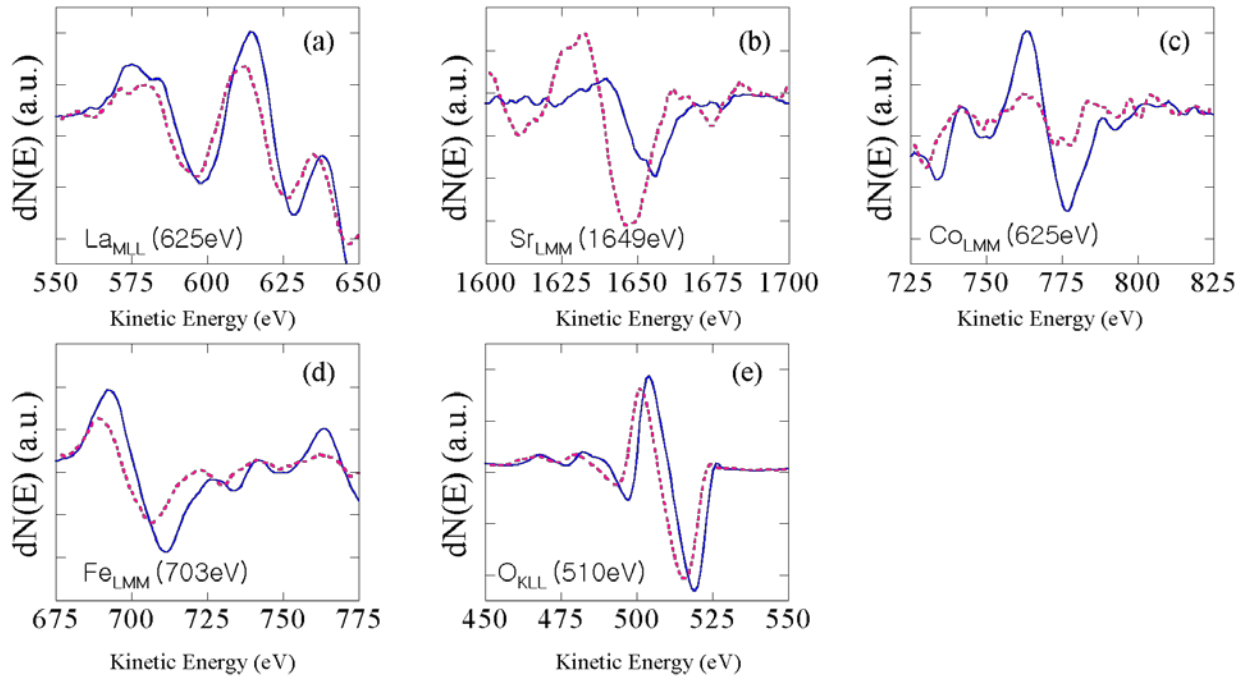


Figure 4-5. Differentiated Auger electron spectra of the (a) $La_{M_{LL}}$, (b) $Sr_{L_{MM}}$, (c) $Co_{L_{MM}}$, (d) $Fe_{L_{MM}}$, and (e) $O_{K_{LL}}$ before (blue solid line) and after (red dotted line) heat treatment at 800°C for 50 hours.

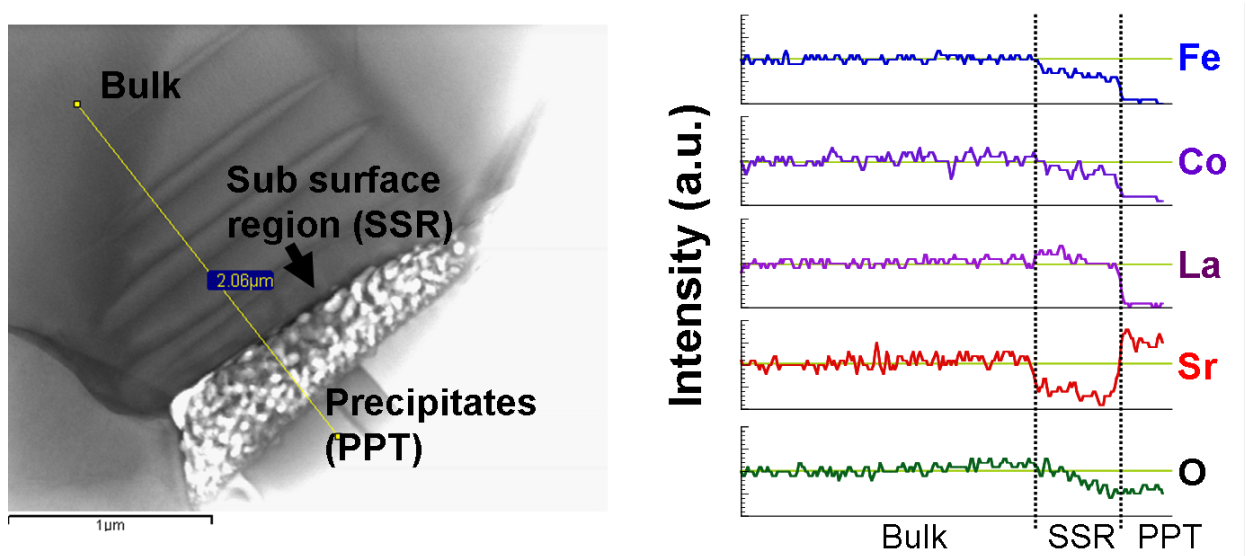


Figure 4-6. TEM bright field image of the cross section of precipitate (left side) and EDS line scan of selected elements (right side)

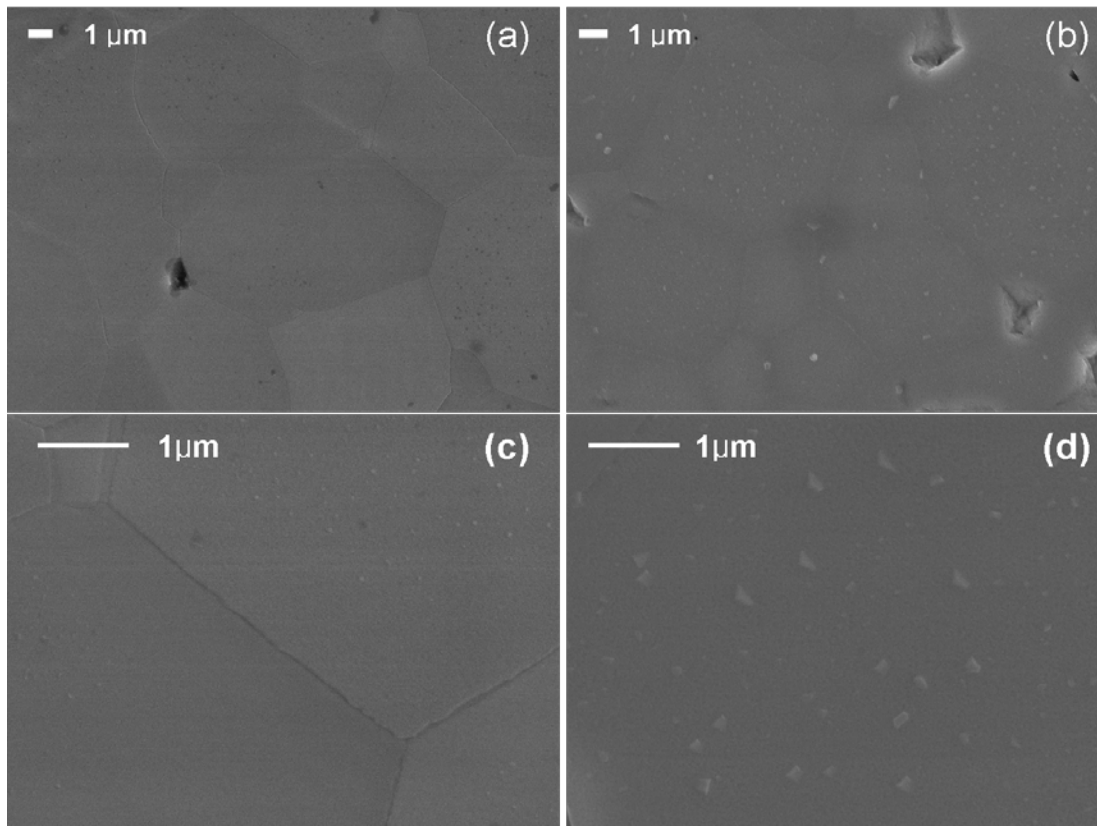


Figure 4-7. SEM micrographs of LSCF surfaces after heat treatment for 50 hours at (a) 800°C/ N₂, (b) 800°C/0.1% O₂ (c) 890°C/N₂ and (d) 890°C/0.1% O₂

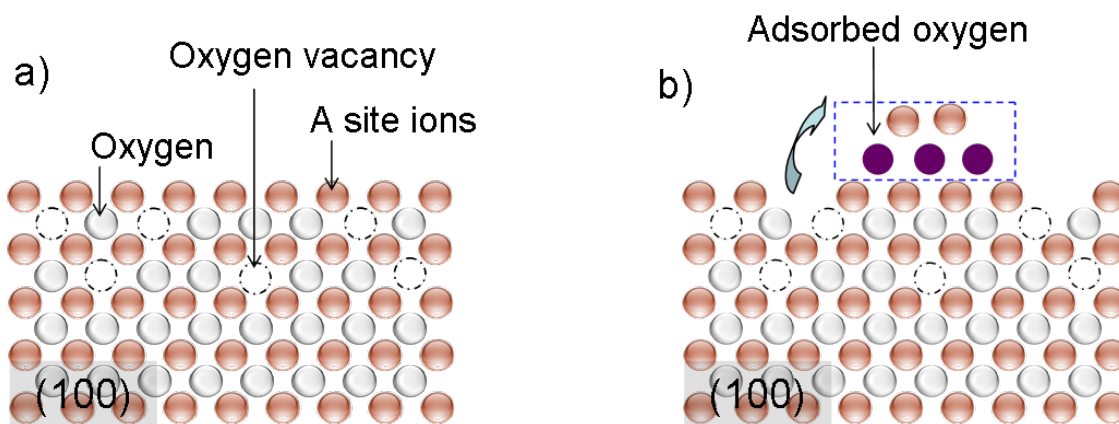


Figure 4-8. Schematic diagram of (a) the formation of oxygen vacancies and (b) formation of cation and anion vacancies simultaneously.

Table 4-1. Elemental atomic percents (%) of pre-and post-heat treated LSCF at 800°C obtained from EDS and AES.

EDS		La	Sr	Co	Fe	O
	As-fresh	12	9	4	14	61
	After heat treatment	13	9	4	15	59
AES		La	Sr	Co	Fe	O
	As-fresh	30	12	5	11	42
	After heat treatment	28	22	0	7	43
	Enrichment factor	0.9	1.8	0	0.6	

CHAPTER 5
IMPACT OF CO IMPREGNATION INTO LSCF CATHODE ON SOFC
PERFORMANCE

5.1 Introduction

Recently the mixed ionic electronic conductor (MIEC) has been widely used for a solid oxide fuel cell cathode due to the high ionic and electronic conducting properties^{22, 41} They have also exhibited enhanced catalytic activity for oxygen reduction compared to the pure electronic conductor.⁴² However, an attempt to reduce operating temperatures causes the reduced rate of oxygen reduction reaction (ORR), which results in a substantial increase in activation overpotential. Therefore, tremendous efforts have been done in order to improve the cathode performance.^{42, 75-79} Since the ORR is a heterogeneous reaction, the interaction between the cathode and oxygen is primarily affected by surface characteristics. Thus, enhancing surface catalytic activity by dispersing nano-sized particles on the surfaces of the porous electrodes can lead to an improvement in cathode performance.^{91, 92}

Previously, precious metals were impregnated into the LSCF cathode in order to enhance the LSCF performance. This method is used to deposit catalytically active fine particles on the surface of a porous electrode backbone as described in Figure 5-1. Sahibzada et al.⁸⁰ investigated the effect of the addition of Pd into the porous $\text{La}_{0.6}\text{Sr}_{0.4}\text{Co}_{0.2}\text{Fe}_{0.8}\text{O}_{3-\delta}$ (LSCF) cathode and observed 3–4 times lower cathodic impedance in the temperature range of 400–750°C after Pd impregnation. Similar enhanced cathode performance by addition of Pd or Pt was also reported by Simner et al.⁸¹ and Uchida et al.⁸² However, from the economic point of view, it is advantageous to use abundant elements for the reduction of manufacturing costs. Yamahara et al.⁸³ tested impact of Co impregnation into the $\text{La}_{0.85}\text{Sr}_{0.15}\text{MnO}_3$ cathode and found

reasonable increase in maximum power density and decrease in electrode resistance after impregnation. However, the impact of Co impregnation into the LSCF cathode has not been tested yet.

It is reported that the chemical composition of the LSCF surface is substantially different from the stoichiometric values. Viitanen et al.⁶¹ studied the chemical compositional change of LSCF after an oxygen permeation experiment at 900°C using X-ray Photoelectron Spectroscopy (XPS). They observed the absence of Co and Fe in the outermost atomic layer from contamination-free LSCF. Bucher et al.⁵⁹ found Sr enrichment on the surface using XPS after measuring surface exchange coefficient of LSCF at 600-700°C. Oh et al.⁸⁴ showed that Sr in LSCF not only enriched on the surface but also precipitated into SrO under an oxidizing condition. They observed reduced concentration of transition metals on the surface in accordance with SrO precipitation. Vance et al.⁸⁵ and Lee et al.⁸⁶ reported that excess Sr increases the electrode resistance. It is generally believed that B site transition metals play a critical role for catalytic activity of ABO_3 perovskite materials.^{24, 69, 87, 88} Therefore, Sr enrichment, can degrade the surface catalytic activity. In this study, cobalt oxide was additionally dispersed into the porous LSCF cathode instead of precious metals in order to improve LSCF performance. The impact of Co impregnation was tested by measuring the electrode resistance and cell performance.

5.2 Experimental

5.2.1 AC Impedance Analysis

A symmetric cell, which consists of LSCF/GDC/LSCF, was prepared for the impedance measurement. A dense $Gd_{0.1}Ce_{0.9}O_{2-δ}$ (GDC, Anan Kasei, Japan) electrolyte was made by sintering a pressed pellet at 1450°C for 4 hours. A LSCF ink was

prepared by mixing LSCF powder with texanol based polymer vehicle (ESL electro-science, USA) using Thinky mixer (Thinky, Japan). The ink was symmetrically painted on both sides of the electrolyte, each having a same electrode area of 0.28 cm². Pt wires were connected as a current collector and LSCF ink was applied for better contact. After that, the cell was sintered at 1100°C for 1 hr with heating and cooling rate of 5°C/ mins.

Figure 5-2 shows the LSCF/GDC/LSCF symmetric cell and the schematic of AC impedance measurement set-up. AC impedance of the symmetric cells was measured in air in the temperature range between 600 and 800°C with 50°C intervals using a Solartron SI 1260 frequency response analyzer. The amplitude of the excitation voltage was 50 mV and the AC frequency range was from 0.1 to 10⁵ Hz. The experimental data was fit using the equivalent circuit shown in Figure 5-3 in order to de-convolute the impedance response and extract the electrode resistance. It consists of a series of resistors (R) and constant phase elements (CPE). CPEs were used instead of capacitors to fit the depressed semi-circle behavior.⁸⁹ In the figure, R_E is the electrolyte ohmic resistance, and R_{HF} and R_{LF} refer to high and low frequency components respectively. The overall electrode resistance is the sum of R_{HF} and R_{LF}. The area specific resistance of the electrode is obtained by

$$ASR_{\text{Electrode}} = \frac{(R_{\text{HF}} + R_{\text{LF}}) \cdot \text{Area}_{\text{Electrode}}}{2} \quad (5-1)$$

5.2.2 Electrical Conductivity Relaxation

A dense LSCF sample was prepared for analysis. It was prepared by pressing La_{0.6}Sr_{0.4}Co_{0.2}Fe_{0.8}O_{3-δ} powder (Praxair Specialty Ceramics, USA) uni-axially and sintering a pellet at 1400°C for 4 hours in air. The density of the sintered body

measured by the Archimedes method was ~ 97% of the theoretical value (6.36 g/cm³). The sintered body was cut and then polished with a series of SiC papers and diamond abrasives (Leco) down to 1 μm. All samples were cleaned with DI water and acetone before ECR test. The sample dimension was approximately 0.1x2x20 mm³.

A bar of LSCF was positioned on the alumina tube in the middle of the reactor and a K-type thermocouple was placed below it. A N₂ and O₂ gas mixture was fed into the reactor through a mass flow controller (MKS & Edwards). The total flow rate was fixed at 300 ccm. The electrical conductivity was measured via the four point probe method. The conductivity change was monitored by a Lock-in amplifier (Stanford, SR830) automated with Labview software. The sample was heated to 800°C at a rate of 5°C/min in air. Before the ECR measurement, the feed stream was switched to 3% O₂. Once it reached steady state the feed stream was switched via four way switching valve. The oxygen partial pressure (pO₂) step was programmed to increase by the following steps: 3→5→8→12→18→28→43→67%.

5.2.3 Button Cell Fabrication and Tests

NiO-GDC anode supports were fabricated by the tape-casting method. A tape casting slurry was prepared in two steps. First, a mixture of NiO (Alfa Aesar), Ce_{0.9}Gd_{0.1}O_{1.95} (Anan), and a dispersant, Solsperse, was ball milled in a toluene and ethanol solvent system for 24 hours. After that, a plasticizer, di-n butyl phthalate (DBP) and polyethylene glycol 5000 (PEG5000), and a binder, polyvinyl butyral (PVB), were added to the slurry. After 24 hours, the slurry was de-gased to remove trapped air bubbles, which cause cracks or defects during casting. The NiO-GDC anode tape was tape casted using a Procast tape casting system (DHI) and then the tape was dried for 2 hours at 100°C. Circular shapes of green tape (dia. 32 mm) were cut out and partially

sintered at 900°C for 2 hours to remove polymer vehicles as well as provide an appropriate mechanical strength for the electrolyte deposition.

An anode functional layer was added to increase SOFC performance. An ethanol based GDC precursor solution was spray coated on the surface of a pre-sintered anode and heat treated at 900°C for 1 hour. An electrolyte was then deposited on the top functional layer. A GDC electrolyte slurry, which was prepared by ball-milling GDC powder, Solsperse, PVB and DBP in ethanol, was spin-coated on the pre-sintered body and dried at room temperature for 10 hours. Finally, it was sintered at 1450°C for 4 hours using a heating rate of 3°C/ min. A LSCF cathode ink was brush-painted on the electrolyte. The cathode was fired at 1100 °C for 1 hour. Pt paste, as a current collector, was brush-painted onto both electrodes along with Pt mesh and gold leads. Current collectors were heat-treated at 900 °C for 1 hour.

Figure 5-4 shows a diagram of the current density and voltage measurement set up. The button cell was loaded in a house-built fuel cell testing setup and gas sealed using a two-part ceramabond sealant (a mixture of 517-powder and 517-liquid from Aremco). 30 ccm of dry air and 30 ccm of wet hydrogen were supplied to the cathode and anode sides, respectively. The cell voltage was measured as a function of current density using a Solartron 1287 potentiostat. Impedance was measured at open circuit conditions by two-point probe methods using a PARSTAT 2273 frequency response analyzer (Princeton Applied Research) with a frequency range of 0.1 to 10⁵ Hz. The electrode area specific resistance (ASR) was calculated from the area below the semi-circle in the Nyquist impedance plot.

5.2.4 Catalyst Impregnation

A Co precursor solution was prepared by dissolving $\text{Co}(\text{NO}_3)_2 \cdot 6\text{H}_2\text{O}$ (Alfa Aesar 99.999%) in ethanol and its pH was measured using a pH meter (Seven multi, Mettler Toledo). The Co precursor was impregnated into the porous body of the cathode by dipping the cell into the Co nitrate solution while a vacuum was pulled. NiO-GDC Anode was dense before reduction in H_2 condition, and so Co solution was barely impregnated into anode side. Co impregnation was continued until no more air bubbles came out from the surface of the cathode. It was taken from the solution and dried at 70°C . The electrolyte area around the electrode was cleaned in ethanol and then heat-treated at 850°C for 30 mins.

5.2.5 Characterization

The morphological change was characterized using scanning electron microscopy (SEM, JSM 6335F) combined with energy dispersive spectroscopy (EDS, Oxford, UK). ZAF correction is used for semi-quantitative analysis, where Z is the atomic number, A is the absorption correction factor, and F is the fluorescence correction factors.

5.3 Results and Discussion

5.3.1 Effect of Co Impregnation on Electrode Impedance

ASR-AC impedance spectroscopy measurements were carried out in the temperature range of $600\text{--}800^\circ\text{C}$. Figure 5-5 shows the AC impedance spectra for LSCF/GDC/LSCF symmetric cell at three different temperatures. The area below the semi-circles corresponds to the electrode resistance, and the high frequency intercepts of the semi-circles were normalized for easier comparison. There are approximately two semi-circles, and each semi-circle corresponds to a different reaction step.⁹⁰ The greatest contribution to the electrode resistance is the high frequency component. As

temperature decreases, the size of the high frequency semi-circle increases, while that of the low frequency semi-circle changes slightly. However, two semi circles were apparently combined into one below 700°C and so they could not be de-convoluted each other. Esquirol et al.⁹¹ and Sahibzada et al.⁸⁰ measured the impedance of LSCF/GDC/LSCF symmetric cell and observed similar behavior. They attributed the high and low frequency components to the surface reaction and gas phase diffusion, respectively. It is expected that the resistance for the surface reaction increases substantially as the temperatures decrease while the mass transport of oxygen gas depends little on temperature. And so their explanation justifies the observed dependence of AC impedance spectra on temperature.

Figure 5-6 shows the impedance spectra for the symmetric cells of plain LSCF and Co impregnated LSCF. It shows that Co impregnation into LSCF reduces R_{HF} while R_{LF} is unaffected, indicating that it does not retard oxygen gas diffusion but improves the surface reaction rate. At temperatures below 700°C it is difficult to distinguish the contribution of the high and low frequency component and so the total electrode ASRs are compared each other. Figure 5-7 shows the $ASR_{\text{Electrode}}$ of plain and Co impregnated LSCF plotted as a function of temperature in log scale. For the plain LSCF electrode, the ASR is $0.040 \Omega \text{ cm}^2$ at 800°C, which is consistent with literature values.⁹¹ The ASR decreases to $0.027 \Omega \text{ cm}^2$ at the same temperature after Co impregnation, providing a 32% reduced value. The activation energies were obtained from Arrhenius plots. They were 1.44 eV and 1.55 eV for plain and Co impregnated LSCF electrodes, respectively. The activation energy is only slightly changed after Cr impregnation. It seems that the rate limiting step does not change with Co impregnation.

$ASR_{\text{Electrode}}$ is related to the surface exchange coefficient (k_o) according to^{100, 102}

$$K_o = \frac{R \cdot T}{z^2 \cdot F^2 \cdot ASR_{\text{Electrode}} \cdot C_o} \quad (5-2)$$

where R is the gas constant, T is the absolute temperature, F is faraday constant, n is the number of electron transferred during the reaction, and C_o is oxygen concentration.

K_o is the apparent rate coefficient of the ORR, in which a series of elementary steps occurs such as⁹²

1. Gas phase diffusion
2. Adsorption of molecular oxygen ($O_2(g) + s_{ad} \rightarrow O_2(ad)$)
3. Dissociation into atomic oxygen ($O_2(ad) \rightarrow 2O(ad)$)
4. Charge transfer ($O(ad) + 2e' \rightarrow 2O''(ad)$)
5. Incorporation of oxygen ions ($O'' + V_o^{**} \rightarrow O_o^x$)

where s_{ad} is the oxygen adsorption sites on the surface. And so the reduction in $ASR_{\text{Electrode}}$ means that one of the elementary reactions becomes faster due to Co impregnation. It is expected that incorporation of oxygen ions remains unaffected. And the resistance for gas phase diffusion was found to remain roughly constant after impregnation. Therefore, one of adsorption, dissociation, or charge transfer process is likely to be activated by Co impregnation.

5.3.2 Effect of Co Impregnation on Power Density of a Single Cell

Figure 5-8 shows the output voltage and power density of single cells as a function of current density. One has a plain LSCF cathode and the other has a Co impregnated LSCF cathode. They showed similar open circuit voltage at 600°C. However the maximum power density is significantly different. The maximum power density of the cell with plain LSCF cathode was around 0.5 W/cm². After Co impregnation, it increased

up to 1.2 W/cm^2 . The gas flow rates were 90 SCCM of wet H_2 (3% H_2O) on anode side and 30 SCCM of air on cathode side. Co impregnation also increased cell performance at 550 and 500°C as seen in Figure 5-8. The maximum power density of button cells was plotted as a function of temperatures between $500\text{-}600^\circ\text{C}$ in Figure 5-8d. Note that these are not composite, but single component cathodes. The maximum power density is high compared to the composite cathode in literatures.^{93, 104}

Factors affecting SOFC performance are complex. In this study, the contribution of electrolyte and electrode was distinguished by measuring the impedance in an open circuit condition. Figure 5-9 compares the impedance spectra of the two cells at 600°C . The reduction in the size of semi-circles is pronounced after Co impregnation, which is in agreement with symmetric cell test. The X-axis intercept is slightly reduced in Co impregnated cell. It seems that the two cells have slightly different microstructure even though they were fabricated at the same time. Post-test analysis shows that they have different thickness of the electrolyte, which was around 15 and $10 \mu\text{m}$ for plain LSCF and Co impregnated cells, respectively. Figure 5-10 is the ASR of electrode and electrolyte, plotted as a function of temperatures. Co impregnation brings a more significant reduction in electrode resistance while electrolyte ASR was decreased slightly. The magnitude of reduction in electrode ASR was higher at lower temperatures. This result indicates that the improvement in cell performance is mostly brought by reduction in electrode resistance. Since Co impregnation does not affect the bulk properties of LSCF cathode such as electronic conduction, the observed reduction in electrode resistance can be attributed to enhanced ORR at the surface and not the reduced in ohmic resistance.

Post-test analysis was conducted using SEM. Figure 5-11a is the SEM micrograph of the cross section of post-tested button cell. And Figure 5-11b is the magnified images for a cathode side. After Co impregnation, deposition of nano sized particles was found on the surface of LSCF cathodes. However, atomic percents obtained from EDS do not provide any noticeable difference between the plain and Co impregnated LSCF cathode. This is because the penetration depth of electron beam is much deeper than the size of the nano sized particle. Previously Yamahara et al.⁸³ impregnated Co nitrate solution into an LSM cathode in similar way to this study, and they observed the formation of Co_3O_4 nano particles using Transmission electron microscopy. And so it is likely that the newly formed nano particle on LSCF is also Co_3O_4 .

The reduced electrode resistance is mostly attributed to the addition of cobalt oxide on LSCF surface. However, the removal of Sr enriched surface layers can also contribute to the improvement in electrode performance. Miura et al.⁹³ tested the oxygen permeability of $\text{La}_{0.6}\text{Sr}_{0.4}\text{Co}_{0.8}\text{Fe}_{0.2}\text{O}_3$ membrane and obtained improved permeability with acid treatment. They performed XPS analysis to identify the reason for activation, and found a reduced concentration of excess SrO on the surface. In this study, a cell was dipped into a nitrate solution during impregnation process. The pH of Co nitrate solution measured was 2.15. This is not a strong acid, but the possibility that a few surface layers were etched during the Co impregnation process cannot be ruled out and may contribute to enhanced ORR.

5.3.3 Characteristic Dependence of K_{chem} on Oxygen Partial Pressure

The chemical exchange coefficient (K_{chem}) and chemical diffusion coefficient (D_{chem}) of LSCF were measured at 800°C using electrical conductivity relaxation. And they are plotted as a function of $p\text{O}_2$ on a log scale in Figure 5-12a. Obtained K_{chem} and

D_{chem} values can be converted into surface exchange coefficients (K_o) and the self diffusion coefficients (D_{self}) using Eqs. 5-3 and 5-4.⁹⁴

$$K_o = \frac{K_{\text{chem}}}{\Gamma} \quad (5-3)$$

$$D_{\text{self}} = \frac{D_{\text{chem}}}{\Gamma} \quad (5-4)$$

where Γ is a thermodynamic factor ($\frac{1}{2} \frac{\partial \ln pO_2}{\partial \ln C_o}$). In addition, the oxygen vacancy

diffusion coefficient (D_v) can be calculated according to⁵³

$$D_v = \frac{D_{\text{self}} \cdot C_o}{C_v} = \frac{D_{\text{self}} \cdot (3 - \delta)}{\delta} \quad (5-5)$$

where C_o and C_v are the concentration of oxygen and oxygen vacancies, respectively, and δ is the molar concentration of oxygen vacancies in $La_{0.6}Sr_{0.4}Co_{0.2}Fe_{0.8}O_{3-\delta}$. The thermodynamic factors and $(3-\delta)/\delta$ values for LSCF at 800°C are given in Table 5-1.^{47, 94} K_o , D_{self} , and D_v were calculated using the values in Table 5-1 and plotted as a function of pO_2 seen in Figures 5-12b and 5-12c, respectively. The slope in the figure indicates the dependence of K and D values on pO_2 . Such dependence must reflect the behavior of oxygen transport mechanisms. For example, D_v is proportional to $pO_2^{0.073}$, which is roughly independent of oxygen partial pressure. This indicates that the mobility of oxygen vacancies is constant in this pO_2 range, which is a reasonable result.

Maier assumed a thin layer, charge-transfer, or adsorption process were rate-limiting steps for the ORR, and set the kinetic models for each case.⁹⁵ The kinetic model provided the characteristic dependencies of apparent rate coefficients on oxygen partial

pressure as Table 5-2 shows. The characteristic dependencies of K_o and K_{chem} on pO_2 , which were obtained in this study, were 0.1 and 0.56 respectively. A comparison of them suggests that the rate-limiting step of the ORR is likely to be a charge-transfer process. Therefore, it is likely that the addition of cobalt oxide on the surface of LSCF reduces the electrode resistance by expediting charge transfer from the cathode to the oxygen gas.

5.4 Conclusions

Based on understanding surface characteristic of LSCF, Co was impregnated into a porous LSCF cathode. After Co impregnation, the electrode ASR was reduced and the maximum power density of a single component LSCF cathode cell was significantly improved, giving 1.2 W/cm^2 at 600°C . This result suggests that Co impregnation into LSCF surface effectively improves deteriorated surface catalytic activity caused by Sr enrichment and transition metal depletion. It seems that the oxygen reduction reaction is limited primarily by a charge transfer process and addition of cobalt oxide via wet impregnation improves this process. Such activation is mainly attributed the addition of cobalt oxide on the surface but the impact of the removal of Sr enriched surface layers during impregnation can not be ruled out. The long-term stability of the impregnated electrode structure needs to be tested.

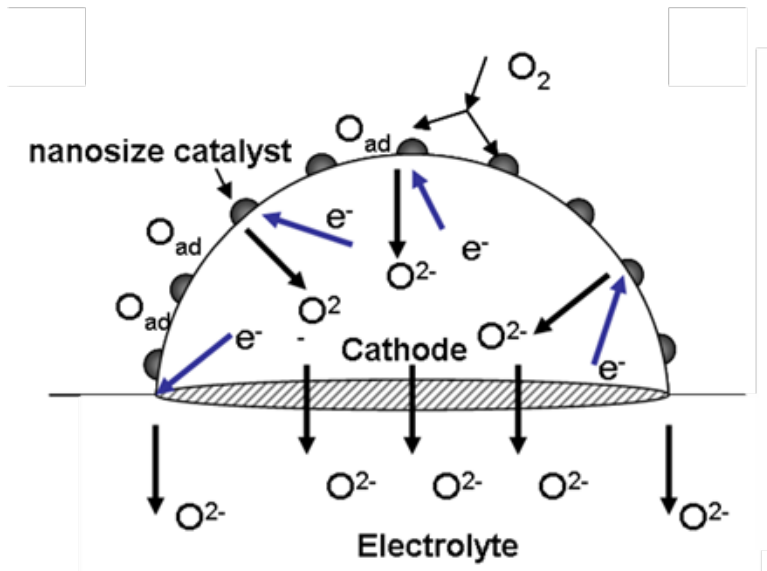


Figure 5-1. Sketch of deposition of nano size particles on cathode surface via wet impregnation.

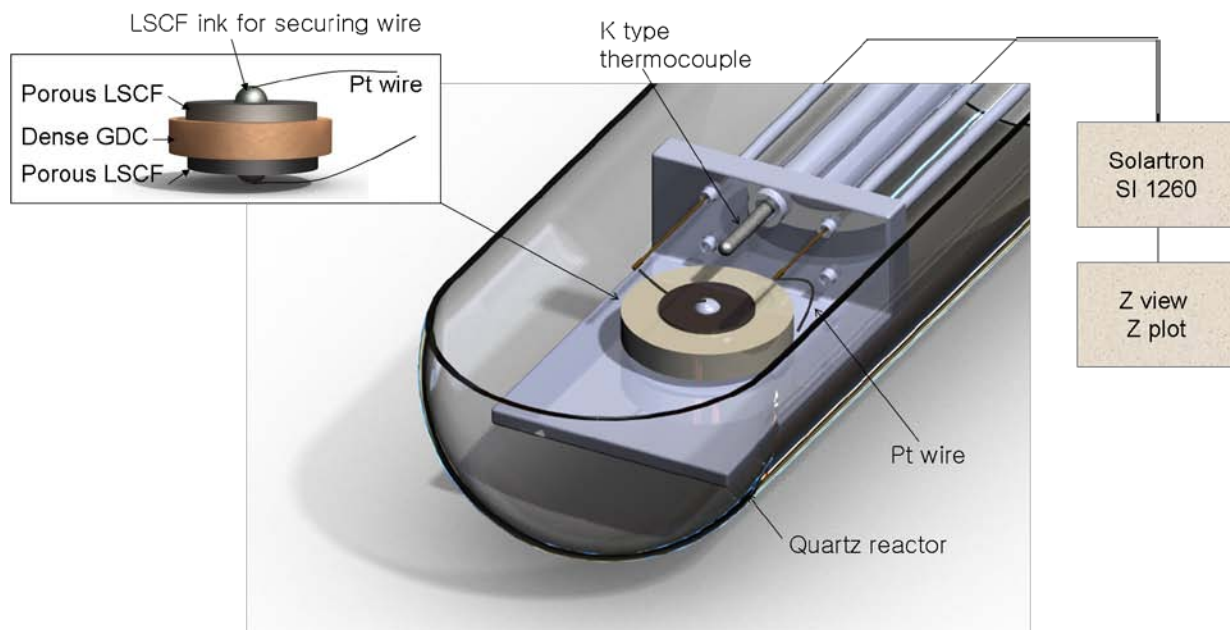


Figure 5-2. Schematic of AC impedance measurements.

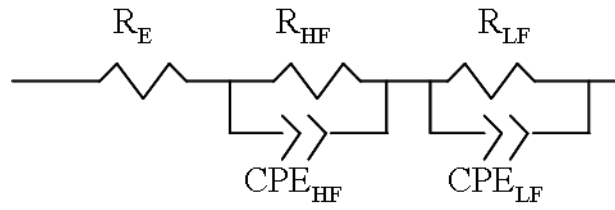


Figure 5-3. Equivalent circuit to fit the measured impedance data.

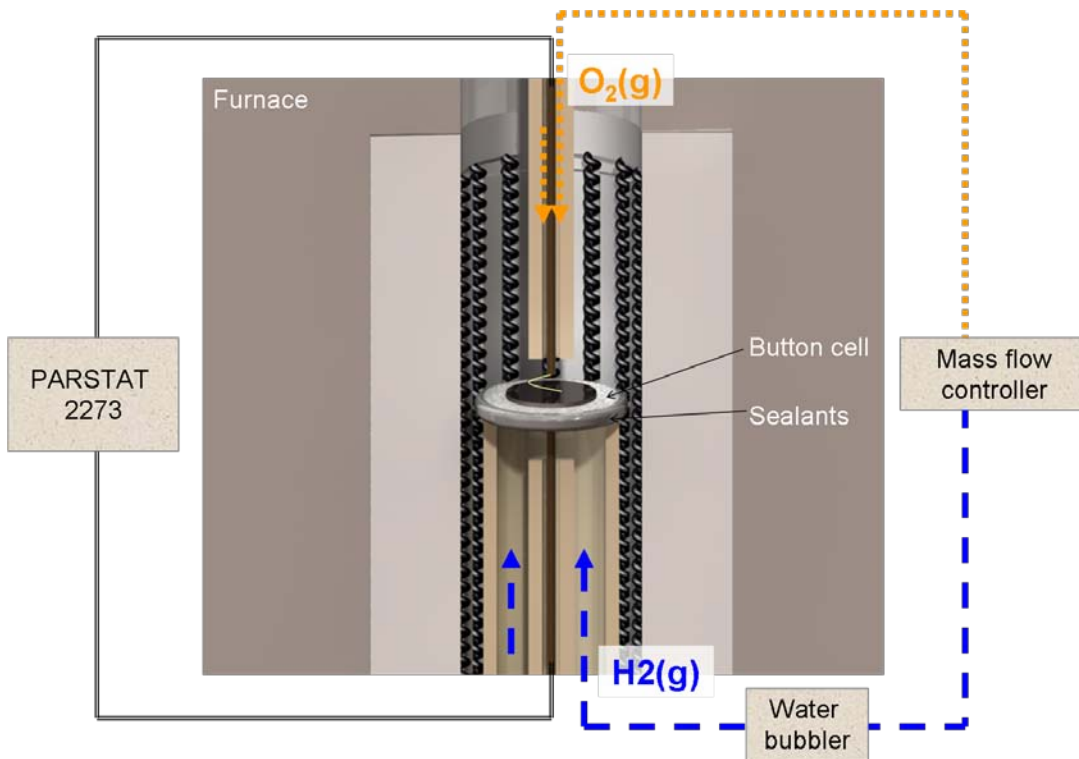


Figure 5-4. Current density and voltage measurement setup

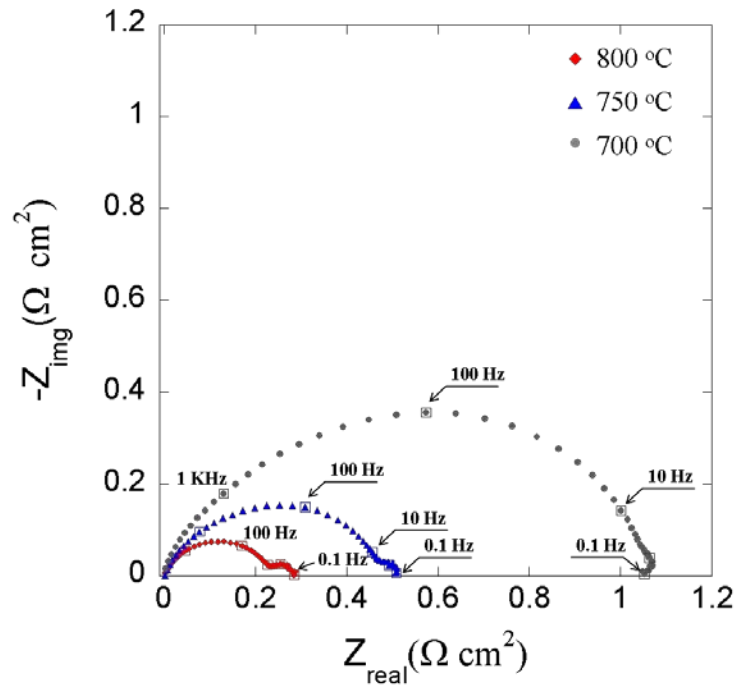


Figure 5-5. AC Impedance spectra of LSCF/GDC/LSCF symmetric cell.

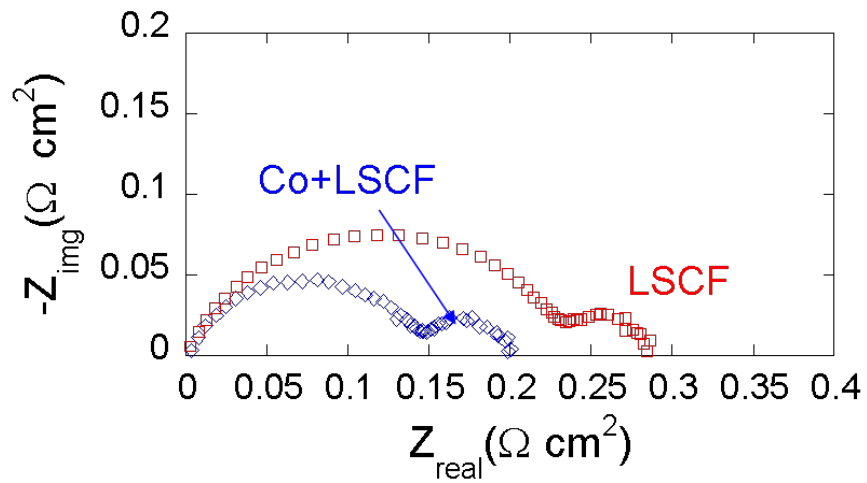


Figure 5-6. Impedance plots for symmetric cell of plain LSCF electrode and Co impregnated LSCF electrode at 800°C in air.

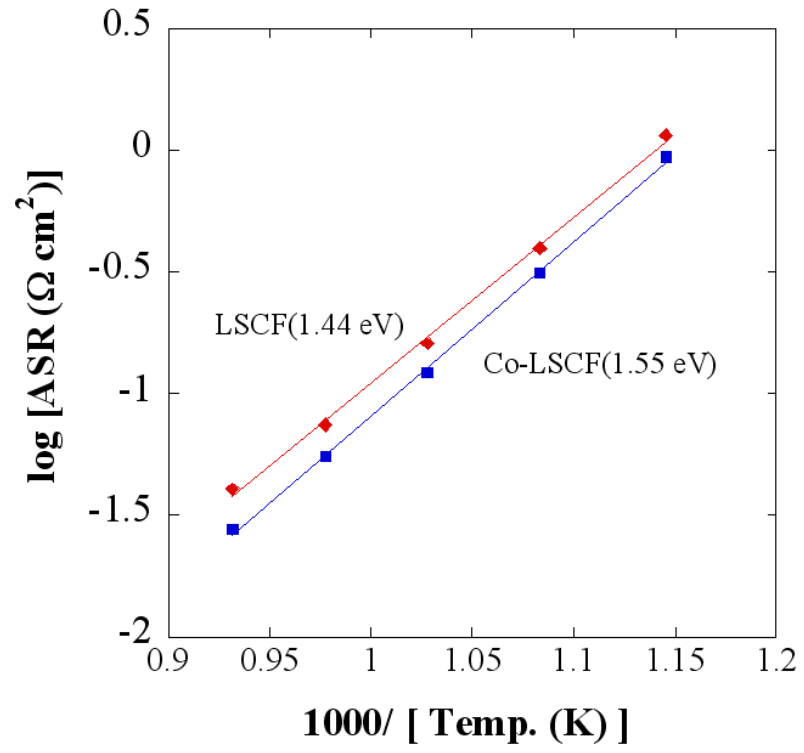


Figure 5-7. Comparison of total electrode ASRs as a function of temperatures

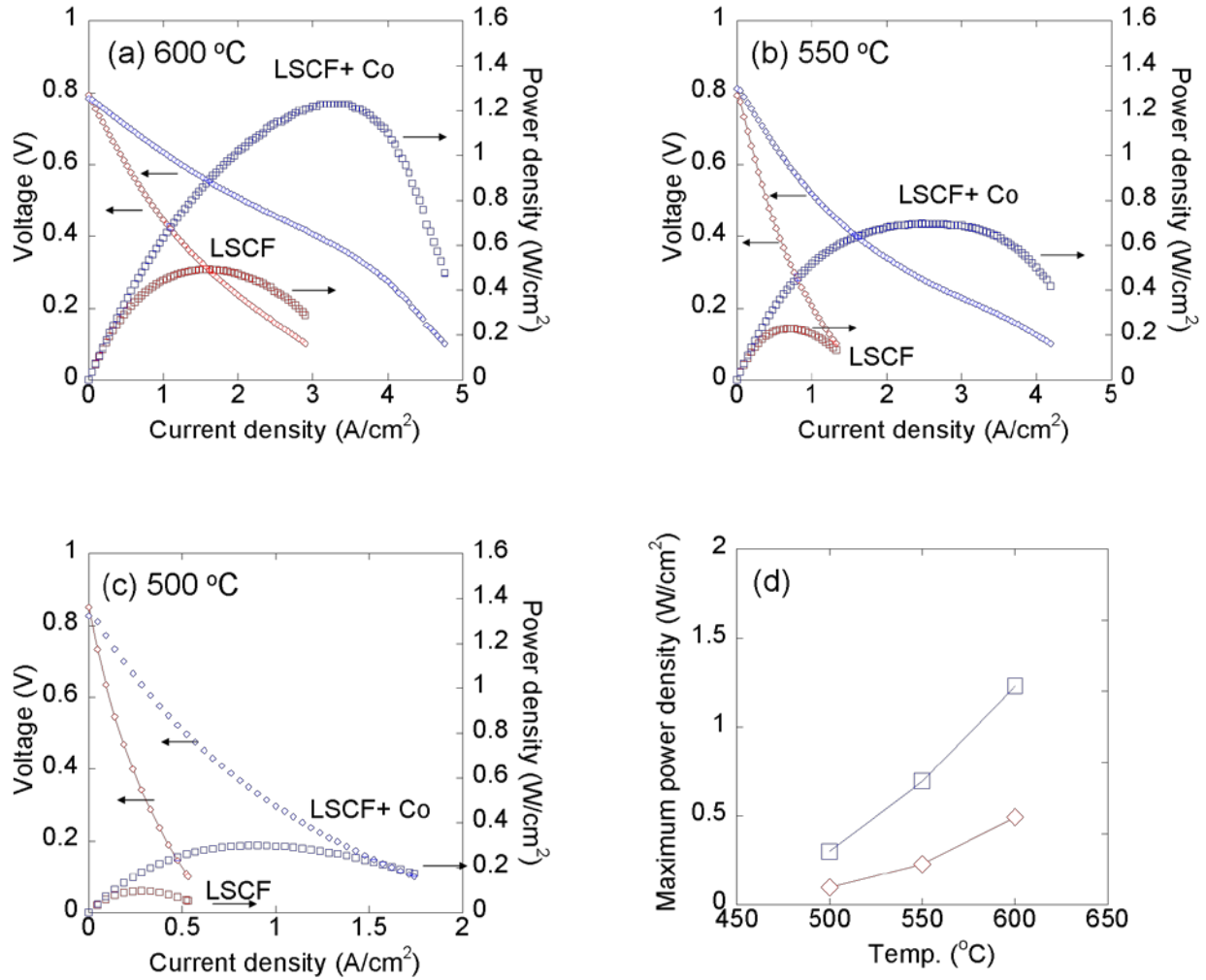


Figure 5-8. Measurement of cell voltage as a function current density at (a) 600°C, (b) 550°C and (c) 500°C. (d) Maximum power densities as a function of temperatures.

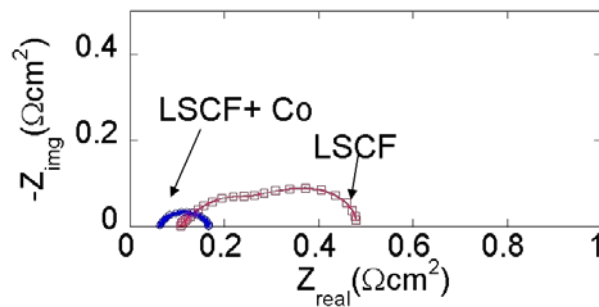


Figure 5-9. Impedance of a button cell for plain LSCF and Co impregnated cathode at 600°C

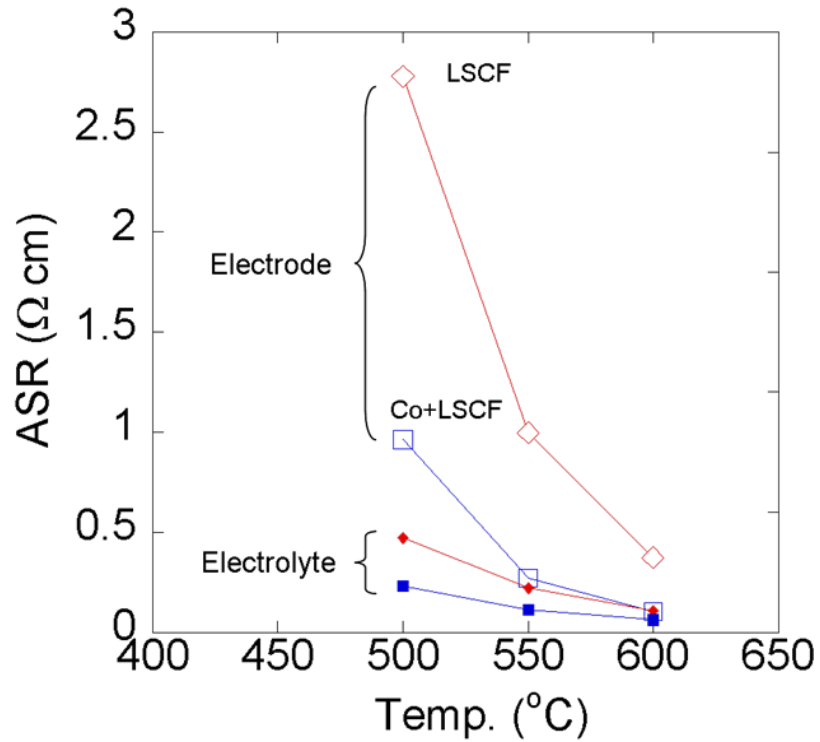


Figure 5-10. The area specific resistance of electrode and electrolyte for plain and Co impregnated LSCF cathode cells.

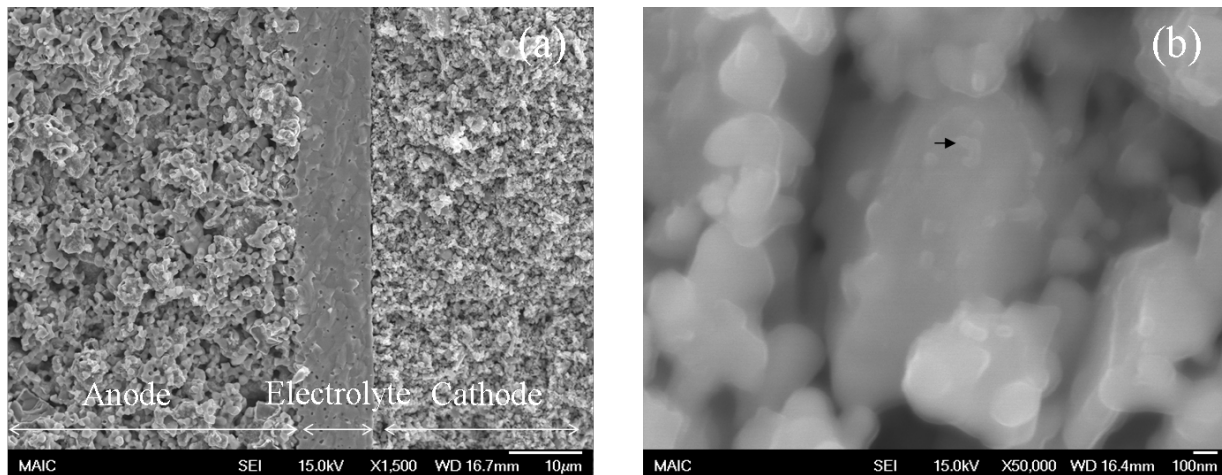


Figure 5-11. (a) SEM micrograph of LSCF/GDC/Ni-GDC button cell and (b) magnified images of Co impregnated LSCF after cell test.

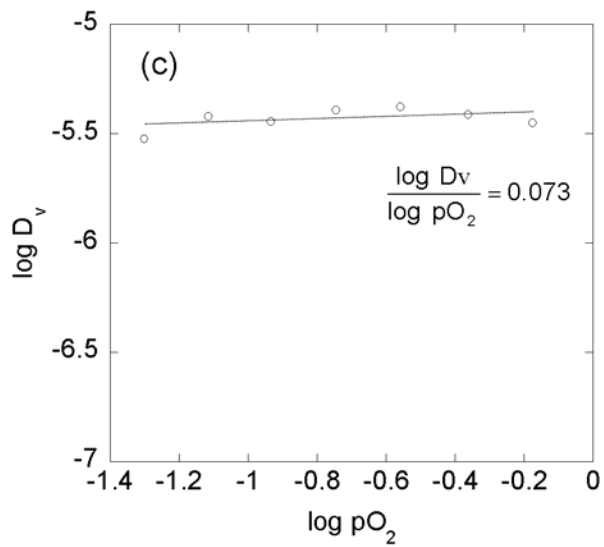
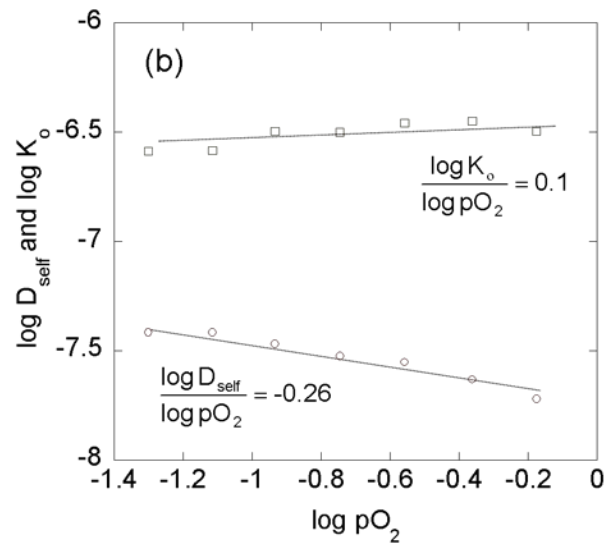
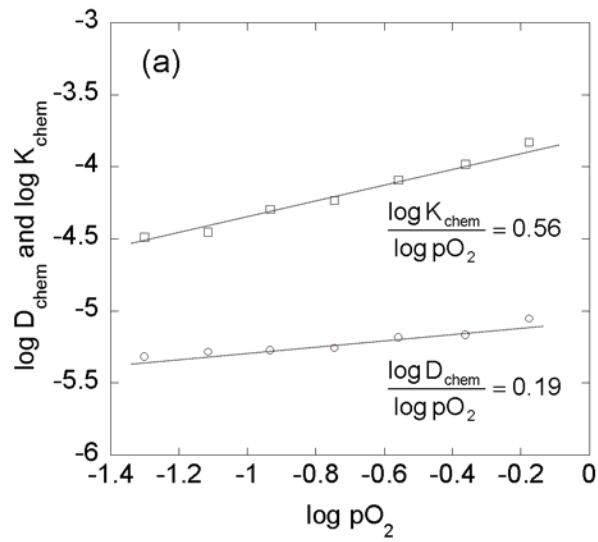


Figure 5-12. (a) D_{chem} and K_{chem} , (b) D_{self} and K_o , and (c) D_v at 800°C as a function of pO_2 .

Table 5-1. Thermodynamic factors and $(3-\delta)/\delta$ of LSCF values at 800°C^{52, 94}

pO ₂	0.05	0.08	0.12	0.18	0.28	0.43
Γ	125.9	135.8	158.5	184.9	232.8	293.1
$(3-\delta)/\delta$	0.0128	0.0101	0.0094	0.0074	0.0067	0.0060

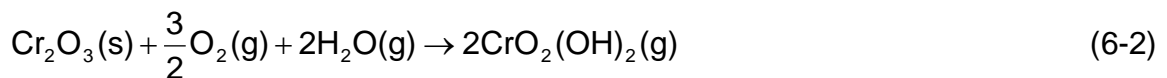
Table 5-2. Characteristic dependencies of the apparent rate coefficients on pO₂.⁹⁵

Controlling parameters	$\frac{\partial \ln k_o}{\partial \ln P}$	$\frac{\partial \ln k_{chem}}{\partial \ln P}$
Thin layer	-1/2	0
Charge transfer	0	1/2
Adsorption	1/2	1

CHAPTER 6
MECHANISM OF CR VAPOR DEPOSITION ON SOFC CATHODES

6.1 Introduction

Solid oxide fuel cells (SOFC) need to be operated as a 'stack' in order to generate practical (high) voltages. The stack consists of multiple single cells, which are electronically connected in series via interconnects. The interconnect also separates oxygen at the cathode side of one cell from the fuel at the anode side of the adjacent cell. Thus, high electronic conductivity, gas tightness, good stability both in air and fuel environment, and low reactivity with other cell components are necessary properties for interconnects.⁹⁶ While ceramic interconnects are generally used for high temperature SOFCs, reduction in the operating temperatures allows utilization of metal alloys. Metal interconnects are advantageous over ceramic interconnects because of reduced manufacturing costs, enhanced machinability and thermo-mechanical stability.^{97, 98} Despite such benefits, metal alloy interconnects contain high concentrations of Cr¹⁴, which leads to out-diffusion of Cr to surface region, formation of Cr scale and Cr vaporization from the Cr scale at high temperatures in oxidizing conditions (Eq. 6-1 and 6-2).



Mass transport of such Cr vapor species to the cathode and the formation of a solid chromium oxide can degrade the cathode performance either by blocking electrochemically active sites or by decomposing cathodes.^{40, 99} SOFCs utilizing metallic interconnects undergo significant degradation during long term operation.^{39, 100}

The long-term stability is an important requirement for the commercialization of SOFC. Thus, the development of a practical SOFC cathode requires an understanding of the degradation mechanism caused by Cr vapor deposition. One group has hypothesized that the degradation mechanism is based on the electrochemical reduction of high valent vapor species of chromium oxide (CrO_3) and oxyhydroxide ($\text{CrO}_2(\text{OH}_2)$) to solid phase Cr_2O_3 .^{40, 101} In contrast, others suggest that the nature of Cr poisoning is a chemical process in which a nucleation agent on the cathode interacts with Cr vapor species.¹¹⁴⁻¹¹⁶ In this study, Cr vapor deposition behaviors on various ABO₃ perovskite materials were systematically investigated in order to better understand the reaction mechanism between Cr vapor species and solid oxide fuel cell cathodes. Dense and polished samples were examined to clearly identify surface morphological changes. A special emphasis was placed on $\text{La}_{0.6}\text{Sr}_{0.4}\text{Co}_{0.2}\text{Fe}_{0.8}\text{O}_3$ (LSCF).

6.2 Experimental

6.2.1 Sample Preparation

$\text{La}_{0.6}\text{Sr}_{0.4}\text{Co}_{0.2}\text{Fe}_{0.8}\text{O}_{3-\delta}$ powder was obtained from Praxair Specialty Ceramics, USA and the rest of the compounds, $\text{La}_{0.6}\text{A}_{0.4}\text{Co}_{0.2}\text{Fe}_{0.8}\text{O}_3$ (A=Ca, Ba), $\text{SrCo}_{0.2}\text{Fe}_{0.8}\text{O}_3$, and $\text{La}_{0.6}\text{Sr}_{0.4}\text{MnO}_3$, were synthesized by a solid state reaction process. La_2O_3 (Cerac, 99.999%), SrCO_3 (Johnson Matthey, 99%), BaO (Acros, 90%), Co_3O_4 (Alfa Aesar, 99.7%) and Fe_2O_3 (Alfa Aesar, 99.945%) powders, were ball milled for 24 hrs in ethanol, and dried at 70°C. They were calcined at 900°C for 6 hrs. LSCF and LSM were sintered at 1400°C for 4 hours and 1450°C for 6 hours, respectively. And the others were sintered at 1200°C for 6 hours. The sintered body was cut and then polished with a series of SiC papers and diamond abrasives (Leco) down to 1 μm. All samples were

cleaned with DI water and acetone before heat treatments. Final sample thicknesses were around 0.1 cm. The compositions of metal oxides and preparation method are listed in Table. 6-1.

6.2.2 Heat Treatment

Samples were heat treated under ambient conditions in the presence of Crofer22APU as described in Figure 6-1. Crofer22APU (ThyssenKrupp VDM, Werdohl, Germany) is a ferritic stainless steel for solid oxide fuel cell interconnects. The composition of the steel, given by the supplier, is listed in Table 6-2. Samples were located on a Crofer22APU sheet, thus the distance between the sheet and sample surfaces is 0.1 cm, which was equivalent to sample thickness. They were also located 0.5 cm away from the sheet. Heat treatments were carried out for 50 hours at 400, 600 and 800°C with heating and cooling rates of 5°C/min. Because no Cr vapor deposition was found at 800°C on LSM, it was heat treated additionally at 1050°C for 50 hours.

6.2.3 Characterization.

X-ray diffraction patterns (Philips APD 3720) of the samples were measured with Cu-K_{α1} radiation ($\lambda=1.54\text{\AA}$). Low angle mode XRD (Philips MRD X'Pert System) was applied in order to analyze the structural variation of LSCF in surface region after heat treatment. All data were compared to the literatures and the Joint Committee on Powder Diffraction Standards Data (JCPDS).

Morphological and compositional changes were characterized using scanning electron microscopy (SEM, JSM 6335F) combined with energy dispersive spectroscopy (EDS, Oxford, UK). ZAF correction was used for semi-quantitative analysis. In addition, surface chemical composition of LSCF before and after heat treatment was measured using Auger electron spectroscopy (AES, AES Perkin-Elmer PHI 660). The accelerating

voltage was 10 kV and it scanned the energy ranges between 50 to 2050 eV, which covered the characteristic peaks of La_{MNN} (625 eV), Sr_{LMM} (1649 eV), Co (775 eV), Fe_{LMM} (703 eV), and O_{KLL} (510 eV). These characteristic peaks were selected in order to minimize interference with each other. Obtained AES spectrum was differentiated, and elemental atomic percents were calculated using AugerScan 3.2.0 software (RBD Instrument). It calculates the atomic percents (X) according to

$$X = \frac{I_a/S_a}{\sum I_m/S_m} \quad (6-1)$$

where I is the peak intensity and S is the relative elemental sensitivity factor for the Auger line used. The relative sensitivity factors, which are provided by RBD instruments, are 0.06, 0.045, 0.19, 0.13, and 0.35 for La_{MNN}, Sr_{LMM}, Fe_{LMM}, Co_{LMM} and O_{KLL}, respectively. This study calculated the relative change based on the ratio of atomic percents before and after heat treatment which were normalized by oxygen concentration. The enrichment factor was calculated according to

$$\text{Enrichment Factor (E.F.)} = \frac{[X_{\text{cation}} / X_{\text{oxygen}}]_{\text{post HT}}}{[X_{\text{cation}} / X_{\text{oxygen}}]_{\text{pre HT}}} \quad (6-2)$$

6.3. Results and Discussion

6.3.1 XRD

Figure 6-2 shows the XRD patterns of the sintered pellets. LSCF, SCF, LBCF, LSM are identified in the pure perovskite phase¹⁰² while small quantities of secondary phases were detected in solid state synthesized LCCF.

6.3.2 Cr Vapor Deposition on LSCF

In Figure 6-3 are representative SEM micrographs of LSCF surfaces before and after heat treatment at 800°C for 50 hours in the presence of Crofer22APU. Compared

to the flat surface of non-heat treated samples in Figure 6-3a, all the surfaces showed the formation of a few micron sizes of particles after heat treatment. Heat treatment with direct contact to Crofer22APU sheet (Figure 6-3b) resulted in uniform formation of secondary phases on grain boundary and grain surfaces while the particles were formed along the grain boundary when LSCF surface was not in contact with the sheet (Figure 6-3c and 6-3d). The distances between Crofer22APU and leading edge of LSCF were 0.1 cm and 0.5 cm in Figure 6-3c and 6-3d, respectively. As the distance increased, apparently the formation of secondary phases decreased due to reduced mass transport of Cr vapor species to LSCF. Elemental atomic percents for a newly formed particle and a flat region between the particles after heat treatment were obtained using energy dispersive spectroscopy (EDS). As Table 6-3 shows, the flat region did not present noticeable difference in atomic percents compared to the non-heat treated sample. By contrast, the particle exhibited substantially increased concentration of Sr and Cr, indicating that the particles are Sr-Cr-O_x.

Compositional variation of surface layers as a result of the formation of Sr-Cr-O_x was investigated using Auger electron spectroscopy (AES). The flat region between Sr-Cr-O_x particles in Figure 6-3d was selected for the analysis, and the values were compared to non-heat treated sample. The elemental atomic percent obtained by AES is given in Table 6-4. It shows that atomic percent of cations varied after heat treatment while that of oxygen remained essentially constant.

The enrichment factors were calculated using Eq. 6-2. While La concentration was slightly increased, the concentration of the rest of the cations became halved. In our previous study, Sr enrichment after heat treatment was evident on the surface of Cr

contamination free LSCF.¹⁰³ Notably, the formation of submicron sized Sr-O precipitate on the grain surface was clearly visualized. For comparison, the elemental atomic percents and enrichment factor of the LSCF surface, which was heat treated at 800°C in the absence of Crofer22APU, were added in Table 6-4. Sr concentration became doubled while transition metal concentration decreased after heat treatment. Such Sr enrichment phenomena on LSCF were also reported by Bucher et al.⁵⁹ and Heide et al.⁶⁰ In Table 6-4, the major difference between the two samples, which were heat treated in the presence and absence of Crofer22APU, arises from the A site cation while the B site transition metals show similar trends. This implies that Sr-O precipitates on LSCF surfaces act as nucleation agents for the formation of Sr-Cr-O_x particles.¹⁰⁴ As a Sr-O precipitate is formed on grain surfaces while Sr-Cr-O_x particle is preferentially formed along the grain boundaries, it is likely that Sr-O on grain surfaces diffuse to grain boundary regions. As a consequence, the grain surface of LSCF exhibited a Sr deficiency.

Figure 6-4 shows the XRD patterns of pre- and post-heat treated LSCF in the presence of Crofer22APU. A single phase rhombohedral perovskite structure was confirmed for the pre-heat treated sample.¹⁰⁵ After heat treatment, no obvious change was found in the standard normal XRD pattern. But low angle XRD, which provides intensified peaks from the surface region, identified the formation of SrCrO₄. The change is pronounced only in low angle XRD because the structural variation occurs in the near-surface region. In addition to the formation of SrCrO₄, low angle XRD revealed the formation of Fe₂O₃ and the combination of split characteristic peaks of rhombohedral into a single peak (Figure 6-4b~d). Similar structural changes of LSCF was observed by

Waller et al.¹⁰⁶ They tested the effect of Sr deficiency on the structural change of LSCF and found the combination of split characteristic peaks of the rhombohedral phase. They suggested that this is evidence of a phase transition from rhombohedral to cubic structure. In their study, Fe_2O_3 appeared as Sr deficiency increased, which was also observed in this study. Therefore, the structural analysis in this study indicates that the LSCF surface undergoes a phase transition under Cr contamination conditions as a result of a Sr deficiency. This is in good agreement with the chemical analysis performed in this study.

For ABO_3 perovskite materials, it is generally believed that B site transition metals play a critical role for catalytic activity.^{24, 69, 87, 88} Kilner et al.³¹ investigated the dependence of surface exchange coefficients (K_o) on the composition of $\text{La}_{0.8}\text{Sr}_{0.2}\text{Mn}_{1-y}\text{Co}_y\text{O}_3$ and found that K_o increased with increasing Co concentration. Takeda et al.⁴⁴ measured the cathodic polarization of $\text{La}_{0.7}\text{Sr}_{0.3}\text{MO}_3$ (M=Cr, Mn, Fe, Co) and found that $\text{La}_{0.7}\text{Sr}_{0.3}\text{CoO}_3$ exhibited the lowest polarization at 800 °C in air. In addition, Kan et al.⁵⁴ studied the effect of catalyst impregnation on the catalytic activity for oxygen exchange. They found oxygen exchange reaction of $\text{La}_{0.8}\text{Sr}_{0.2}\text{MnO}_3$ (LSM) was improved with the addition of Co on the surfaces via wet impregnation. These results in literatures indicate that Co is a catalytically active element for oxygen reduction reaction. Therefore, reduction in Co concentration on the surface of LSCF is likely to degrade oxygen exchange reaction. Furthermore, the collected data of the surface exchange coefficients and the oxygen tracer diffusion coefficients of various metal oxides evidences that the electronic species on the surface are essential for oxygen exchange reaction. The formation of near insulator Fe_2O_3 ,¹⁰⁷ and less conductive Sr deficient LSCF,¹⁰⁸ reduces

the concentration of electronic species and so contributes to degradation of oxygen exchange reaction at the surface. Consequently, the formation of Sr and transition metal deficient layers on LSCF surfaces as a result of the formation of SrCrO_4 particle is likely to cause a significant degradation in oxygen reduction reaction. In our group, the impact of Cr contamination on the oxygen reduction reaction of LSCF was examined using electrical conductivity relaxation (ECR), AC impedance, and temperature programmed isotopic exchange.¹⁰⁹ They consistently showed degradation of oxygen exchange reaction at the surface as a result of Cr vapor deposition. The same chemical variation of LSCF surface as observed in this study was found after ECR test at 800 °C. The result confirms that the formation of Sr and transition metal deficient phases reduces the catalytic activity for oxygen reduction.

6.3.3 Dependence of A-site ions on Cr Vapor Deposition

LCCF, LSCF, LBCF, and SCF, which have different A site but identical B site ions, were heat treated at 800°C for 50 hours in the presence of Crofer22APU. Figure 6-5 shows representative surfaces of these samples after heat treatment. All samples present significant morphological changes after heat treatment. The formation of secondary phase decreased as the separation distance increased due to reduced mass transport of Cr vapor species. Table 6-5 shows the elemental atomic percents of newly formed particles obtained using EDS. The concentration of alkaline earth metal ions was substantially higher than the other cations compared to non-heat treated samples, and considerable amounts of Cr were found. This result provides that the secondary phases are Ca-Cr-O_x , Ba-Cr-O_x , and Sr-Cr-O_x for LCCF, LBCF, and SCF respectively, in which alkaline earth metal oxides worked as a nucleation agent. It is likely that Cr vapor

deposition on these materials is governed by the same Cr vapor deposition mechanism as for LSCF.

Figure 6-6 shows the influence of temperature. Compared to heat treated surfaces at 800°C, these surfaces exhibit reduced formation of secondary phases when heat treated at 600°C. When heat treatment was conducted at 400°C, a dramatic drop in Cr vapor deposition on metal oxides was observed. Since Cr vapor pressures increase with increasing temperatures, this is primarily due to the reduced Cr vapor pressure at lower temperatures.

The effect of A site cations on the reactivity to Cr vapor species was examined by comparing the amount of secondary phases. Previously, Yokokawa et al.¹¹⁰ provided the formation enthalpy difference between metal chromates and metal oxides. They showed a strong tendency of basic oxides to form stable metal chromates, in which BaO has a stronger tendency than SrO, which has a stronger tendency than CaO. This indicates that the tendency to form a metal chromate increases with increasing basicity of metal oxides. LBCF shows higher areal density of secondary phase than LSCF at 800°C (Figure 6-5) and 600°C (Figure 6-6). However, it is difficult to tell whether LSCF is more reactive than LCCF based on the formation of secondary phase. At 800°C, LCCF exhibited fewer particles with higher growth rate while at 600°C showed similar areal density of particles after heat treatment.

In addition, it appears that the reactivity increases with increasing molar concentration of alkaline earth metal ions. In Figure 6-5 and Figure 6-6, SCF presents a substantially higher amount of secondary phase compared to LCCF, LSCF and LBCF. In part, this can be explained by increased amount of Sr, which has a higher basicity

than La. However higher reactivity of SCF is also attributed to higher concentration of unstable transition metal species. This will be explained in following section.

6.3.4 Dependence of B-site ions on Cr Vapor Deposition

The effect of B site transition metals on the reactivity to Cr vapor was investigated by comparing Cr vapor deposition behavior on LSCF and LSM. They have the same A site composition but different B site transition metals. LSM was placed on the Crofer22APU sheet and heat treated 800°C for 50 hours. Figure 6-7a and 6-7b show the surfaces of non-heat treated and post-heat treated LSM, respectively. After heat treatment, any noticeable change, e.g. the formation of particles, was not found on the LSM surface. This indicates that LSM does not react with Cr vapor species at 800°C.

The formation of secondary phase was observed when LSM was heat treated at higher temperatures. Figure 6-8a shows the SEM micrograph of LSM after heat treatment at 1050°C for 50 hours. It shows the formation of faceted particles on the surface. EDS spectra for non-heat treated LSM and faceted particles are given in Figure 6-8b and 6-8c, respectively. It reveals that the secondary phase is a Cr-Mn-O_x. Multiple particles were analyzed but the formation of Sr-Cr-O_x was not found on LSM. The temperature dependence of Cr vapor deposition on LSM is in good agreement with the literature. Tucker et al.¹¹¹ tested Cr vapor deposition on La_{0.65}Sr_{0.3}MnO₃ and found that Cr vapor deposition did not occur until 1000°C. The observation of Cr vapor deposition on LSM without application of cathodic or anodic polarization supports the theory that the nature of Cr vapor deposition on LSM at 1050°C is a chemical process, in which Mn acts as a nucleation agent.

It was previously reported that the crystal structure of Cr-Mn-O_x, which was formed as a result of Cr vapor deposition on LSM, was (CrMn)₃O₄.^{14, 126} The most prominent

form of $(\text{CrMn})_3\text{O}_4$ is cubic MnCr_2O_4 spinel in which Mn^{2+} and Cr^{3+} occupy the tetrahedral and octahedral sites, respectively.^{112, 113} Consequently, it is likely that Mn^{2+} acts as a nucleation agent for the formation of $(\text{CrMn})_3\text{O}_4$ as proposed by Jiang et al.¹¹⁴ In order to form Mn^{2+} species, LSM needs to undergo charge disproportionation of Mn^{3+} according to¹¹⁵



Since the formation of $(\text{CrMn})_3\text{O}_4$ does not occur until 1050°C, charge disproportionation of Mn^{3+} is likely to be inhibited below this temperature.

Note that the formation of SrCrO_4 on LSCF was found at 600 and 800°C, in which Sr acted as a nucleation agent. Also, other perovskite materials containing Co and Fe in B site exhibited similar Cr vapor deposition behavior. By contrast, no formation of SrCrO_4 was detected on LSM at 800°C, and Cr vapor deposition occurred at much higher temperatures. Since the chemical composition of A site concentration is the same between LSCF and LSM, the significant difference in Cr vapor deposition behavior is attributed to B site transition metals. While LSCF exhibits a substantial oxygen deficiency in air,^{40, 49} LSM shows oxygen excess. Such high oxygen vacancy concentration in LSCF is due to the instability of Co^{4+} and Fe^{4+} , which are generated by a partial substitution of La for Sr. They are unstable species at high temperatures⁸ and thus, LSCF achieves a more stable state by reducing them through oxygen vacancy formation. In contrast, the valence stability of Mn^{4+} is relatively higher than that of Mn^{3+} ,^{116, 117} and therefore, LSM does not exhibit oxygen deficiency. Even though oxygen vacancies improve the oxygen reduction reaction on the surface and oxygen diffusion in the lattice,²³ their presence weakens the stability of the structure by

removing the shielding effect between like atoms. Previously Wang et al.⁶⁷ demonstrated the effect of oxygen vacancies on bonding strength experimentally. They found that the elastic modulus of ceria decreases drastically as the oxygen vacancy concentration increases. This proves that the bonding strength becomes weakened in accordance with the formation of oxygen vacancies. At elevated temperatures, LSCF has substantial oxygen vacancies in the lattice⁴⁵ and thus Sr is likely to be loosely bound in the lattice. Then enriched Sr in surface region can be precipitated into Sr-O and react to Cr vapor deposition. In contrast, Sr in LSM, which is not oxygen deficient in air, is tightly-bound in the lattice and so inert in Cr contaminated environments.

In the previous section, SCF exhibited substantially higher Cr vapor deposition than LCCF, LSCF, and LBCF. The difference between SCF and other materials is the concentration of alkaline earth metal ions in A site. As explained, increase in alkaline earth metal ions increases the basicity of A site. But it also raises the concentration of unstable Co^{4+} and Fe^{4+} species. As a result, SCF has more oxygen vacancies in the lattice and becomes more reactive to Cr vapor species.

Matsuzaki et al.¹¹⁸ compared Cr vapor deposition behaviors of LSCF and LSM cathode based cells. They found that Cr vapor deposition occurred on the electrode surface of LSCF during the cell test at 800 °C. Cr contamination was intense on electrode surface near the interconnect while it decreased at the three phase boundary (TPB) of air, electrode and electrolyte. In contrast, in the case of LSM cathode based cell, Cr vapor deposition was found in TPB region while it was significantly reduced on the electrode surface. Such different Cr contamination behaviors indicate that the nature of Cr vapor deposition process on LSCF and LSM during cell operation is not identical.

Cr vapor deposition on electrodes can occur either by chemical or electrochemical reaction. This study shows that Cr vapor species deposited on LSCF at 800 °C in the absence of polarization currents, which is an evidence of chemical reaction. It was found that Cr vapor deposition via chemical reaction decreased with increasing separation distance between metallic interconnect and electrode surface due to the reduced mass transport of Cr vapor species. This well justifies the observed Cr vapor deposition on LSCF in literature. Thus, it is likely that Cr vapor deposition on LSCF electrode during the cell test is chemical reaction. In contrast, this study shows no Cr vapor deposition on LSM at 800 °C in the absence of polarization currents. This indicated that Cr vapor deposition on TPB of LSM during the cell test at 800 °C is not chemical reaction. Previously, Ricoult¹¹⁹ found that cathodic polarization during the single cell operation caused strong enrichment of Mn²⁺ at the TPB of LSM and YSZ at 700 °C. As mentioned, Mn²⁺ is likely to act as a nucleation agent for the formation of (CrMn)₃O₄ particles. Consequently, the formation of Mn²⁺ due to cathodic polarization leads to preferential deposition of Cr vapor species along the TPB region during the cell operation. This is in agreement with the observation in literature. Therefore, the dominant reaction process of Cr vapor deposition on LSM at 800 °C is likely to be the electrochemical reaction.

At last, it was observed that the grain surface of LSCF exhibited a Sr deficiency in Cr contaminated environment because enriched Sr on LSCF diffused from grain to grain boundary regions, forming SrCrO₄. Two possible diffusion mechanisms are surface diffusion and evaporation-condensation. Recently Bishop et al.¹²⁰ reported mass loss of La_{0.6}Sr_{0.4}Co_{0.2}Fe_{0.8}O_{3-δ} at 800 °C in air using thermogravimetry. Mass reduction

continued over 200 hrs, which is a substantially longer time scale compared with oxygen diffusion and surface reaction. Such a mass loss phenomenon was difficult to be justified by Sr enrichment to surface regions or the formation of Ruddlesden-Popper (RP) phases, which were frequently found from other perovskite materials.^{68, 71} One can deduce that Sr-O on LSCF is vaporized at oxidizing conditions at 800 °C. This result puts more weight on evaporation-condensation for the diffusion mechanism of Sr-O on LSCF surface.

6.4. Conclusions

This study improves the fundamental understanding of the reaction between SOFC cathode materials and Cr vapor species. It turns out Cr vapor deposition causes substantial chemical and structural changes of LSCF surface layers above 600°C, which involves the formation of SrCrO₄ particles, and Sr and transition metal deficient matrices. This may lead to a significant degradation in surface catalytic activity of LSCF. LCCF, LBCF, and SCF exhibited similar Cr vapor deposition behavior, in which alkaline earth metal ions in the A site acted as nucleation agents. In contrast, LSM presented considerably different behavior in Cr vapor deposition. Mn²⁺, which is formed as a result of charge disproportionation of Mn³⁺, seems to act as a nucleation agent on LSM. Consequently, chemical reaction between LSM and Cr vapor species occurred at higher temperatures (1050°C). The results imply that transition metals in the B site, rather than the basicity of A site ions, primarily determines the reactivity to Cr vapor species. It is proposed oxygen vacancy formation due to instability of Co⁴⁺ and Fe⁴⁺ increases the repulsive forces between cations, and allows the formation of nucleation agent at lower temperatures. Therefore below 1000°C the dominant Cr vapor deposition mechanism

on LSCF and LSM during the cell operation is likely to be chemical and electrochemical reactions, respectively.

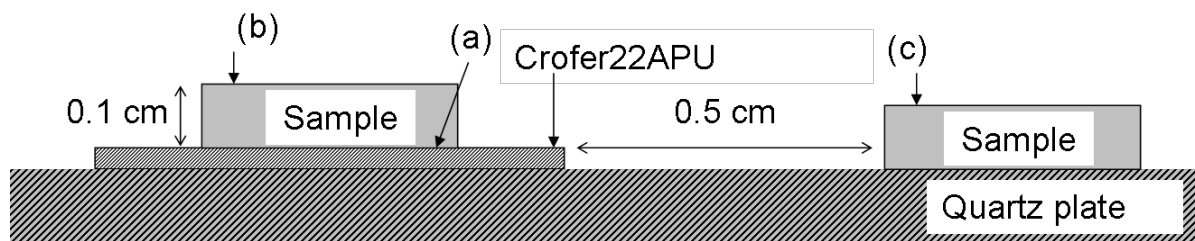


Figure 6-1. Schematic of experimental design for heat treatment.

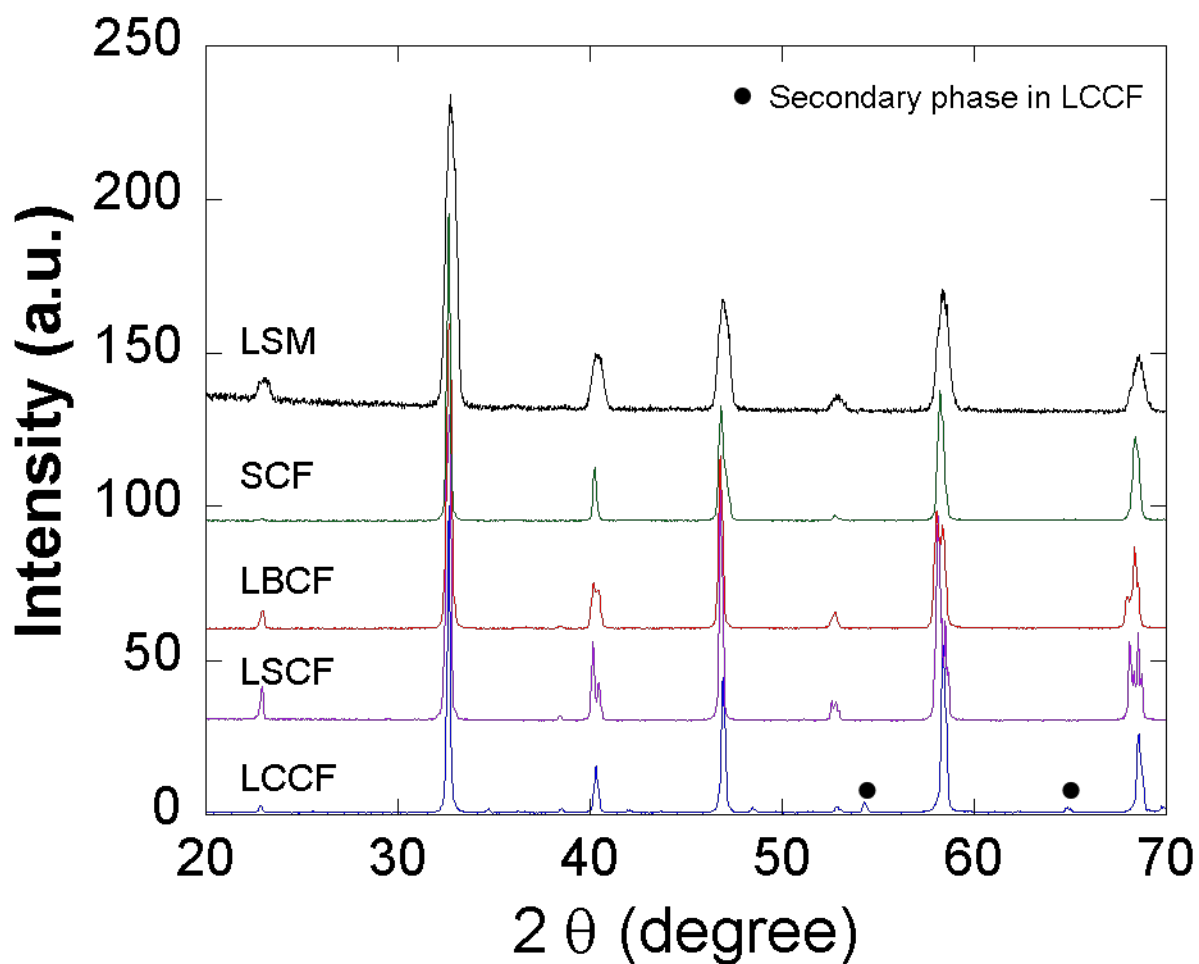


Figure 6-2. XRD patterns of tested perovskite materials

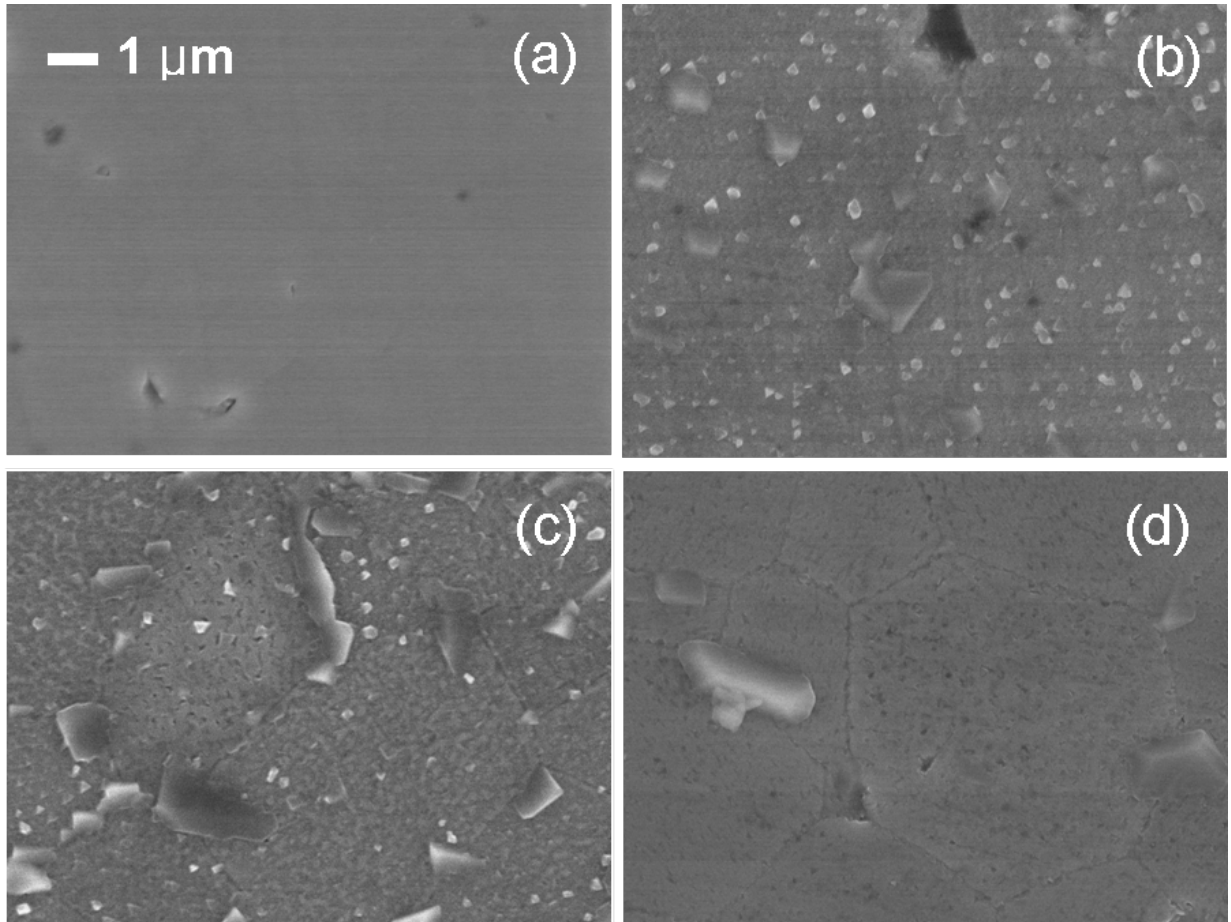


Figure 6-3. Surfaces of LSCF (a) before and (b-d) after heat treatment in the presence of Crofer22APU at 800°C 50 hrs. The leading edge distances between LSCF and Crofer22APU sheets were (b) direct contact, (c) 0.1 cm, and (d) 0.5 cm. All images are the same scale.

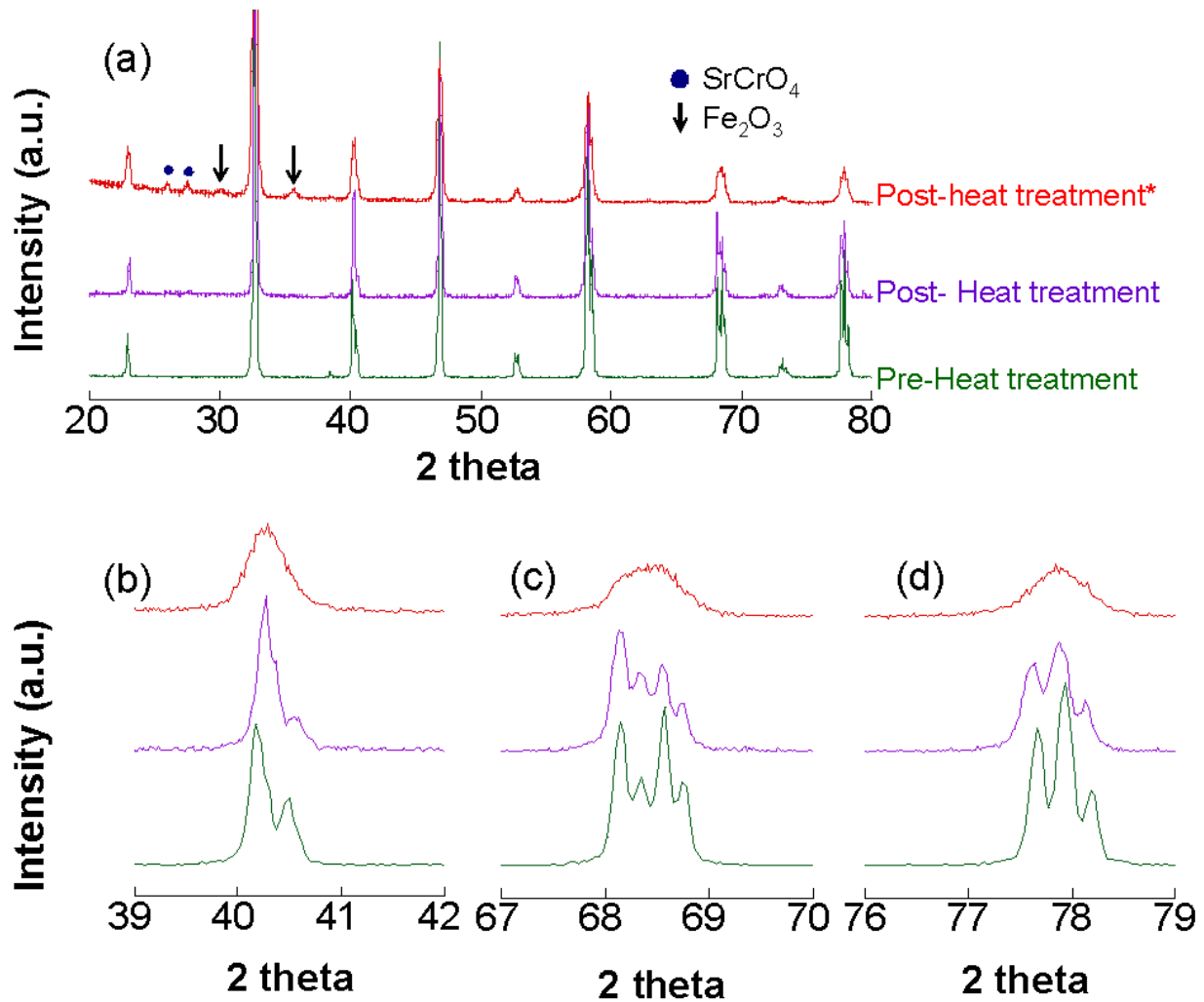


Figure 6-4. (a) XRD patterns of fresh and heat treated LSCF on Crofer22APU sheet at 800°C for 50hours. (b ~ d) Enlarged patterns for better comparison. * is the XRD pattern measured using a low angle mode.

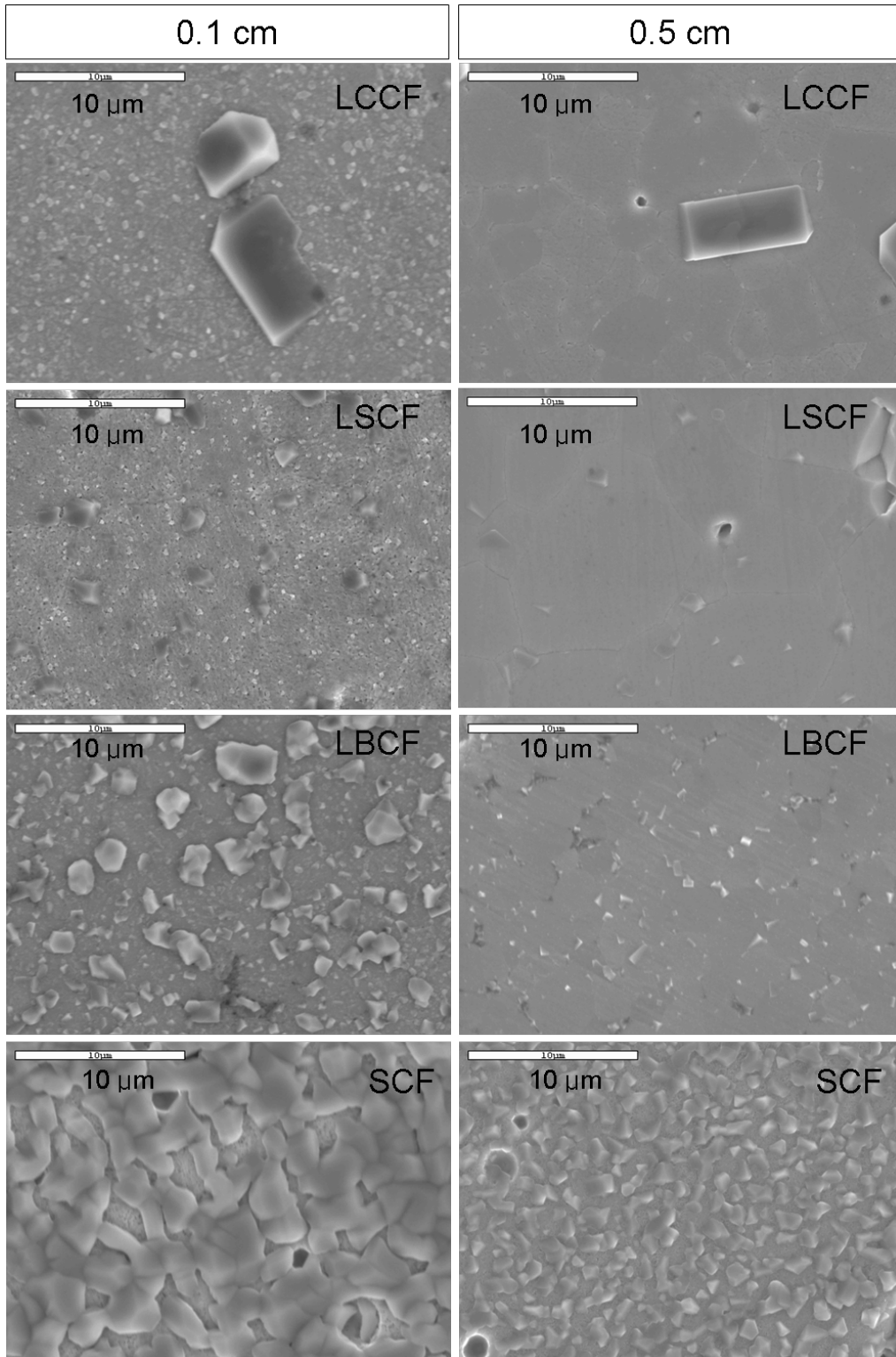


Figure 6-5. Surfaces of LCCF, LBCF, LSCF and SCF after heat treatment in the presence of Crofer22APU at 800°C for 50 hours. The leading edge distances between samples and Crofer22APU sheet were 0.1 cm and 0.5 cm for the left and right hand sides, respectively.

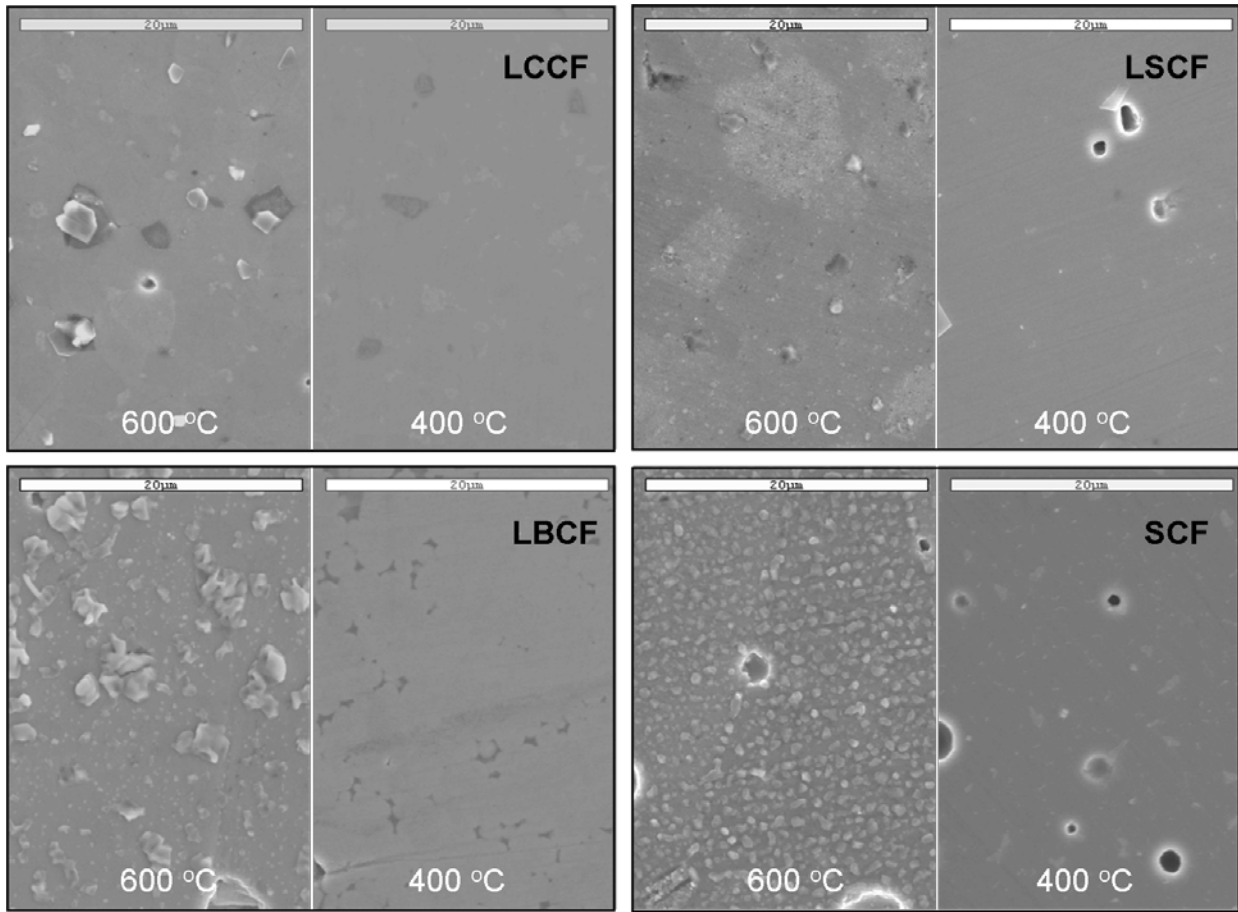


Figure 6-6. Surfaces of tested after heat treatment in the presence of Crofer22APU at 600°C and 400°C (Leading edge distance 0.1 cm).

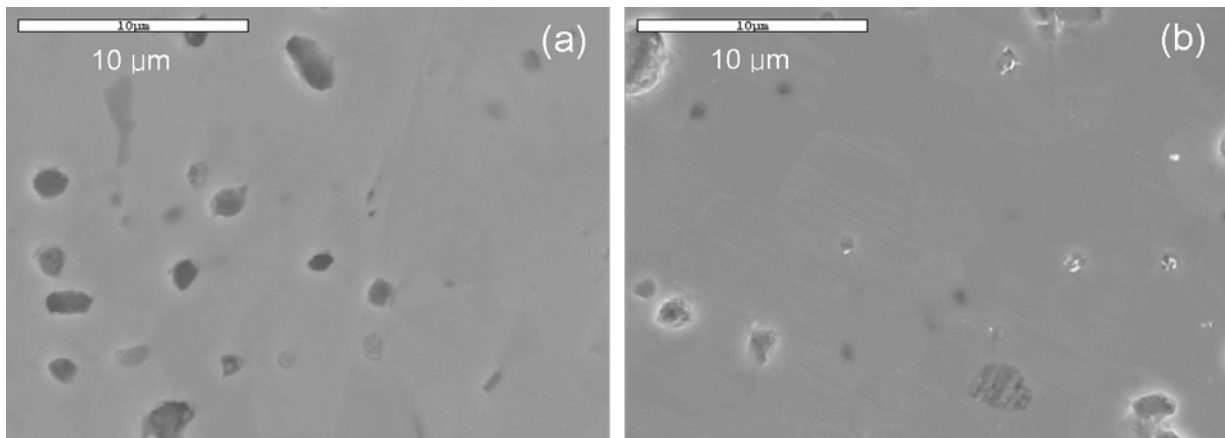


Figure 6-7. SEM micrographs of LSM surfaces of (a) before and (b) after heat treatment at 800°C for 50 hours in the presence of Crofer22APU (Leading edge distance 0.1 cm).

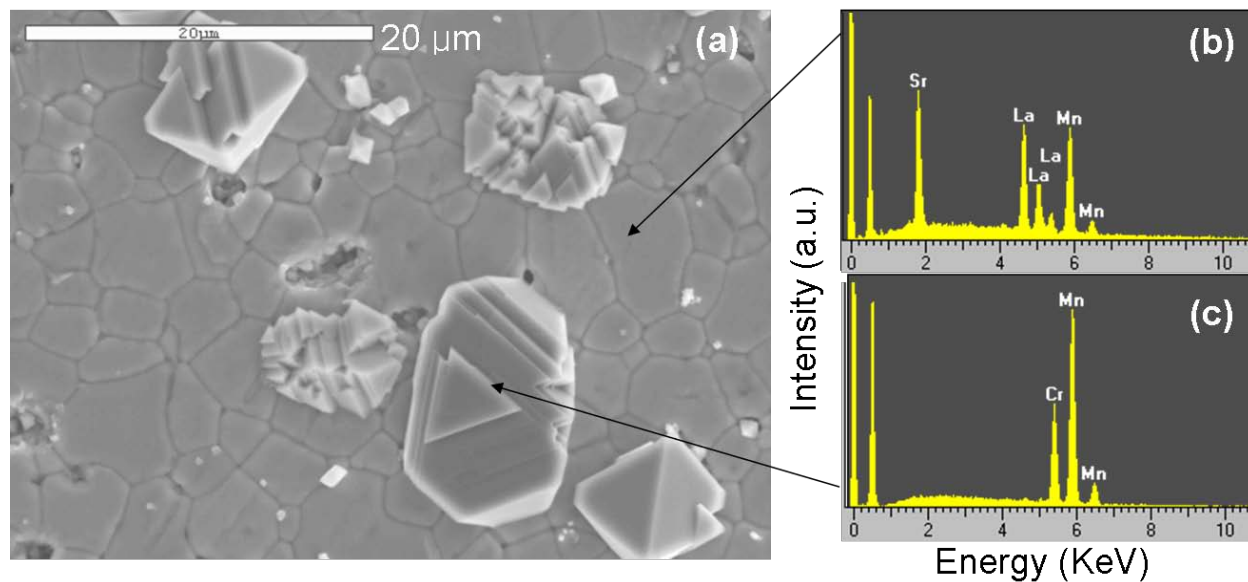


Figure 6-8. (a) SEM micrograph of LSM after heat treatment in the presence of Crofer22APU at 1050°C for 50 hours, and EDS spectra for (b) the flat region and (c) particle (Leading edge distance 0.1 cm).

Table 6-1. Summary of tested ABO₃ perovskite materials

Composition	Abbreviation	Preparation method
La _{0.6} Ca _{0.4} Co _{0.2} Fe _{0.8} O ₃	LCCF	Solid State synthesis
La _{0.6} Sr _{0.4} Co _{0.2} Fe _{0.8} O ₃	LSCF	Praxair specialty
La _{0.6} Ba _{0.4} Co _{0.2} Fe _{0.8} O ₃	LBCF	Solid State synthesis
SrCo _{0.2} Fe _{0.8} O ₃	SCF	Solid State synthesis
La _{0.6} Sr _{0.4} MnO ₃	LSM	Solid State synthesis

Table 6-2. Chemical composition of Crofer22APU

Cr	Fe	Mn	Si	Cu	La
20~24	Bal.	0.3~0.8	0.5	0.5	0.04~0.2

Table 6-3. Elemental atomic percents (%) of LSCF after heat treatment at 800°C for 50 hrs in the presence of Crofer22APU obtained using EDS

		La	Sr	Co	Fe	O	Cr
Non-heat treated		12	9	4	14	61	
Post-heat treatment	Flat surface	17	8	4	20	51	
	Particles	5	16	1	5	58	15

Table 6-4. AES atomic percents of LSCF after heat treatment(HT) at 800°C for 50 hours

	La	Sr	Co	Fe	O
Non-heat treated	30	12	5	11	42
HT in the presence of Crofer22APU*	38 (1.2)	8 (0.6)	2 (0.4)	8 (0.7)	44
HT in the absence of Crofer22APU	28 (0.9)	22 (1.8)	0 (0)	7 (0.6)	43

The enrichment factors are given in parenthesis.

* A flat surface region was selected for the analysis.

Table 6-5. Elemental atomic percents of non-heat treated and heat treated samples*

LCCF	La	Ca	Co	Fe	Cr
Non-heat treated	12	8	4	16	
Post heat treatment	1	18	1	2	19
LBCF	La	Ba	Co	Fe	Cr
Non-heat treated	17	11	4	21	
Post heat treatment	1	16	1	4	14
SCF		Sr	Co	Fe	Cr
Non-heat treated		27	6	25	
Post heat treatment		21	3	12	12

*The newly formed particles after heat treatment were selected for the analysis.

CHAPTER 7 DEGRADATION MECHANISM AND THEIR IMPACT ON OXYGEN REDUCTION KINETICS OF LSCF

7.1. Introduction

The advantages of using Fe-Cr metal alloys as interconnects for solid oxide fuel cell (SOFC) stacks include reduction in manufacturing costs, good machinability and enhanced thermo-mechanical stability.^{109, 110} However, Cr vapor species generated from the Cr scales of these alloys are known to react with the cathode, forming a less catalytically active phase.^{40, 104, 121} The long-term stability is an important requirement for the commercialization of SOFCs. Thus, there is a need to understand cathode performance in Cr contaminated environments over long time periods. In this study, the influence of Cr contamination on the oxygen reduction reaction of $\text{La}_{0.6}\text{Sr}_{0.4}\text{Co}_{0.2}\text{Fe}_{0.8}\text{O}_3$ (LSCF) was examined using electrical conductivity relaxation (ECR),^{48, 49, 52} AC impedance spectroscopy^{23, 80, 91} and temperature programmed isotopic exchange (TPX).^{54, 122} The impact of Cr vapor deposition on surface morphology and composition of LSCF was clearly identified from post ECR characterization.

7.2. Experimental.

7.2.1 AC Impedance

A symmetric cell, which consists of LSCF/GDC/LSCF, was prepared for the impedance measurement. A dense $\text{Gd}_{0.1}\text{Ce}_{0.9}\text{O}_{2-\delta}$ (GDC, Anan Kasei, Japan) electrolyte was made by sintering a pressed pellet at 1450 °C for 4 hours. A LSCF ink was prepared by mixing LSCF powder with texanol based polymer vehicle (ESL electro-science, USA) using Thinky mixer (Thinky, Japan). The ink was symmetrically painted on both sides of the electrolyte, each having a same electrode area of 0.28 cm². Pt wires were connected as a current collector and LSCF ink was applied for better

contact. After that, the cell was sintered at 1100 °C for 1 hour with heating and cooling rate of 5 °C/ mins.

AC impedance of the symmetric cells was measured at 800 °C in the presence and absence of K-type thermocouple using a Solartron SI 1260 frequency response analyzer. The amplitude of the excitation voltage was 50 mV and the AC frequency range was from 0.1 to 10⁵ Hz. Measurement was repeated every 1 hour using ZPlot software (Scribner). The experimental data was fit using the equivalent circuit shown in Figure 1 using ZView software (Scribner) in order to de-convolute the impedance response and extract the electrode resistance. It consists of a series of resistors (R) and constant phase elements (CPE). In the figure, R_E is the electrolyte ohmic resistance, and R_{HF} and R_{LF} refer to high and low frequency resistance respectively. The electrode area specific resistance (ASR_p) is obtained by

$$ASR_p = \frac{(R_{HF} + R_{LF}) \cdot Area_{Electrode}}{2} \quad (7-1)$$

7.2.2 Electrical Conductivity Relaxation

A dense LSCF sample was prepared for analysis. It was prepared by pressing La_{0.6}Sr_{0.4}Co_{0.2}Fe_{0.8}O_{3-δ} powder (Praxair Specialty Ceramics, USA) uni-axially and sintering a pellet at 1400°C for 4 hours in air. The density of the sintered body measured by the Archimedes method was ~ 97% of the theoretical value (6.36g/cm³). The sintered body was cut and then polished with a series of SiC papers and diamond abrasives (Leco) down to 1µm. . After polishing, samples were cleaned with DI water and acetone before ECR measurement. The sample dimension was approximately 0.1x2x20 mm³.

A bar of LSCF was positioned on the alumina tube in the middle of the reactor and a K-type thermocouple (OMEGA, Part# KMQSS-040E-12) was placed below the sample for accurate measurement of temperature. A N₂ and O₂ gas mixture was fed into the reactor through a mass flow controller (MKS & Edwards) and the total flow rate was fixed at 300sccm. The electrical conductivity was measured via the four point probe method using a Lock-in amplifier (Stanford, SR830) automated with Labview software. The sample was heated to 800°C at a rate of 5°C/min in air. Before the ECR measurement, the feed stream was switched to 3% O₂. Once it reached steady state, the feed stream was switched via four way switching valve. The oxygen partial pressure (pO₂) step was programmed to increase by the following steps:

3→5→8→12→18→28→43→67%.

7.2.3 Temperature Programmed Isotopic Exchange (TPX)

A schematic of the TPX test system is seen in Figure 7-2a. The custom-made quartz reactor (i.d. = 4 mm) was used and a powder sample was placed atop the quartz frit in the middle of the reactor. The flow rate of the feed gas was controlled by mass flow controllers (MKS & Alicat) with a total flow rate of 25sccm. The reactor effluent was sampled by a quadrupole mass spectrometer (MS, Extrel QMS), in which Masses 16 (¹⁶O), 18 (¹⁸O), 28 (N₂), 32 (¹⁶O₂), 34 (¹⁶O¹⁸O), 36 (¹⁸O₂) and 40 (Ar, inert tracer) were continuously monitored. The K type thermocouple, which was shielded in a quartz capillary tube, was placed above the sample to monitor temperatures.

The heating schedule and condition are briefly summarized in Figure 7-2b. Before a TPX run began, the sample was pre-heat treated at 650°C in 1% ¹⁶O₂ for 10 mins and cooled down to room temperature. Once the MS signal reached a steady state, the feed

gas was switched to 0.25% $^{18}\text{O}_2$ (Cambridge Isotope, 95% pure), followed by sample heating at a linear rate of 30°C/min. All gas mixtures were balanced by helium.

7.2.4 Characterization

The microstructure and element distribution before and after ECR measurement was characterized by scanning electron microscopy (SEM, JEOL JSM6400), combined with energy dispersive spectroscopy (EDS, Oxford, UK). ZAF correction was used for semi-quantitative analysis for EDS. In addition, surface chemical composition of LSCF before and after ECR test was measured using Auger electron spectroscopy (AES, AES Perkin-Elmer PHI 660). The accelerating voltage was 10 kV and it scanned the energy ranges between 50 to 2050 eV, which covered the characteristic peaks of La_{MNN} (625 eV), Sr_{LMM} (1649 eV), Co (775 eV), Fe_{LMM} (703 eV), and O_{KLL} (510 eV). These characteristic peaks were selected in order to minimize interference with each other. Obtained AES spectra were differentiated, and elemental atomic percents were calculated using AugerScan 3.2.0 software (RBD Instrument). The specific surface area of powders was measured by BET analysis (Quantachrome NOVA 1200).

7.3 Results and Discussion

7.3.1 AC Impedance

Figure 7-3 shows the impedance spectra of a LSCF/GDC/LSCF symmetric cell at 800°C. There are approximately two semi-circles, which consists of high frequency (HF) and low frequency (LF) components as seen in the figure. As the measurement was conducted at 800°C, the size of semi-circles changed with aging. For easier comparison, the HF intercepts of the semi-circles were subtracted in Figure 7-3. After 190 hours, the size of the HF semi-circle was found to increase, while that of the LF semi-circle remained roughly constant. HF and LF components were de-convoluted by fitting the

equivalent circuit (Figure 7-1) to experimental data, and the related area specific resistance (ASR) was plotted as a function of aging time in Figure 7-4a. This shows that the electrode ASR, which is the sum of ASR_{HF} and ASR_{LF} , increased relatively faster for the first 50 hours due to the increase in ASR_{HF} . Then the degradation rate became slightly reduced, but the electrode ASR increased continuously. The overall electrode ASR increased approximately 57% after 190 hours. In contrast, if the K-type thermocouple inside the reactor was removed during impedance measurement, the symmetric cell exhibited roughly constant ASR_{HF} and ASR_{LF} for 190 hours at 800°C as shown in Figure 4b. Since the temperatures were maintained by the same furnace temperature controller, which was located outside of the quartz reactor, the temperatures were essentially the same in both cases. The temperature differences between inside and outside of the reactor were less than ± 5 °C.

Each semi-circle corresponds to different reaction mechanisms. Previously Esquirol et al.⁹¹ and Sahibzada et al.⁸⁰ measured the impedance of LSCF/GDC/LSCF symmetric cell, and observed the formation of two semi-circles at 800 °C. They attributed the HF and LF components to the surface reaction and gas phase diffusion, respectively. In this study, the ASR_{HF} was found to increase while ASR_{LF} remained roughly constant at 800 °C when the symmetric cell was tested in the presence of K-type TC in the reactor. This indicates that resistance for surface reaction increased due to K-type TC.

7.3.2 Electrical Conductivity Relaxation

Figure 7-5a shows an electrical conductivity relaxation curve after switching the pO_2 from 43 to 67% at 800°C, which is normalized by initial and final equilibrium

electrical conductivities. It shows that the kinetic model fits well to experimental data. Figure 7-5b shows the variation of relaxation curves with aging when the pO₂ was switched from 43 to 67%. As the ECR run was repeated over time at isothermal condition, the relaxation time, which was required to reach a new equilibrium, gradually increased. This indicates degradation of oxygen transport on the surface or in the bulk..

Chemical diffusion (D_{chem}) and chemical exchange (K_{chem}) coefficients in the pO₂ range from 5 to 67% at 800°C were obtained by fitting kinetic model to relaxation curves. They were plotted in log scale as a function of aging time in Figure 7-6. It shows that the degradation rate of D_{chem} was not significant over the entire pO₂ range, while K_{chem} exhibited relatively fast reduction up to 400 hours. Note that K_{chem} in log scale linearly dropped. This means that the degradation rate of K_{chem} was relatively faster at the beginning and decreased at longer time. Since K_{chem} represents the apparent rate for oxygen exchange reaction at the surface, the results indicate degradation of surface layers during the measurement. Since K-type thermocouple (TC) was located under the LSCF bar, it is likely the source of the Cr contamination on LSCF surface. Post ECR characterization clearly showed how it degraded the surface morphology and composition.

The relationship between electrode ASR (ASR_p) and surface exchange coefficient (K_o) is ^{100, 102}

$$K_o = \frac{R \cdot T}{z^2 F^2 ASR_p C_o} \quad (7-2)$$

where R is the gas constant, T is the absolute temperature, F is faraday constant, n is the number of electron transferred during the reaction, and C_o is oxygen concentration. Furthermore, K_o can be converted into K_{Chem} by⁹⁴

$$K_{\text{chem}} = \Gamma \cdot K_o \quad (7-3)$$

where Γ is a thermodynamic factor ($\frac{1}{2} \frac{\partial \ln pO_2}{\partial \ln C_o}$). Thus, the decrease in K_{Chem} from

ECR is consistent with the increase in ASR_p from AC impedance under essentially identical conditions.

7.3.3 Temperature Programmed Isotopic Exchange

Figure 7-7 shows the TPX results of fresh LSCF samples. Each oxygen concentration, $C(^{16}O_2)$, $C(^{18}O_2)$ and $C(^{16}O^{18}O)$, was normalized by input oxygen concentration, $C(^{18}O_2)$. Bulk oxygen evolution was observed above 550°C. Previously Stevenson et al.⁴⁵ and Tai et al.³⁴ measured the oxygen nonstoichiometry of $La_{1-x}Sr_xCo_yFe_{1-y}O_3$ and showed that oxygen nonstoichiometry increased above 600°C for LSCF having same chemical composition to this study. The difference in temperatures between this study and previous works is attributed to sample condition. While TPX tested a powder sample, a dense sample was used in literature. A powder sample possesses substantially higher surface area than dense sample, and thus it can provide more surface sensitive behavior. Since the bonding strength of oxygen in near surface region is weaker than oxygen in the bulk due to broken bonding and more point defects,¹²⁰ it is likely that oxygen in near surface region evolves more rapidly at lower temperatures than oxygen in bulk.

Even though overall oxygen concentration does not change until 550°C, TPX reveals that the oxygen exchange reaction is activated at substantially lower temperatures, thereby concentration of $^{18}O_2$ decreases and that of $^{16}O_2$ increases. Since oxygen diffusivity in the lattice is insignificant around 300°C, the oxygen

exchange reaction mostly occurs on the surface or near the surface region. In Figure 7-7, TPX results of two samples are compared. They are exactly the same except for the sample weight. In the figure, the LSCF sample with a higher total surface area exhibits lower onset temperatures for oxygen exchange. This is because the total amount of oxygen exchanges per unit time is proportional to total surface area and oxygen exchange kinetics. Therefore, in order for direct comparison of oxygen exchange kinetics between different samples, the total surface area must be the same.

For the test of Cr contaminated sample, samples were prepared by annealing LSCF powder at 800°C for 400 hours with and without Crofer22APU present. The specific surface area of the powders is given in Table 7-1. Heat treated LSCF powders exhibited reduced specific surface area due to coarsening than fresh LSCF and so sample sizes were selected to provide the same total surface area. TPX results of these samples are given in Figure 7-8. While they showed identical temperature dependency for overall oxygen concentration changes, the oxygen exchange behavior was considerably changed. The onset temperature for the heat treated LSCF sample is higher than the fresh LSCF sample, and it further increases when heat treated in the presence of Crofer22APU. A higher onset temperature indicates decreased oxygen exchange reaction at the surface. Therefore, the TPX result implies that heat treating LSCF at 800°C degraded the surface reactivity and the extent of degradation is increased by Cr contamination. This result is in agreement with the results of ECR and AC impedance and further confirms that LSCF cathode degradation is due to decreased surface oxygen exchange kinetics.

It is reported that the chemical composition of the LSCF surface is different from that of bulk at high temperatures. Viitanen et al.⁶¹ observed the absence of Co and Fe in the outermost atomic layer from contamination-free LSCF after an oxygen permeation experiment at 900°C. Bucher et al.⁵⁹ found Sr enrichment on the surface after measuring chemical exchange coefficient of LSCF at 600-700°C. Furthermore, Furthermore, Oh et al.⁸⁴ showed that enriched Sr in LSCF precipitated into submicron sized Sr-O particles under an oxidizing condition in temperature range of 600-900°C. They also observed reduced concentration of transition metals on the surface in accordance with Sr-O precipitation at 800°C. Similarly, enrichment of A site cation is also found in other perovskite materials such as $\text{La}_{1-x}\text{Sr}_x\text{MnO}_3$,¹²³ BaTiO_3 ,⁷⁰ and SrTiO_3 ⁶⁴⁻⁶⁶ at elevated temperatures. As a result concentration of B site transition metals became reduced in the surface region. Rahmati et al.⁶⁴ observed the formation of Sr-O islands on the surface of SrTiO_3 . They found that the areal density of surface islands under re-oxidized conditions (1200°C for 30 hours) increased with increasing surface energies of underlying grains. This indicates that formation of Sr-O islands is due to the stabilization of surface. Szot. et al⁶⁸ investigated the chemical variations of several ABO_3 perovskite materials at elevated temperatures (500-1000°C) and consistently found formation of AO layers on the surface , which is known as Ruddlesden-Popper Phase (RP).⁷¹ They propose that the formation of RP phase is stable in oxidizing condition. When LSCF powder was heat treated at 800°C for 400 hours in the absence of Crofer22APU sheets, the surface is likely to have Sr enriched and transition metal deficient phase. Since B site transition metals play a critical role for catalytic activity of ABO_3 perovskite materials^{26, 66-68} and Sr-O is a electrically insulator⁷⁴,

such Sr enrichment and the formation of Sr-O precipitates on the surface degrades the surface catalytic activity. Thus, it is likely the cause for the increase in the onset temperature when LSCF is heat treated without Crofer22APU present. The reason for higher onset temperature in Cr contaminated LSCF will be explained in following section.

7.3.4 Post ECR Characterization

Figure 7-9a and 7-9b are SEM micrographs of LSCF before and after ECR test, respectively. While the surface before ECR testing is flat and unblemished, it becomes rugged and the formation of faceted particles is found along grain boundary surfaces after ECR testing. Elemental atomic percents for a newly formed particle on grain boundaries as well as grain surfaces between the particles were obtained using energy dispersive spectroscopy (EDS). As table 7-2 shows, the grain surface did not present noticeable difference in atomic percents compared to the fresh sample. By contrast, the particle exhibited substantially increased concentration of Sr and Cr, indicating that the particles are Sr-Cr-O. This is in good agreement with literatures.^{40, 104} Since K type thermocouple (OMEGA) uses 304 stainless steel, which contains around 8 wt% Cr, as a sheath,¹²⁴ it is likely that Cr vapor species is formed and deposits on the LSCF electrode during ECR measurement.

The kinetic measurements in this study consistently show the degradation of surface catalytic activities. Therefore, the compositional variation of surface layers was investigated using Auger electron spectroscopy (AES). The grain surface between Sr-Cr-O particles was selected for the analysis. The elemental atomic percent, which was obtained using Eq. 11, is given in Table 7-3.

$$X = \frac{I_a/S_a}{\sum I_m/S_m} \quad (7-4)$$

where I is the peak intensity and S is the relative elemental sensitivity factor for the Auger line used. Compared to the fresh sample, atomic percent of cations varied substantially after heat treatment. It shows Sr deficiency on LSCF surface rather than Sr enrichment. In addition, the transition metals concentrations became halved.

In literatures, Sr enrichment at elevated temperatures was evident on the surface of LSCF.^{59, 60} For the comparison, the elemental atomic percents of the LSCF surface, which was heat treated at 800°C in the absence of Cr contamination, were added in Table 7-3.¹⁰³ Sr concentration became doubled and transition metal concentration decreased after heat treatment in the absence of Cr contamination. In Table 7-3, the major difference between the two samples arises from A site cation while B site transition metals show same trends. This implies that Sr-O precipitate on LSCF surfaces acts as a nucleation agent for the formation of Sr-Cr-O particles. As Sr-Cr-O particle is preferentially formed along the grain boundaries, it is likely that Sr-O on grain surface diffuses to grain boundary region either by surface diffusion or by evaporation-condensation. As a consequence, grain surface of LSCF exhibits Sr deficiency as observed in this study.

The heterogeneous catalytic activity is primarily determined by interaction between surface and surrounding gases, and thus surface composition and structure is an important factor affecting the activity. Even though the rate determining step of oxygen reduction reaction is not well understood, it is no doubt that B site transition metals play a critical role for oxygen reduction reaction.^{26, 66-68} Previously De Souza et al.⁴² measured surface exchange coefficient of $\text{La}_{1-x}\text{Sr}_x\text{Mn}_{1-y}\text{Co}_y\text{O}_3$ and found that the activation energy of K_0 decreased with increasing Co concentration. And Teraoka et

al.³⁷ found that the rate of the oxygen permeation of $\text{La}_{1-x}\text{Sr}_x\text{Co}_y\text{Fe}_{1-y}\text{O}_3$ increased with increasing Co. Kremenec et al. reported the oxygen adsorption properties of LaMO_3 (M=Cr, Mn, Co, Fe, Ni) depended on the transition metals, in which Co and Mn exhibited the highest oxygen adsorption. . In addition, Kan et al.⁵⁴ studied the effect of catalyst impregnation on the catalytic activity for oxygen exchange. They found oxygen exchange reaction of $\text{La}_{0.8}\text{Sr}_{0.2}\text{MnO}_3$ (LSM) was improved with the addition of Co on the surfaces via wet impregnation. These results in literatures indicate that Co is a catalytically active element for oxygen reduction reaction. Therefore, the formation of Sr and transition metal deficient layers on the grain surface of LSCF can bring a significant degradation in oxygen reduction reaction and eventually cell performance. In the TPX result, a heat treated LSCF sample in the presence of Crofer22APU exhibited higher onset temperatures than heat treated LSCF in the absence of Crofer22APU. This indicates the formation of Sr and transition metal deficient surface more dramatically reduces the surface catalytic activity than Sr enriched surface.

It should be stressed that the Cr contamination source for ECR and AC impedance test was a K type TC, which contains Cr alloys as a sheath. In many studies, the TC is located near the sample in order for accurate measurement of temperatures. However, this may lead to unwanted Cr contamination on tested samples during the measurement. In order to prevent it, the TC must be shielded by other materials such as Zirconia or quartz.

7.4 Conclusions

This study improved degradation mechanism and their impact on the oxygen reduction reaction of LSCF. The temperature programmed isotopic exchange (TPX) result showed that heat treating LSCF at 800°C degraded the surface reactivity due to

Sr enrichment and the extent of degradation was further increased by Cr contamination. Electrical conductivity relaxation and AC impedance study consistently showed that oxygen reduction reaction at the surface was degraded as a result of Cr vapor deposition. Post ECR characterization revealed that Cr vapor deposition deteriorated surface properties by forming a catalytically inactive surface layer, which consists of Sr-Cr-O particles and Sr deficient surface layers. The surface of LSCF also exhibited reduced concentration of transition metals. It seems that enriched Sr on LSCF surface acts as a nucleation agent for the formation of Sr-Cr-O particles, and as a result LSCF surface exhibits Sr deficiency.

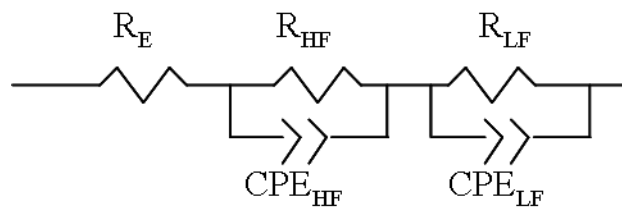


Figure 7-1. Equivalent circuit to fit the measured impedance data

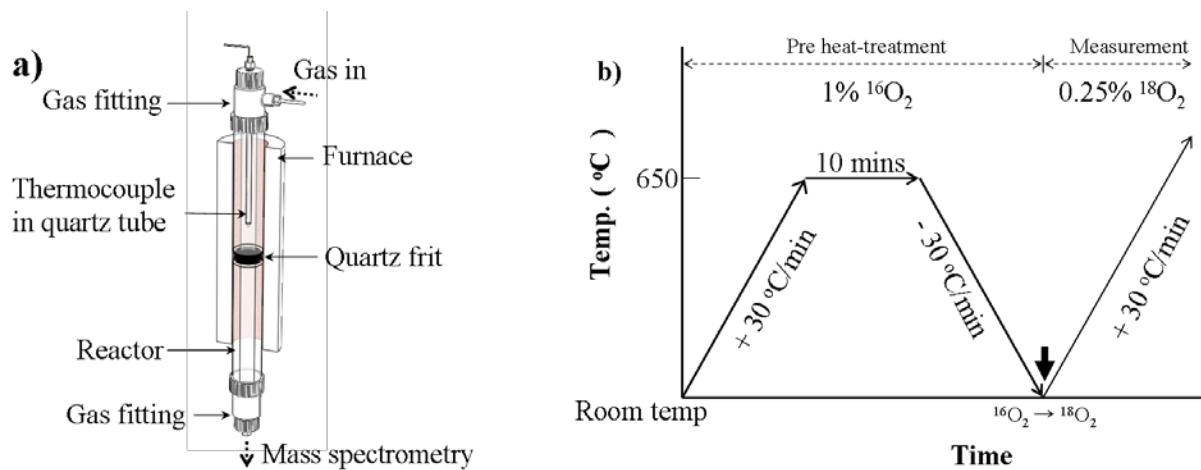


Figure 7-2. (a) A schematic of the experimental set up used for temperature programmed isotopic exchange and (b) the pre-heat treatment and measurement conditions

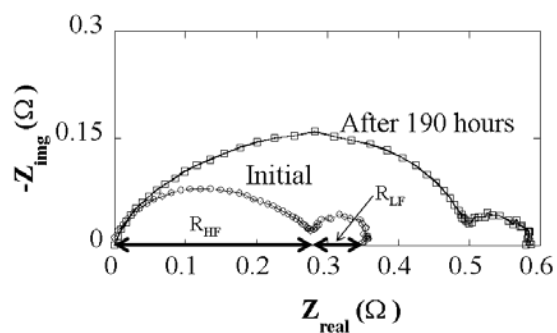


Figure 7-3. AC Impedance spectra of LSCF/GDC/LDCF in air at 800°C

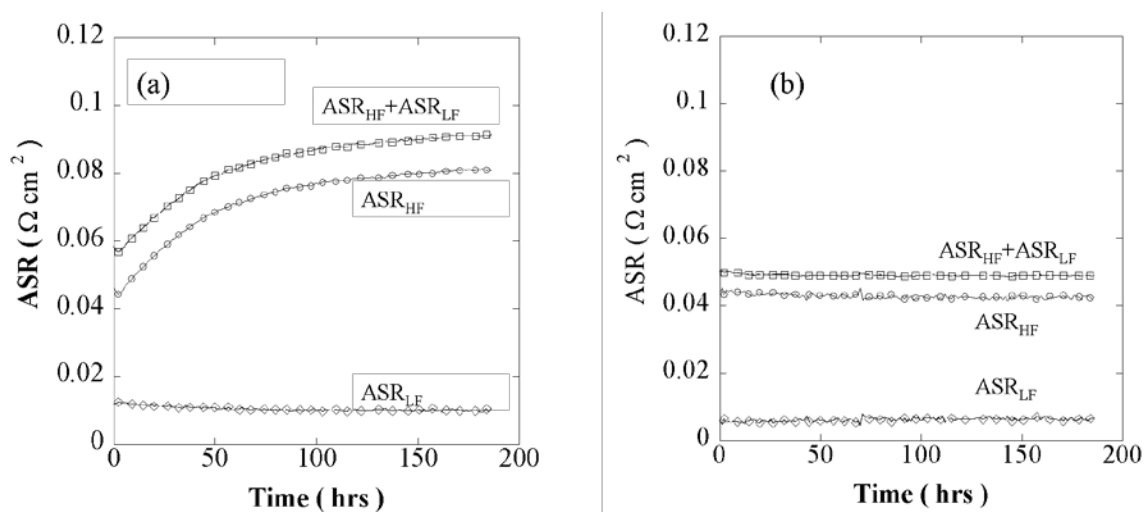


Figure 7-4. Area specific resistance of LSCF at 800°C in air as a function of aging time (a) in the (a) presence and (b) absence of K type thermocouple in the reactor.

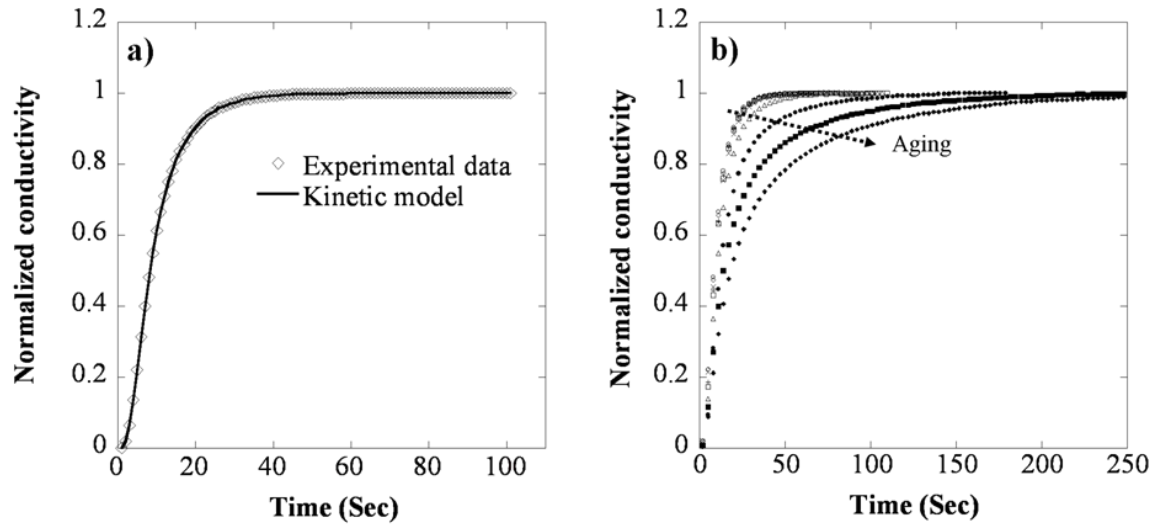


Figure 7-5. (a) Normalized electrical conductivity relaxation curve after switching oxygen partial pressure from 43 to 67% at $t = 0$ and (b) variation of relaxation curves with aging at 800°C .

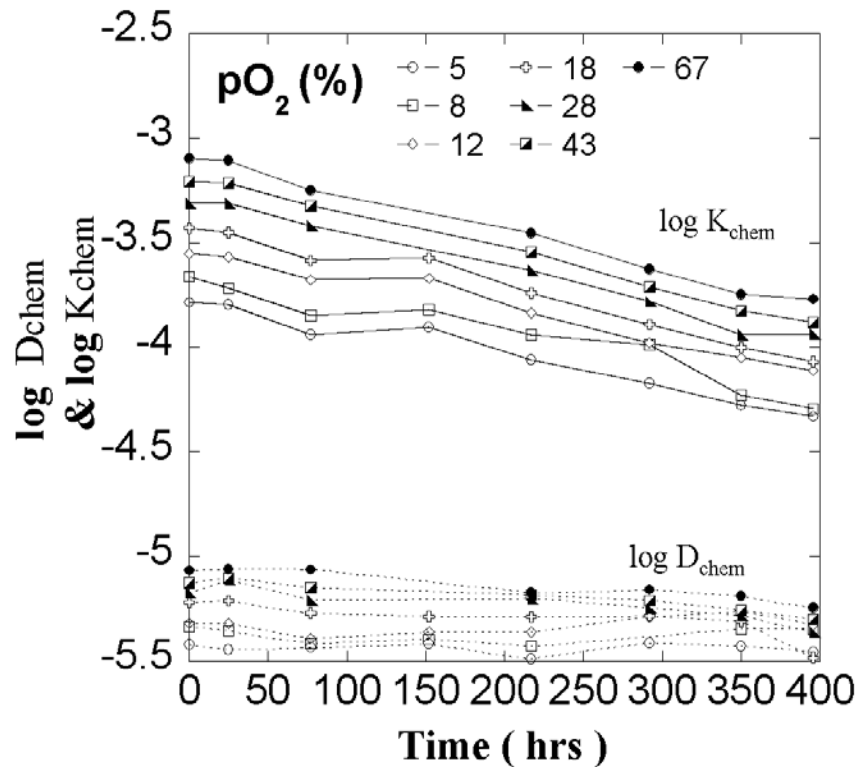


Figure 7-6. Degradation of K_{chem} and D_{chem} in Cr contaminated environment at 800°C

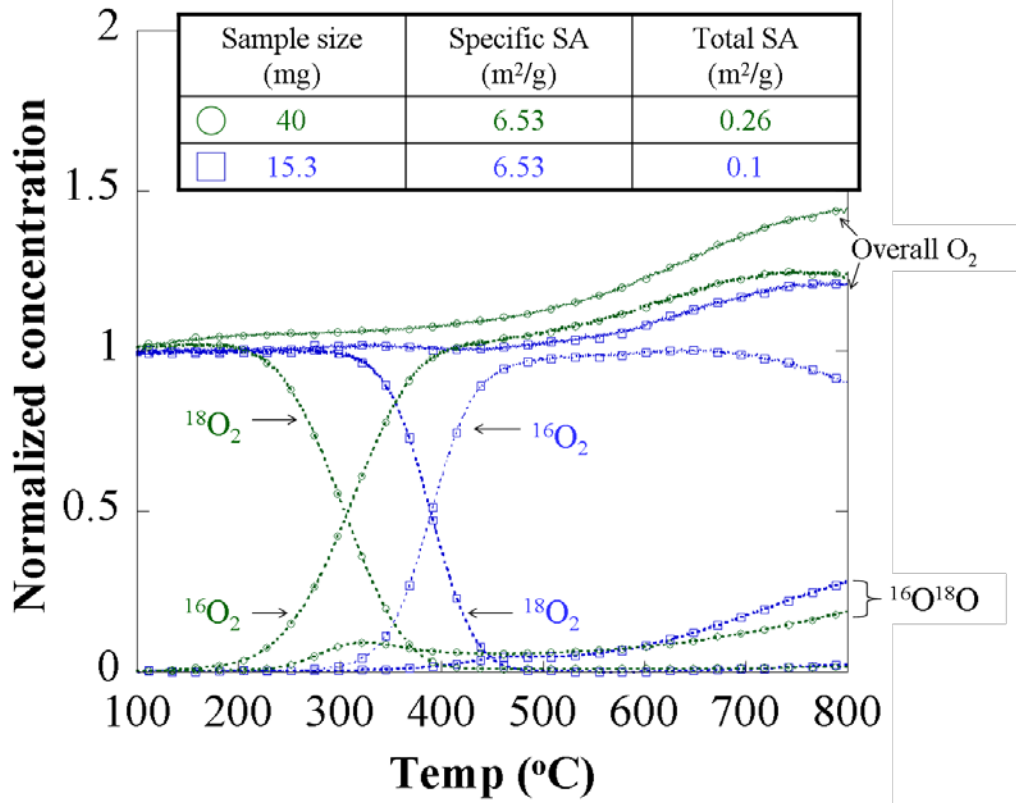


Figure 7-7. Effect of total surface area on oxygen exchange profiles which are measured by TPX. SA refers to the surface area.

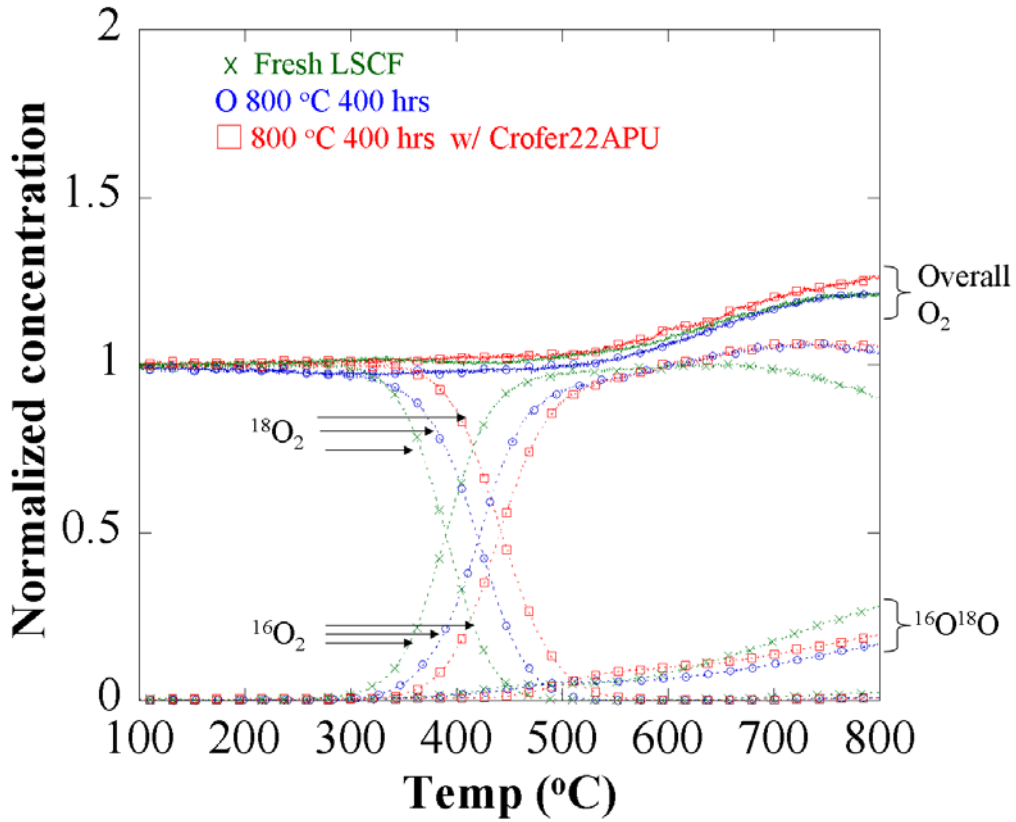


Figure 7-8. TPX result of heat treated LSCF at 800°C for 400 hours with and without exposure to Crofer22APU in comparison to fresh LSCF.

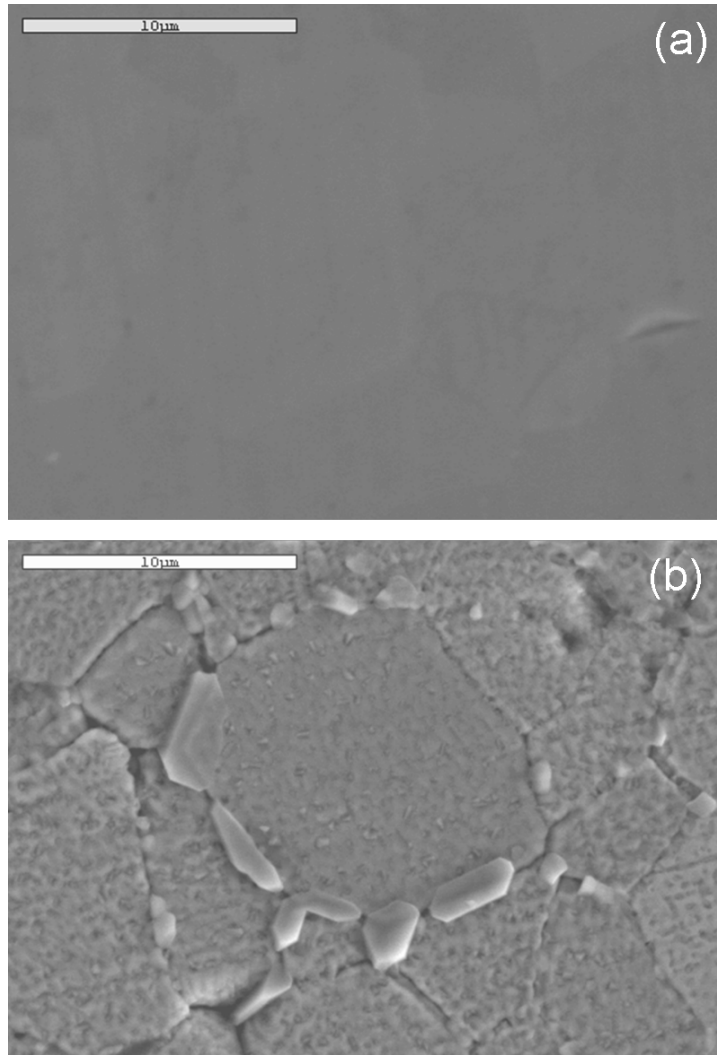


Figure 7-9. SEM micrographs of polished LSCF surfaces (a) before and (b) after ECR at 800°C for 400 hours.

Table 7-1. Samples tested in TPX

Heat treatment conditions		Specific SA* (m ² /g)	Sample size(mg)	Total SA (m ²)
Fresh LSCF		6.53	15.3	0.1
LSCF	800°C / 400 hours	4.38	22.8	0.1
LSCF w/ Crofer22APU	800°C / 400 hours	3.97	25.2	0.1

* SA is the surface area

Table 7-2. Elemental atomic percents (%) of LSCF obtained using EDS

		La	Sr	Co	Fe	O	Cr
Fresh		12	9	4	14	61	
Post ECR test at	Grain surface	17	9	4	19	51	
800°C for 400 hours	Particles	2	13	1	2	72	10

Table 7-3. Elemental atomic percents (%) of LSCF after ECR test at 800°C for 400 hours obtained using AES

	La	Sr	Co	Fe	O
Fresh	30	12	5	11	42
Post ECR test at 800°C for 400 hours*	38 (1)	0 (0)	2 (0.3)	8(0.6)	52
Heat treatment at 800°C for 50 hours in the absence of Cr contamination.	28 (0.9)	22 (1.8)	0 (0)	7 (0.6)	43

The enrichment factors are given in parenthesis.

* A grain surface was selected for the analysis.

CHAPTER 8 VAPORIZATION OF DOPED ALKALINE EARTH METAL OXIDE

8.1 Introduction

Doped Sr has been found to segregate in the surface region at high temperatures.^{59, 60} Bucher et al.⁵⁹ found Sr enrichment on the surface of LSCF using X-ray photoelectron spectroscopy (XPS) after electrical conductivity relaxation measurement at 600-700°C. Similarly Simner et al.³⁸ found Sr enrichment at the cathode-electrolyte and cathode-current collector interfaces after testing a button cell at 750°C for 500 hours. This study observed that Sr in LSCF not only enriched to the surface but also precipitated into SrO under oxidizing condition between 600-900°C. As a heterogeneous catalyst, the surface reaction is primarily affected by surface composition, and therefore such surface segregation of catalytically inactive element can lead to degradation of cathode performance.

Recently, Bishop et al.¹²⁰ reported a slow mass reduction of a dense $\text{La}_{0.6}\text{Sr}_{0.4}\text{Co}_{0.2}\text{Fe}_{0.8}\text{O}_{3-\delta}$ bar under isothermal conditions in air during thermogravimetric measurements. The mass reduction was small, but it continued over 200 hours, of which this time scale is substantially longer than that of oxygen diffusion or oxygen exchange reaction at the surface. Elemental segregation phenomena in the surface region may occur during long term heat treatments, but such a mechanism is not suitable for justifying mass reduction.^{71, 80} Previously, Mai et al.¹²⁵ tested the effect of a $\text{Ce}_{0.8}\text{Gd}_{0.2}\text{O}_2$ (GDC) interlayer between LSCF cathode and a $\text{Zr}_{0.92}\text{Y}_{0.08}\text{O}_2$ (YSZ) electrolyte in order to prevent chemical reactions between the LSCF and YSZ during sintering. They found that SrZrO_3 was formed at the YSZ interface when the GDC interlayer was porous while no Sr diffusion occurred when the interlayer was dense.

This indicates that Sr was likely to transport from the LSCF cathode to the YSZ electrolyte via vapor phase diffusion. The objective of this study was to improve the understanding of the effect of doped alkaline earth metal ions on surface structure at high temperature. Based on observations in literatures, it was hypothesized that doped Sr was vaporized in the vicinity of the surface region and a simple heat treatment experiment was conducted to prove the hypothesis.

8.2 Experimental

LSM was exposed to a stagnant dry atmosphere at 800°C for 50 hours. Samples were heat treated in the presence of Crofer22APU sheets and BaO (or LSCF powder) as described in Figure 8-1a. Also, LSM was heat treated with exposure to LSCF powder and Crofer22APU as described in Figure 8-1b in order to reduce the separation distance between the LSM surface and the LSCF powder.

8.3 Results and Discussion

Figure 8-2 shows the SEM micrographs of as-polished and heat treated LSM. Heat treatment was conducted in the same conditions as for the LSCF. In contrast to the results for LSCF, LSM shows no formation of secondary phase after heat treatment. This means that LSM must not react with Cr vapor species at 800°C. However, when LSM was heat treated at higher temperatures, the formation of secondary phases was found. Figure 8-3a shows the SEM micrographs of LSM after heat treatment at 1050°C in the presence of Crofer22APU. The formation of faceted particles is clearly observed. The EDS spectra for the LSM matrix and secondary phase are provided in Figure 8-3b and 5c, respectively. The characteristic peaks of Mn (K_{α_1} 5.899 keV) and Cr are pronounced while no Sr and La is found. This means that the secondary phase is a Mn-

Cr-O_x. It seems that Sr²⁺ in LSM is in a stable state, and as a result LSM reacts with Cr vapor differently than LSCF. Since A-site cations are the same for LSCF and LSM, the results indicate that the transition metals in B-site play a critical role for the reactivity to Cr vapor deposition.

Figure 8-4a represents the SEM micrograph of LSM surface after heat treatment at 800°C for 50 hours in the presence of Crofer22APU and BaO together. They are located as illustrated in Figure 8-1a. Compared to heat treated LSM in the absence of BaO, the formation of secondary phases was observed on the LSM surface. Figure 8-4b is the spot mode EDS spectrum for the particle. Compared to the EDS spectrum of as-polished LSM (Figure 8-3c), it shows the characteristic peaks of Ba (L_{α1} 4.466 keV) and Cr, proving the presence of Ba and Cr for the particle. It seems that the penetration depth of accelerated electron beam of SEM is deeper than the size of the particles and so EDS spectrum for the particle contains the characteristic peaks of LSM. During heat treatment, LSM was located above BaO powder without any direct contact. Therefore, the only way for BaO to deposit on LSM surface is through vapor phase diffusion, in which a vapor phase is formed from the BaO powder and mass transported to the LSM surface. As Ba vapor species are basic,¹²⁶ they interact with the acidic Cr vapor species, forming a salt on LSM surface.¹¹⁰ This study, therefore, shows that the vaporization of BaO cannot be neglected at substantially lower temperatures than boiling temperatures.

LSM was heat treated with exposure to LSCF powder and Crofer22APU together as described in Figure 8-1b. Figure 8-5a is the SEM micrographs of LSM after heat treatment at 800°C for 50 hours. It shows the formation of particles on grain boundary

after heat treatment. Figure 8-5b is the EDS spectrum for the particle. The intensity of the characteristic peak of Sr substantially increased compared to those of La and Mn. In addition, Cr was also found. It indicates that the particle is a Sr-Cr-O_x and the formation of Sr-Cr-O_x means the mass transport of Sr vapor from LSCF powder to LSM as same as BaO. Sr vapor species are also basic, and thus react with Cr vapor species, forming Sr-Cr-O_x on the surface of the LSM. This result supports that Sr in LSCF is vaporized in the vicinity of surface region at 800°C. Furthermore this helps explain the slow mass reduction, which was observed by Bishop et al.¹²⁰ The formation of Ba-Cr-O_x was found over the entire surface of LSM when it was heat treated with exposure to BaO and Crofer22APU. By contrast, the formation of Sr-Cr-O_x was found on the LSM surface only in the region near the LSCF powder, which is marked by the dotted box in Figure 1b, and the most area remained unchanged. This means vaporization of Sr from LSCF occurs in the vicinity of surface region.

8.4 Conclusions

Sr vaporization from LSCF was tested by comparing Cr contamination behavior on LSCF and LSM at high temperature. Heat treatment of LSCF with exposure to Crofer22APU at 800°C for 50 hours led to the formation of Sr-Cr-O_x particle on LSCF surface. By contrast, no Cr vapor deposition occurred on LSM at 800°C, and the formation of Cr-Mn-O_x particle was found at 1050°C. It seems that Sr in LSM is in stable state and so it does not react with Cr vapor species. When LSM was exposed to BaO and Crofer22APU at 800°C, the formation of Ba-Cr-O_x particles was found. Since there was no direct contact between BaO powder and LSM, it indicated that BaO was vaporized and transported to LSM surface. In a same way, the formation of Sr-Cr-O_x was found when LSM was heat treated in the presence of LSCF powder and

Crofer22APU at 800°C. The result well supports that Sr in LSCF is vaporized in the vicinity of surface region. As a heterogeneous catalyst, such vaporization of Sr from LSCF may degrade the catalytic activity and long term performance.

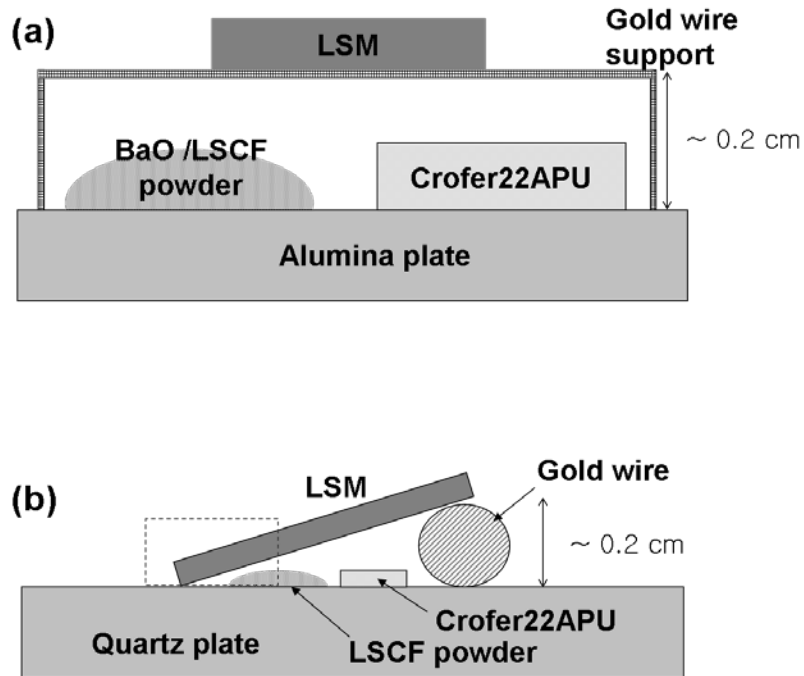


Figure 8-1. Schematic of experimental set up.

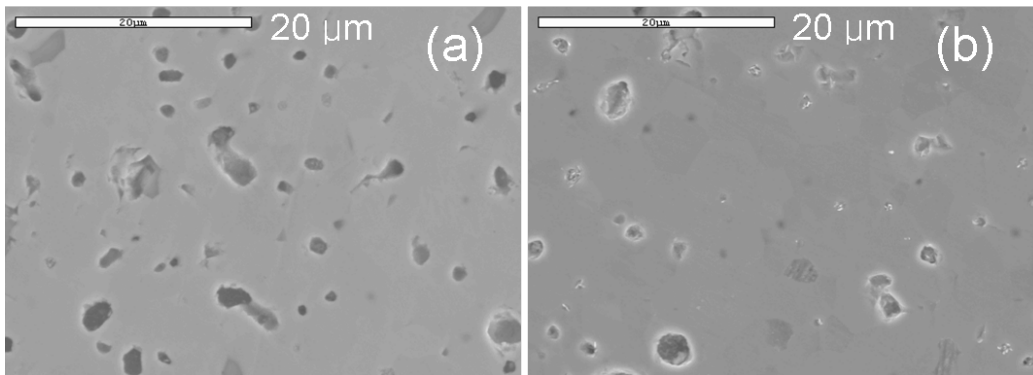


Figure 8-2. SEM micrographs of (a) as-polished and (b) heat treated LSCF in the presence of Crofer22APU.

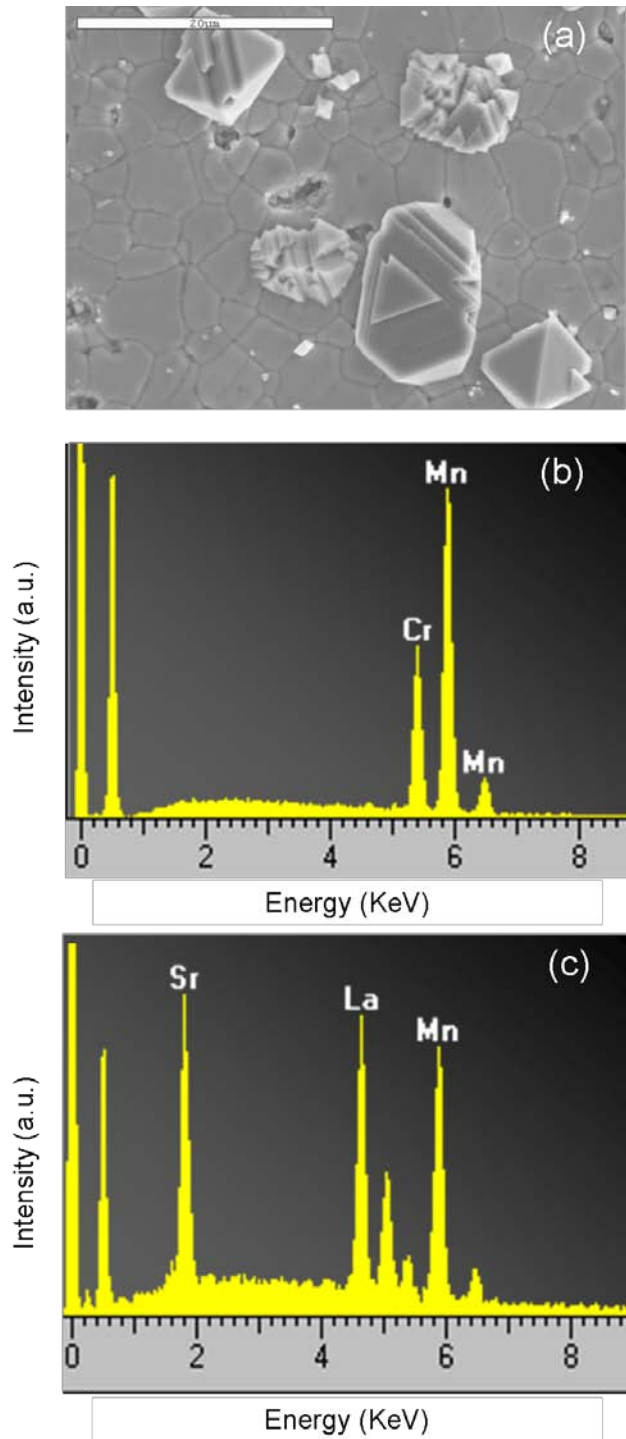


Figure 8-3. (a) LSM surface after heat treatment at 1050°C for 50 hours in the presence of Crofer22APU sheet. EDS spectra for (b) the newly formed particle after heat treatment and (c) as polished LSM sample.

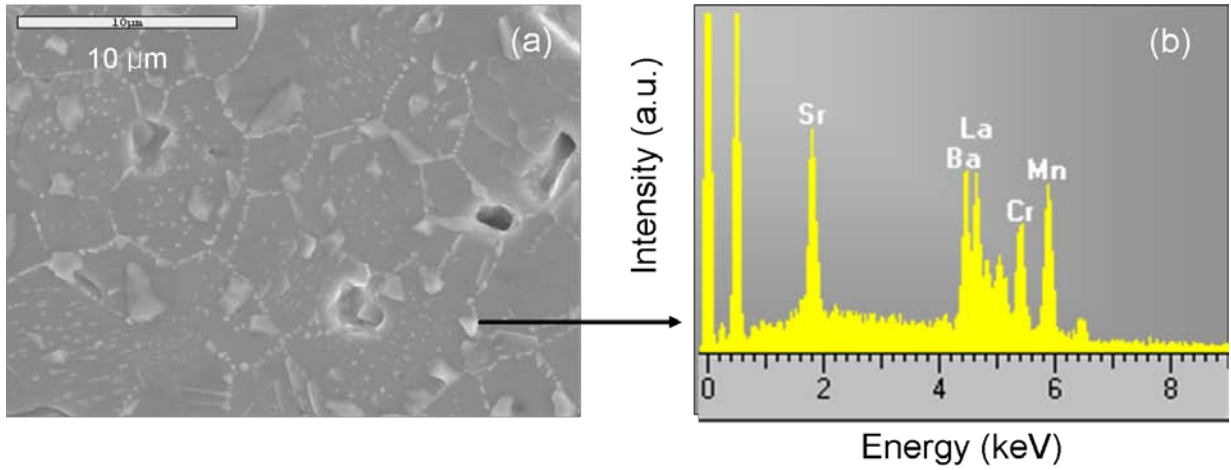


Figure 8-4. (a) Surface of LSM after heat treatment at 800°C for 50 hours in the presence of BaO powder and Crofer22APU. (b) Spot mode EDS spectra for the particle.

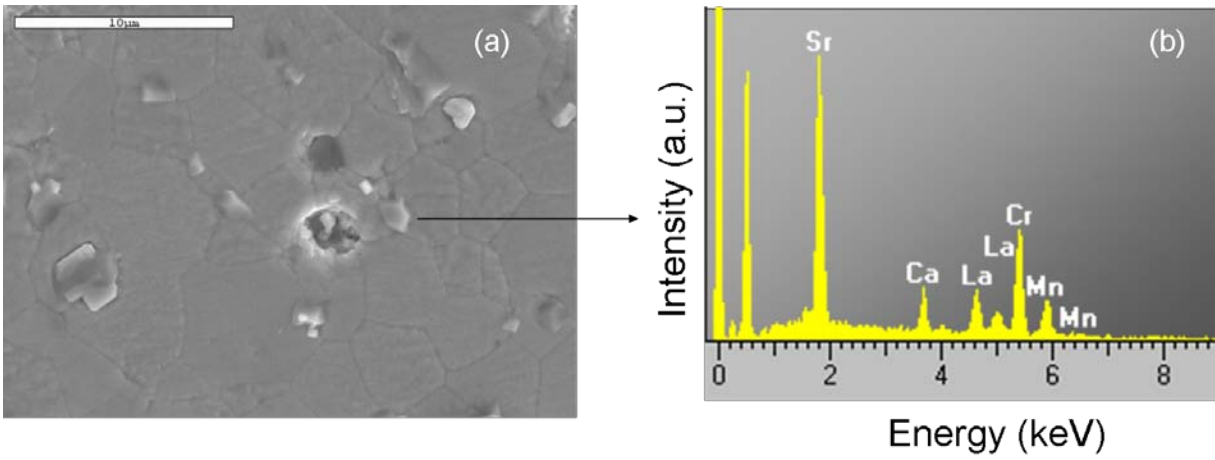


Figure 8-5. (a) SEM micrograph of heat treated LSM surface with exposure to

CHAPTER 9 CONCLUSIONS

Surface characteristic of $\text{La}_{0.6}\text{Sr}_{0.4}\text{Co}_{0.2}\text{Fe}_{0.8}\text{O}_3$ in the absence of and presence of Cr contamination have been investigated in order to better understand degradation mechanisms and improve the SOFC cathode performance. In many studies, the oxygen non-stoichiometry at high temperatures is a major concern for SOFC cathode materials, and thus A site ions on ABO_3 perovskite materials are partially substituted with the ions having a lower oxidation state to create more oxygen vacancies in the lattice. But this study showed that some doped Sr tended to segregate in the surface region at high temperatures and formed catalytically inactive layers. AES and TEM provided that segregated Sr in $\text{La}_{0.6}\text{Sr}_{0.4}\text{Co}_{0.2}\text{Fe}_{0.8}\text{O}_3$ (LSCF) precipitated into SrO_x and grew on top of the surface. It seems that excess surface energy due to increase in oxygen vacancies lead to the precipitation of cations.

Sr segregation led to reduction in the concentration of transition metals on the surface region, which might bring significant reduction in catalytic activity for oxygen reduction. In order to improve its performance, cobalt oxide was impregnated into a porous LSCF cathode via wet impregnation and its effects were tested. The ASR of the electrode was reduced and the maximum power density of a single LSCF cathode cell was significantly improved. It seems that increased concentration of cobalt oxide on the surface enhances surface reaction, especially charge transfer process. But the possibility of removal of Sr enriched surface layer cannot be ruled out. While a catalyst impregnation has been widely used previously, mostly expensive materials such as Pt and Pd were applied. In this study, based on the result of surface characterization,

SOFC performance was improved through Co impregnation without incurring significant increase in material costs.

In the meanwhile, SOFCs need to be operated in a stack, in which Fe-Cr alloys are used for the interconnect. At high temperatures, Cr was found to vaporize from these metal alloys and deposit on the cathodes. Electrical conductivity relaxation, AC impedance spectroscopy and temperature programmed isotopic exchange (TPX) consistently showed that surface reaction kinetics of LSCF was substantially decreased in Cr contamination environment. This degradation is attributed to the formation of SrCrO_4 particles and Sr deficient matrix on LSCF surface in Cr contamination condition. A phase transition from rhombohedral to cubic structure occurred and Fe_2O_3 was formed in the near surface region due to Sr deficiency. It was found that the reactivity between ABO_3 perovskite materials and Cr vapor species was not primarily determined by basicity of A site ions but by B site transition metals. Unstable Co^{4+} and Fe^{4+} lead to the formation of a nucleation agent for the chemical reaction while stable Mn^{4+} does not form a nucleation agent. Therefore, Cr contamination is a chemical process for Co-Fe based materials and an electrochemical process for Mn based materials.

Finally this study identifies that doped Sr in LSCF not only precipitates on the surface but also vaporizes in the vicinity of the surface region. As LSCF is a heterogeneous catalyst, this effect can play crucial role in its electrochemical performance.

APPENDIX A
THEORETIC EQUILIBRIUM VOLTAGE

At 800°C the Nernst equation can be written as

$$E_{\text{Eq}} = E_{\text{T}}^0 - \frac{RT}{nF} \ln \left(\frac{p_{\text{H}_2\text{O}}^2}{p_{\text{O}_2} \cdot p_{\text{H}_2}^2} \right) = E_{923\text{K}}^0 - \frac{8.3144\text{J/mol} \cdot \text{K} \cdot 1073\text{K}}{4 \cdot 96485\text{C/mol}} \ln \left(\frac{P_{\text{H}_2\text{O}}^2}{0.21 \cdot P_{\text{H}_2}^2} \right) \quad (\text{A-1})$$

If it is assumed that gaseous pressures at anode and cathode sides are the same as the atmospheric pressure, the pressure (p) is replaced by unit-less partial pressure (P).

In order to solve Eq. A-1, the standard voltage variation with temperature (E_{T}^0), and partial pressure of H_2O (g) and H_2 (g) are necessary. First, E_{T}^0 may be derived from the variation of standard free energy with temperatures. At constant pressures, the standard free energy change (ΔG°) is written as

$$\left(\frac{d\Delta G^\circ}{dT} \right)_p = -\Delta S^\circ \quad (\text{A-2})$$

where ΔS° is the standard entropy change. Generally, the temperature dependence of ΔS° is insignificant and thus, if ΔS° is assumed to be independent of temperature, integral of Eq. 2-11 from 298.15 K to an arbitrary temperature (T) gives

$$\begin{aligned} \Delta G_{\text{T}}^\circ &= \Delta G_{298.15\text{K}}^\circ - \Delta S_{298.15\text{K}}^\circ \cdot (T - T_{298.15\text{K}}) \\ &= (\Delta G_{298.15\text{K}}^\circ + \Delta S_{298.15\text{K}}^\circ \cdot T_{298.15\text{K}}) - \Delta S_{298.15\text{K}}^\circ \cdot T \end{aligned} \quad (\text{A-3})$$

This is in the form of

$$\Delta G_{\text{T}}^\circ = A + B \cdot T \quad (\text{A-4})$$

Table A-1 provides the thermodynamic properties of reactants and products. $\Delta G_{298.15K}^{\circ}$ and $\Delta S_{298.15K}^{\circ}$ are -228.57 kJ/mol and -88.86 J/mol·K, respectively. Thus, A is -484,000 J/mol and B is 88.86 J/mol·K. Therefore, E_T° at 800°C is

$$E_T^{\circ} = -\frac{\Delta G_T^{\circ}}{nF} = -\frac{-484000\text{J/mol} + 88.86\text{J/mol}\cdot\text{K} \times 1073\text{K}}{4 \cdot 96485\text{C/mol}} = 1.01\text{V} \quad (\text{A-5})$$

Approximate values of $P_{\text{H}_2\text{O}}$ and P_{H_2} can be obtained from the equilibrium vapor pressure of H_2O (g) using Clausius-Clapeyron equation.

$$\log p_{\text{H}_2\text{O}}(\text{atm}) = -\frac{2900}{T} - 4.65 \log T + 19.732 \quad (\text{A-6})$$

Since hydrogen gas flows through the anode via a water bath at room temperature (298.15K), $p_{\text{H}_2\text{O}} = 0.032$ atm and subsequently $P_{\text{H}_2} = 1 - 0.032 = 0.968$. From Eq. A-5 and A-6 the equilibrium voltage for an ideal case at 650°C is

$$E_{\text{Eq}} = 1.01\text{V} - \frac{8.3144\text{J/mol}\cdot\text{K} \cdot 1073\text{K}}{4 \cdot 96485\text{C/mol}} \ln\left(\frac{0.032^2}{0.21 \cdot 0.968^2}\right) = 1.13\text{V} \quad (\text{A-7})$$

Table A-1. Thermodynamic properties at 298.15K and 1bar

	G° (kJ/mol)	S° (J/mol·K)
O_2 (g)	0	205.14
H_2 (g)	0	130.68
H_2O (g)	-228.57	188.82

APPENDIX B
MEASUREMENT EFFECT OF NON-IDEAL STEP CHANGE IN ECR

A kinetic model of electrical conductivity relaxation (ECR) assumes the ideal step change of pO_2 inside of the reactor. In reality it takes certain amount of time to switch the gas concentration. Den otter et al. calculated the reactor flush time based on the continuous stirred tank reactor model (B-1)¹²⁷

$$\tau_f = \frac{V_r}{\Phi_{v,tot}} \frac{T_{STP}}{T_r} \quad (B-1)$$

where τ_f is the characteristic flush time, V_r it the dead volume, $\Phi_{v,tot}$ = total flow rate, T_{STP} =room temperature, and T_r = reactor temperature. They explained that 99% of gas inside the reactor would be replaced after the time of $4 \times \tau_f$ has passed. Based on Eq. B-1, the characteristic flush time of our reactor at 800°C with total flow rate of 500ccm was calculated according to

$$\tau_f = \frac{V_r}{\Phi_{v,tot}} \frac{T_{STP}}{T_r} = \frac{4.4cc}{\frac{500}{60}cc/sec} \times \frac{273K}{1073K} \approx 0.2sec \quad (B-2)$$

It takes about 0.8 sec to switch 99% gas inside of the reactor. The actual flush time was measured by connecting the output of ECR to Mass spectrometer (MS, Extrel QMS). In order to avoid damage on MS, the gas flow to MS was controlled to 30 sccm using the ball flow meter between two set-ups as seen in Figure B-1. Figure B-2 shows the oxygen concentration profile after switching a gas. Eq. B-3 was used to obtain characteristic flush time¹²⁸

$$p(t) = p_\infty + (p_0 - p_\infty) \exp\left(\frac{-t}{\tau_f}\right) \quad (B-3)$$

where t is the time, τ_f is the characteristic flush time, P_o , P_t and P_∞ are the initial, transient, and final pressures, respectively. The measured flush time was about 2.5 sec at 800°C. Based on this value and a kinetic model which accounts for the non ideal step change¹²⁷, experimental data was fit and compared with ideal step change model in Figure B-3. The non ideal step change kinetic model provided a more accurate fit at the early stage of exchanging reaction, however it did not affect much on the final values of D_{chem} and K_{chem} .

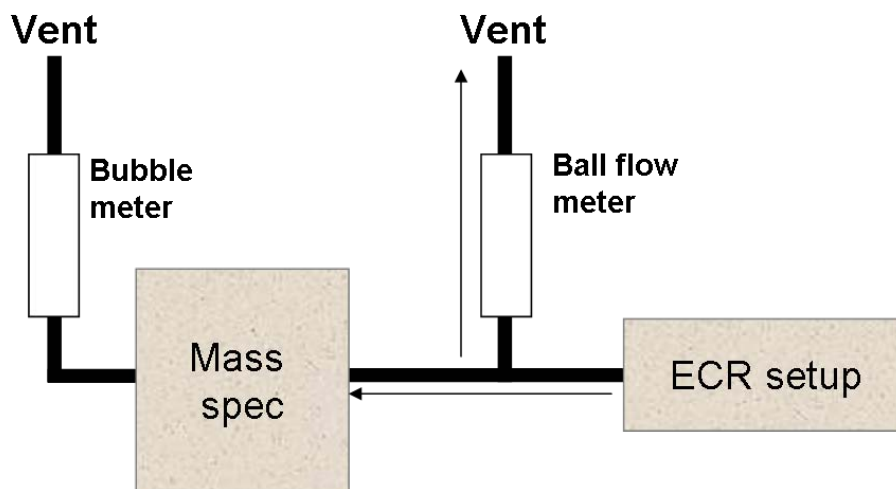


Figure B-1. Reactor flush time measurement set up using mass spectrometer. The flow from ECR to mass spec was limited to 30 sccm by the ball flow meter.

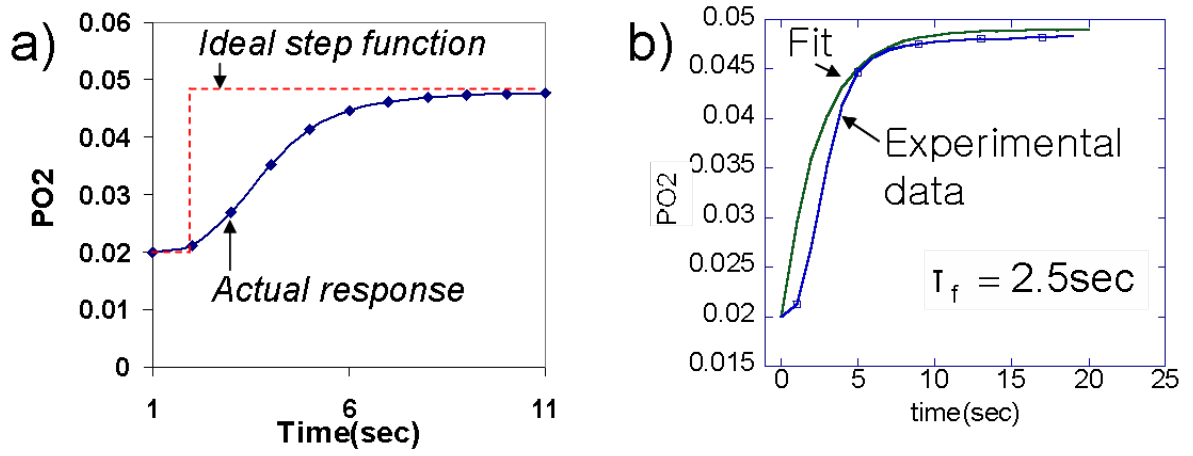


Figure B-2. Measured reactor flush time using mass spectrometer (a) and a fit using Eq B-3 (b).

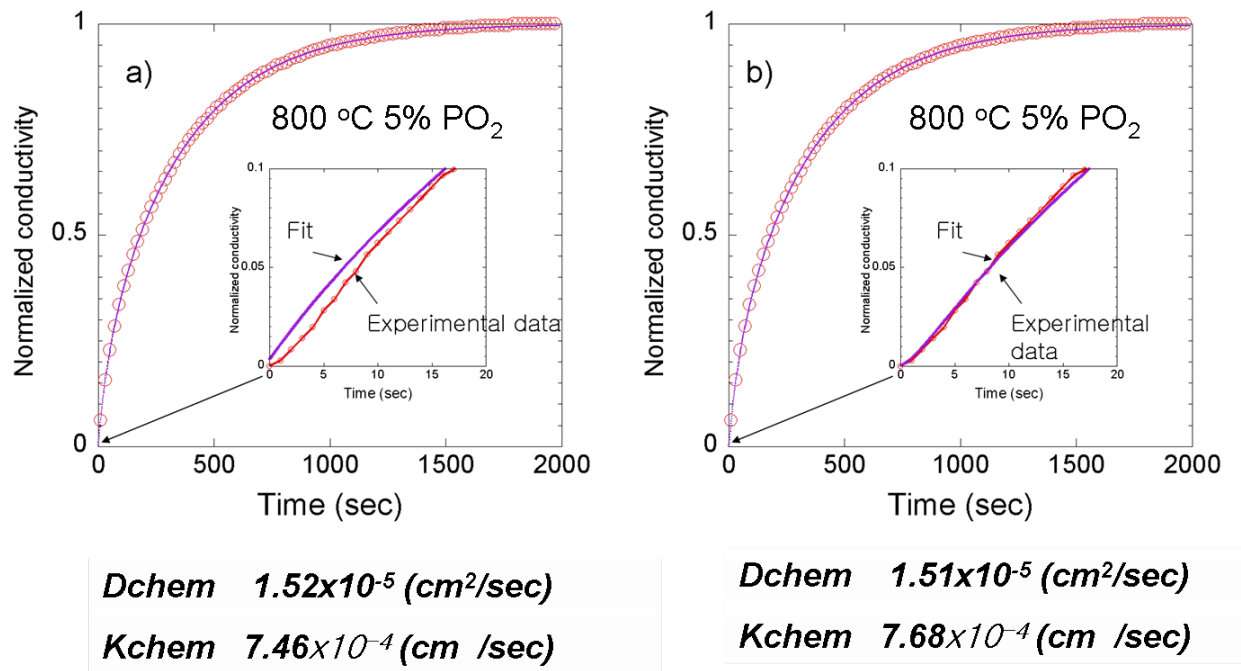


Figure B-3. A fit into experimental data using ideal step change model (a) and non-ideal step change (b) model.

CHAPTER C MEASUREMENT OF THE SURFACE SENSITIVE RATE COEFFICIENT USING ISOTHERMAL ISOTOPIC SWITCHING

C.1 Introduction

There were several attempts to get surface sensitive values by reducing the sample thickness. Chen et al.^{143, 144} made an epitaxial thin film of metal oxides with pulsed laser deposition (PLD) and measured the chemical exchange coefficient (K_{chem}). They found that K_{chem} was much smaller than that of the bulk polycrystalline coefficient. As Kim et al.¹²⁹ observed, this is because a preferentially oriented thin film has dissimilar surface properties than a polycrystalline sample. In addition, when a thin film grown on the single crystal substrate is tested at high temperatures, inter-diffusion across the interface of film and substrate can occur, changing the oxygen transport property. To overcome this limitation, Ganeshanathan et al.¹³⁰ prepared porous bulk polycrystalline samples with an average grain size of a few microns. They found that the magnitude of K_{chem} of $\text{La}_{0.6}\text{Sr}_{0.4}\text{CoO}_3$ was close to other data in the literature, but it increased as temperature decreased, suggesting an exothermic surface reaction process. The objective of this study is to introduce the application of a new experimental method to measure the surface sensitive reaction coefficient: isothermal isotopic switching. One of the benefits of this technique is easy sample preparation. Either fresh or heat treated powder can be tested without additional processing (such as pressing and polishing). Since mass spectrometry monitors the gas composition of the reactor *in situ* and in real time, electrode contacts to the samples aren't necessary. This avoids the potential contribution to the catalytic activity from triple phase boundaries along the contact¹³¹. Small particle size and high surface area powder samples can provide highly surface sensitive kinetic values. As an initial test, the surface exchange coefficient of

La_{0.6}Sr_{0.4}Co_{0.2}Fe_{0.8}O_{3-δ} (LSCF), an extensively studied material for intermediate temperature SOFC, was measured and compared to the literature.

C.2 Background

Cathode materials maintain a dynamic equilibrium with the external atmosphere at sufficiently high temperatures. When an oxygen isotope (¹⁸O₂) is introduced into the sample environment, which has been equilibrated with normal oxygen (¹⁶O₂), under constant overall oxygen partial pressure, the dynamic equilibrium will not be disturbed, but normal oxygen in the lattice will be displaced by isotopic oxygen. If isotopic effects are ignored, this can be expressed as



Direct measurement of the rate constant (k_{in} and k_{out}) is not possible due to lack of understanding of the mechanism. Instead, apparent rate coefficients can be measured assuming a first order reaction such that the flux in and out can be expressed by¹³⁰

$$J_{\text{in}} = \frac{dC(t)}{dt} = k_{\text{in}}^* [^{18}\text{C}_\text{o} - ^{18}\text{C}(t)] \cdot \frac{S}{V} \quad (\text{C- 3})$$

$$J_{\text{out}} = \frac{dC(t)}{dt} = k_{\text{out}}^* [^{16}\text{C}_\text{o} - ^{16}\text{C}(t)] \cdot \frac{S}{V} \quad (\text{C- 4})$$

where J is the flux, C_o is the new equilibrium concentration, $C(t)$ is the concentration at time t , V is the volume and S is the surface area. k_{in}^* and k_{out}^* are the surface exchange coefficients for incorporation and desorption, respectively. Since the sample is in quasi-equilibrium, it should satisfy $J_{\text{overall}} = J_{\text{in}} + J_{\text{out}} = 0$. Accordingly, k_{in}^* is equivalent to k_{out}^* when $\Delta C (^{18}\text{O}_2) = -\Delta C (^{16}\text{O}_2)$. If a spherical particle shape is assumed, integration of Eq. C-3 gives

$$g(t) = \frac{{}^{18}\text{C}_o - {}^{18}\text{C}(t)}{{}^{18}\text{C}_o - {}^{18}\text{C}(0)} = \exp\left[-\frac{t}{\frac{V}{S \cdot k_{in}^*}}\right] = \exp\left[-\frac{t}{\frac{r}{3 \cdot k_{in}^*}}\right] \quad (\text{C-5})$$

where, $C(0)$ is the initial equilibrium concentration and r is the average particle radius. Thus, fitting Eq. C-5 to the concentration profile of oxygen isotope obtained by mass spectrometry will provide surface exchange coefficients (k_{in}^*) values.

C.3 Experimental

Commercially available LSCF powder (Praxair) was used without additional modification. The specific surface area was $6.52 \text{ m}^2/\text{g}$ and the volume averaged particle radius was $1.4 \text{ }\mu\text{m}$ based on manufacturer provided particle size distribution data. The reactor schematic is the same at temperature programmed isotopic exchange set up. Due to small sample volume and no electrode connection, reactor size (i.d. = 4.12 mm , length = 10 cm and volume $\sim 1.33 \text{ cm}^3$) can be reduced and this ensures fast gas changing out time in the reactor with a relatively slow gas flow rate. If it follows a continuously stirred tank reactor model as suggested by den Otter et al¹²⁷, it takes less than 1 sec at 800°C with 20CCM . It would take even less time using the plug flow model. LSCF powder (0.015 g) was placed atop the glass frit in the middle of the reactor. The flow rate of the feed gas was controlled by mass flow controllers (MKS & Alicat) adjusted to yield a total flow rate of 20 CCM . Gas composition in feed stream was switched using an automatic switching valve (Veeco) and the reactor effluent was constantly sampled by a downstream mass spectrometer (Extrel). First the sample was pretreated under ${}^{16}\text{O}_2$ diluted with Helium for 30 mins at 800°C . Once the mass spectrometry signal reached steady state, the feed gas was switched to ${}^{18}\text{O}_2$. The total oxygen concentration was fixed to 10000 PPM . Time dependent relaxation curves were

monitored until a new steady state was reached. The measurements were performed at 700, 750 and 800°C.

C.4 Results and Discussion

Figure C-1 shows time dependent relaxation curve of normal and isotope oxygen after switching the gas composition from $^{16}\text{O}_2$ to $^{18}\text{O}_2$ at 700°C. $^{16}\text{O}+^{18}\text{O}$ represents a scrambled species formed on the surface by combining dissociatively adsorbed species ($^{18}\text{O}_{\text{ads}}$) and residual lattice oxygen (^{16}O). Its concentration increased rapidly but decreased as adsorbed ^{16}O diminishes. In Figure C-2, the amount of oxygen isotope incorporating into the lattice will be $(\text{isotope input} - ^{18}\text{O} + 1/2 * (^{16}\text{O} + ^{18}\text{O}))$ ppm and that of desorbed normal oxygen is equivalent to $(^{16}\text{O} + 1/2 * (^{16}\text{O} + ^{18}\text{O}))$. Relaxation curves reach a plateau in approximately 3000 seconds, indicating that the surface exchange reaction reached isotopic steady state. Right after gas switching, the concentration of $^{16}\text{O}_2$ appeared to overshoot, but this is probably due to pressure fluctuations during gas switching, which was also observed by Lane et al.⁴⁸ Despite the initial pressure fluctuation, the normalized relaxation curves of desorbed oxygen and incorporated oxygen isotopes were superimposed and were fit to Eq.C-5 (solid line) as shown in Figure C-2, giving $k_{\text{in}}^* = k_{\text{out}}^*$.

The measured surface exchange coefficient is converted to the chemical exchange coefficient for the comparison using the thermodynamic factor.⁹⁵ As shown in Figure C-3, the magnitude is lower than values reported in the literature and by our own measurements with the electrical conductivity method. It might be due to particle size distribution. Another possible explanation is different sample geometries and preparation procedures. Samples for both conductivity relaxation and IEDP were solid bars which were sintered at high temperatures to obtain sufficient density and then

polished with fine abrasives to produce a flat, well defined surface for more accurate estimation of surface kinetics.⁴⁹ This is in contrast this with our sample, which is a fine powder with a high surface area to volume ratio. As a result, the surface composition or structure of powder sample can be different from the dense polycrystalline bar, causing the difference in catalytic activities.

In order to calculate the activation energy of the surface reaction, experiments were conducted at three different temperatures. Figure C-4 shows the normalized relaxation curves of $^{18}\text{O}_2$ which shows that the relaxation time decreases as temperature decreases. Fig.6 shows the Arrhenius plot of k_{in}^* which yields an activation energy of -23 kJ/mol for the surface reaction. This means the surface reaction is exothermic while in most literature, an endothermic surface reaction for perovskite materials with similar chemical compositions has been observed.^{31, 132} Bouwmeester et al.⁵² reported an activation energy of 214 kJ/mol for the surface reaction of bulk polycrystalline LSCF and Chen et al.¹³³ observed the activation energy of approximately 160kJ/mol for $\text{La}_{0.5}\text{Sr}_{0.5}\text{CoO}_{3-\delta}$ epitaxial film. However, Ganeshanathan et al.¹³⁰ found that the activation energy of porous $\text{La}_{0.6}\text{Sr}_{0.4}\text{CoO}_{3-\delta}$ was around -23 kJ/mol, which is very close to that found from this study. There is one similar aspect between the powder and porous bulk sample. Both have substantially higher surface area than dense bulk polycrystalline. As shown in Figure C-4, the surface reaction coefficient increases with $p\text{O}_2$, this means that the rate expression for oxygen reduction should include a surface coverage term. As surface area becomes larger, surface coverage of adsorbed oxygen species may play a more important role in determining the apparent activation energy for surface reaction. Thus, the increase in surface coverage at reduced temperatures

might enhance the apparent reaction coefficient, giving negative activation energy. Whether this is due to high surface area or another factor's affect on measurement needs further analysis.

C.5 Conclusions

A new application for the isothermal isotope switching method was applied to measure surface sensitive reaction coefficients of LSCF. An in situ powder sample was tested without sintering and electrode contacts. The small sample volume allowed for a small reactor design, which reduced the gas switch time with relatively lower total gas flow than other experimental techniques. It shows that time dependent relaxation curves of normal and isotope oxygen can be fitted to a first order kinetic model. The magnitude of the surface exchange coefficient of the powder type sample used in this study was smaller than values reported in literature. That might be due to the different surface reactivity of fresh powder from dense bulk polycrystalline sample. Relaxation time for $^{18}\text{O}_2$ increased as temperature decreased, giving the activation energy of -23 kJ/mol for the oxygen reduction process. This is substantially different from previous results for dense perovskite materials, but it is close to that of porous bulk $\text{La}_{0.6}\text{Sr}_{0.4}\text{CoO}_{3-\delta}$. Surface coverage of oxygen appears to play a larger role in high surface area samples.

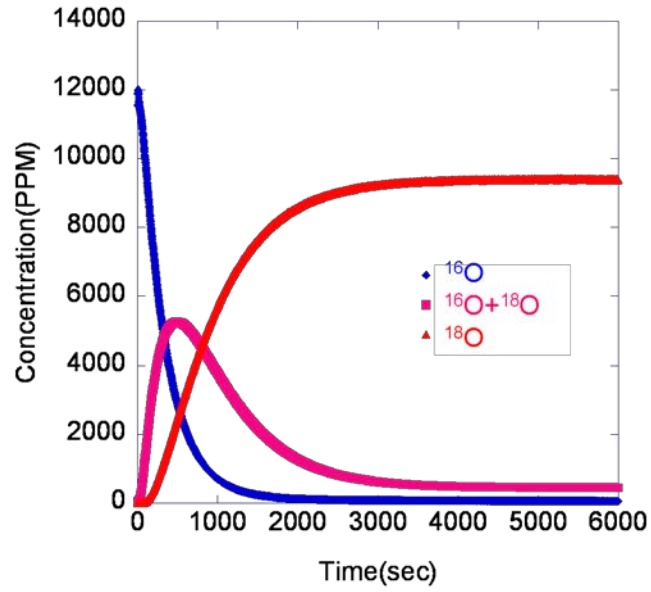


Figure C-1. Time dependent relaxation profile of normal oxygen (^{16}O), oxygen isotope (^{18}O) and scrambled oxygen ($^{16}\text{O}+^{18}\text{O}$) at 700°C

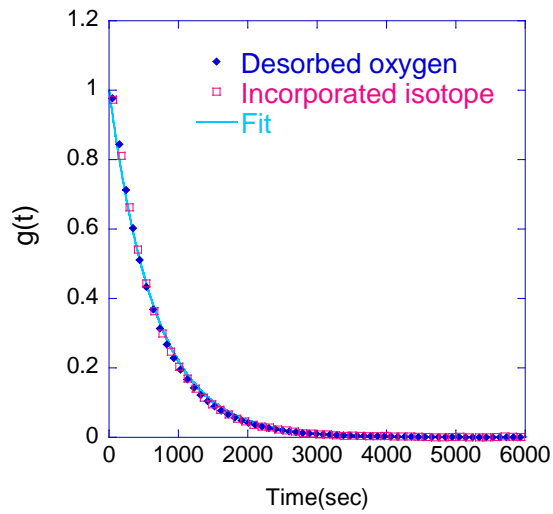


Figure C-2. Normalized concentrations of desorbed oxygen from the sample and incorporated oxygen

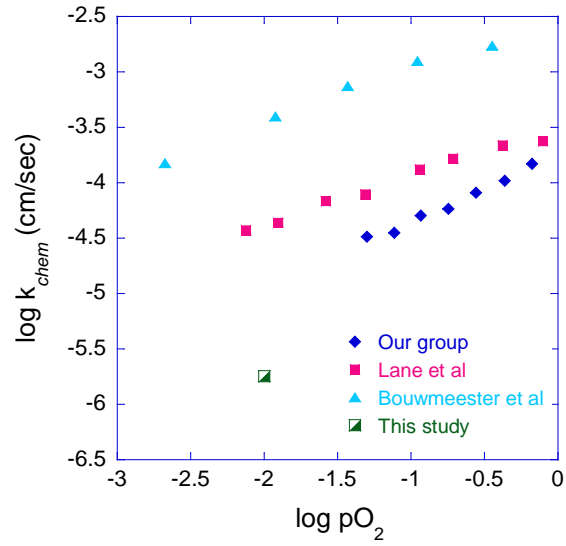


Figure C-3. k_{chem} measured by ECR in this study and literatures^{52, 94}, converted using the thermodynamic factor, at 800°C.

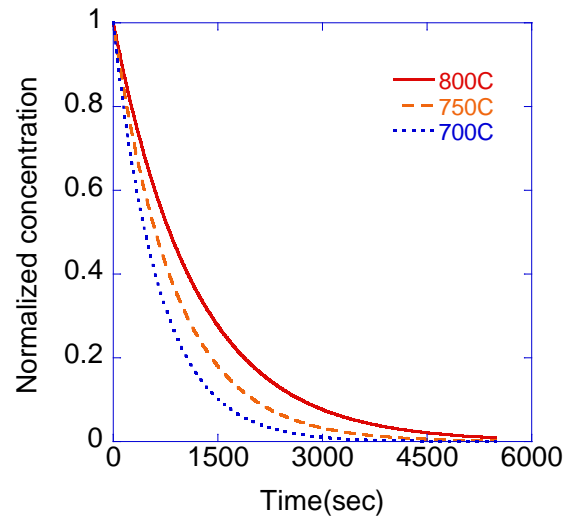


Figure C-4. Normalized relaxation curves of incorporated oxygen isotope at different temperatures.

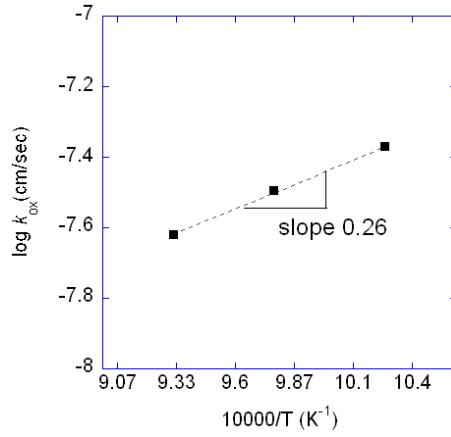


Figure C-5. Arrhenius plot of surface exchange coefficient ($pO_2= 0.01$)

APPENDIX D
TAPE CASTING SLURRY COMPOSITION

The tape-casting procedure was introduced in Chapter 5. The slurry compositions for 8YSZ, 10GDC, NiO and glass powder are given in Table D-1.

Table D-1. Tape casting slurry composition.

	Weight (g)	wt%		Weight (g)	wt%
8YSZ (Tosho)	100	52.1	10GDC (Anan)	50	40.4
Fish oil*	1	0.5	Fish oil	1.5	1.2
DBP	14	7.3	DBP	7	5.7
PVB	10	5.2	PVB	5	4.0
Toluene	38.2	19.9	Toluene	36.7	29.7
ETOH	25.7	13.4	ETOH	22	17.8
PEG8000	3	1.6	PEG8000	1.5	1.2
Total	192	100	Total	123.7	100
	Weight (g)	wt%		Weight (g)	wt%
NiO	140	55.0	Glass	110	89.4
Fish oil	1.5	0.6	Fish oil	2.1	1.7
DBP	9.8	3.9	DBP	9.8	8.0
PVB	17	6.7	PVB	12	9.8
Toluene	47	18.5	Toluene	41	33.3
ETOH	37	14.5	ETOH	27	22.0
PEG8000	2.2	0.9	PEG8000	5.1	4.1
Total	254.5	100.0	Total	207	168

Menhaden fish oil*

APPENDIX E CR CONTAMINATION ON LSM82

$\text{La}_{0.8}\text{Sr}_{0.2}\text{MnO}_3$ (LSM82) is the composition, which is more widely used for SOFC cathodes than $\text{La}_{0.6}\text{Sr}_{0.4}\text{MnO}_3$ (LSM64), which was tested in this study. LSM82 was tested in a same way that LSM 64 was tested. The powder (Fuel Cell Materials) was uniaxially pressed and then sintered at 1450°C . Figure E-1a shows the as-polished surface of LSM82. EDS analysis provided that the darker regions were Mn rich oxide. Figure E-1b represents the LSM after heat treatment with exposure to Crofer22APU at 800°C for 50 hours. It shows no Cr vapor deposition on the surface. This is in agreement with LSM64, which indicates that $(\text{La}_{1-x}\text{Sr}_x)\text{MnO}_3$ does not react with Cr vapor species at 800°C .

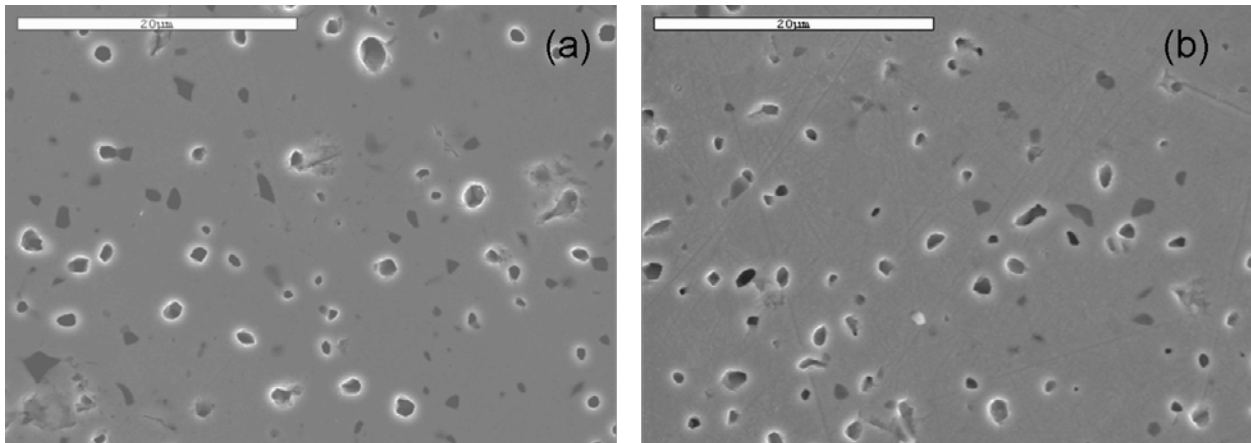


Figure E-1 (a) As-polished LSM82 surface and (b) heat treated LSM82 at 800°C for 50hrs in the presence of Crofer22APU.

APPENDIX F
K_{CHEM} AND D_{CHEM} AT 750°C

The D_{chem} and K_{chem} at 750°C were obtained using electrical conductivity relaxation and plotted as a function of oxygen partial pressure in Figure F-1. The characteristic dependencies of K_{chem} and D_{chem} are close to that at 800°C, meaning that the rate limiting step of LSCF is a charge transfer between LSCF and oxygen gas. Figure F-2 shows the degradation rate of K_{chem} at 750°C either. Surface reaction rate decreased at a relative fast rate during the 70 hours and at a slower rate after 70 hours. Interestingly, the degradation rate was increased with increasing pO₂.

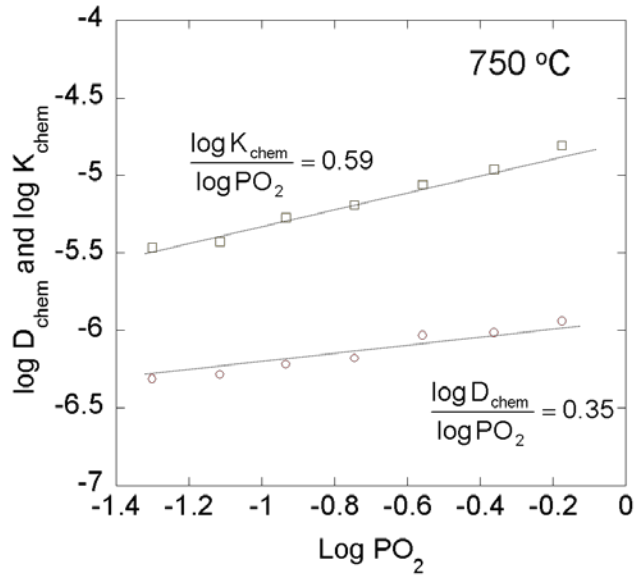


Figure F-1. D_{chem} and K_{chem} at 750°C as a function of pO₂.

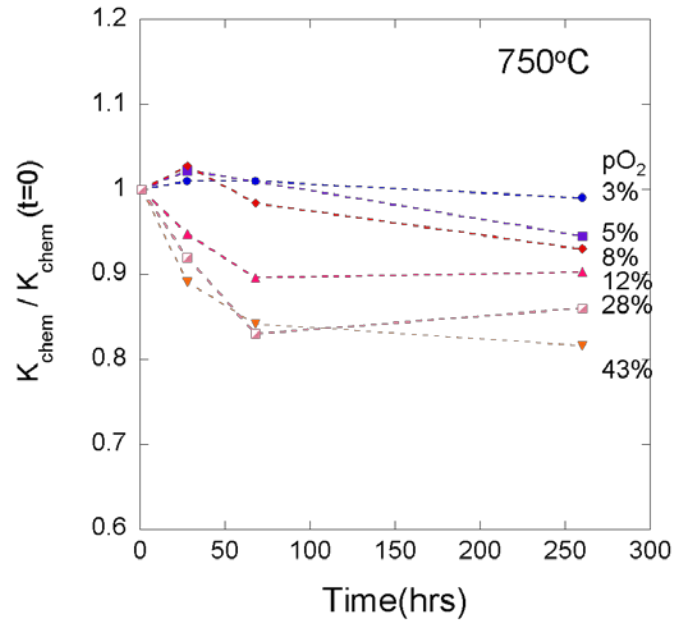


Figure F-2. Degradation of K_{chem} at 750°C.

APPENDIX G
SURFACE VARIATION OF LCCF AND LBCF

Figure G-1 shows the differentiated AES spectra of $\text{La}_{0.6}\text{Ca}_{0.4}\text{Co}_{0.2}\text{Fe}_{0.8}\text{O}_3$ (LCCF) and $\text{La}_{0.6}\text{Ba}_{0.4}\text{Co}_{0.2}\text{Fe}_{0.8}\text{O}_3$ (LBCF). In comparison to the AES spectrum of the pre-heat treated sample, LBCF showed an increase in the characteristic peak of Ba after heat treatment at 800°C for 50 hrs. By contrast, the AES spectra of LCCF presented weak change after heat treatment. There is no doubt that the concentration of Ba increased while that of rest elements decreased but the elemental atomic percents of LBCF may not be accurate due to peak overlapping. LSCF and LBCF showed similar behavior, but LCCF showed weak segregation of elements. The tendency of segregation in doped alkaline earth metal oxides is $\text{Ca} < \text{Sr} \approx \text{Ba}$. Further systematic study is required to explain difference segregation tendency.

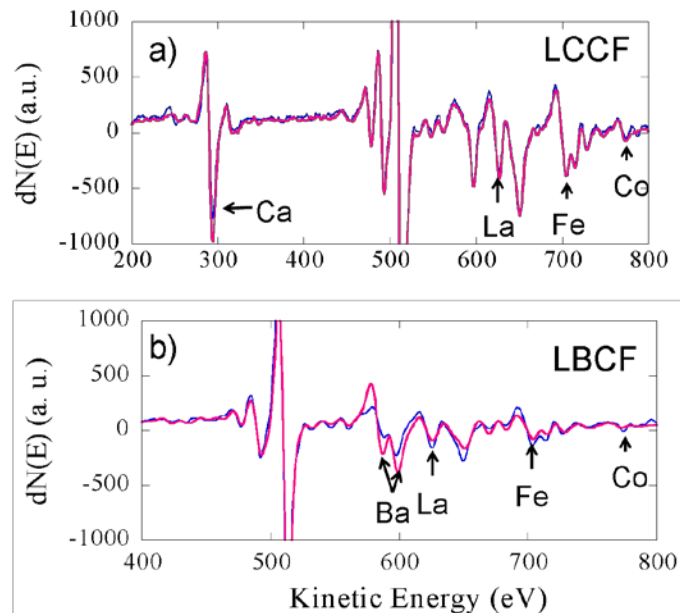


Figure G-1. Differentiated Auger electron spectra for pre (blue) and post (red) heat treated samples at 800°C for 50 hrs. (a) LCCF and (b) LBCF

APPENDIX H
COBALT OXIDE DISPERSION ON LSCF SURFACE

Co nitrate solution was prepared by dissolving $\text{Co}(\text{NO}_3)_2 \cdot 6\text{H}_2\text{O}$ and PEG 14g in mixture of ethanol and water. It was dip-coated and heat treated at 700 and 900°C, respectively. Figure G-1 shows the formation of nano cobalt oxide on the surface of LSCF.

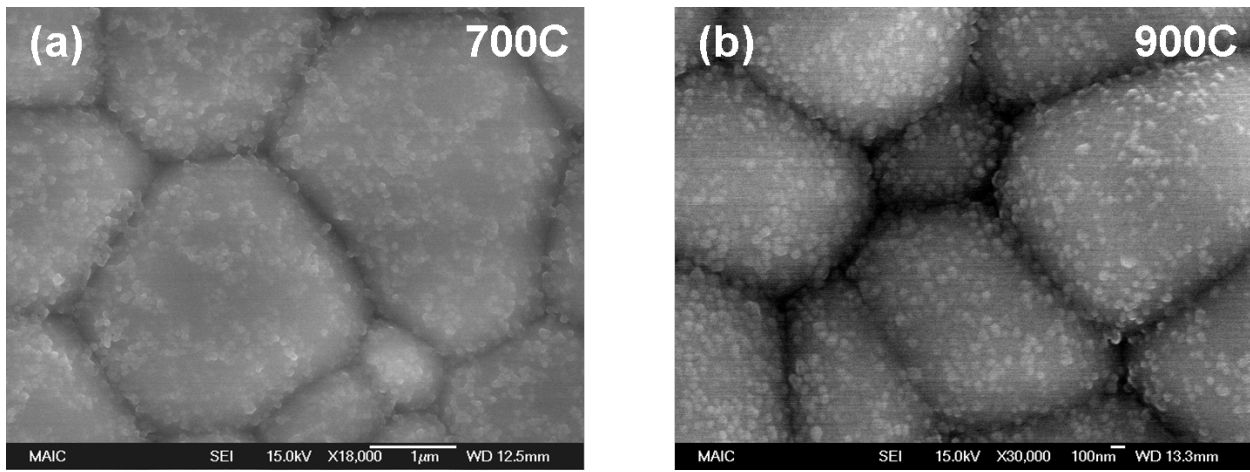


Figure H-1. LSCF surface after heat treating Co dip-coated LSCF

LIST OF REFERENCES

1. R. E. Smalley, *Mrs Bulletin*, 2005, **30**, 412-417.
2. C. J. Campbell and J. H. Laherrere, *Scientific American*, 1998, **278**, 77-83.
3. N. Stern, *The economics of climate change : the Stern review*, Cambridge University Press, Cambridge, UK, 2007.
4. B. C. H. Steele and A. Heinzl, *Nature*, 2001, **414**, 345-352.
5. S. M. Haile, *Acta Materialia*, 2003, **51**, 5981-6000.
6. O. Yamamoto, *Electrochimica Acta*, 2000, **45**, 2423-2435.
7. R. M. Ormerod, *Chem. Soc. Rev.*, 2003, **32**, 17-28.
8. T. Ishihara, *Perovskite Oxide for Solid Oxide Fuel Cells* Springer, New York, 2009.
9. P. Singh and N. Q. Minh, *International Journal of Applied Ceramic Technology*, 2004, **1**, 5-15.
10. R. O'hayre, S.-W. Cha, W. Colella and F. B. Prinz, *Fuel Cell Fundamentals* John Wiley & Sons New York, 2006.
11. M. C. Williams, J. P. Strakey, W. A. Surdoval and L. C. Wilson, *Solid State Ionics*, 2006, **177**, 2039-2044.
12. E. Fontell, T. Kivisaari, N. Christiansen, J. B. Hansen and J. Palsson, *Journal of Power Sources*, 2004, **131**, 49-56.
13. E. Riensche, U. Stimming and G. Unverzagt, *Journal of Power Sources*, 1998, **73**, 251-256.
14. J. W. Fergus, *Materials Science and Engineering A*, 2005, **397**, 271-283.
15. M. W. Barsoum, *Fundamentals of ceramics*, McGraw-Hill, London, 2003.
16. H. Ricket, *Electrochemistry of Solids: An Introduction* Spring-Verlag, New York 1982.
17. S. B. Adler, X. Y. Chen and J. R. Wilson, *Journal of Catalysis*, 2007, **245**, 91-109.
18. S. P. S. Badwal and K. Foger, *Ceramics International*, 1996, **22**, 257-265.
19. W. Z. Zhu and S. C. Deevi, *Materials research bulletin* 2003, **38**, 957-972.
20. H. Y. Zhu and R. J. Kee, *Journal of Power Sources*, 2006, **161**, 957-964.

21. R. W. Sidwell and W. G. Coors, *Journal of Power Sources*, 2005, **143**, 166-172.
22. K. C. Wincewicz and J. S. Cooper, *Journal of Power Sources*, 2005, **140**, 280-296.
23. S. B. Adler, *Chemical Reviews*, 2004, **104**, 4791-4843.
24. T. Shimizu, *Chemistry Letters*, 1980, 1-4.
25. J. Nowotny, T. Bak, M. K. Nowotny and C. C. Sorrell, *Advances in Applied Ceramics*, 2005, **104**, 154-164.
26. R. Hammami, H. Batis and C. Minot, *Surface Science*, 2009, **603**, 3057-3067.
27. Y. J. Leng, S. H. Chan and Q. L. Liu, *International Journal of Hydrogen Energy*, 2008, **33**, 3808-3817.
28. T. Nitadori, T. Ichiki and M. Misono, *Bulletin of the Chemical Society of Japan*, 1988, **61**, 621-626.
29. T. Nakamura, M. Misono and Y. Yoneda, *Bulletin of the Chemical Society of Japan*, 1982, **55**, 394-399.
30. I. Yasuda and T. Hikita, *Journal of the Electrochemical Society*, 1994, **141**, 1268-1273.
31. J. A. Kilner, R. A. DeSouza and I. C. Fullarton, *Solid State Ionics*, 1996, **86-8**, 703-709.
32. J. M. D. Tascon and L. G. Tejuca, *Reaction Kinetics and Catalysis Letters*, 1980, **15**, 185-191.
33. H. Takahashi, F. Munakata and M. Yamanaka, *Physical Review B*, 1998, **57**, 15211-15218.
34. L. W. Tai, M. M. Nasrallah, H. U. Anderson, D. M. Sparlin and S. R. Sehlin, *Solid State Ionics*, 1995, **76**, 273-283.
35. L. W. Tai, M. M. Nasrallah, H. U. Anderson, D. M. Sparlin and S. R. Sehlin, *Solid State Ionics*, 1995, **76**, 259-271.
36. E. Girdauskaite, H. Ullmann, M. Al Daroukh, V. Vashook, M. Bulow and U. Guth, *Journal of Solid State Electrochemistry*, 2007, **11**, 469-477.
37. Y. Teraoka, H. M. Zhang, S. Furukawa and N. Yamazoe, *Chemistry Letters*, 1985, 1743-1746.
38. S. P. Simner, M. D. Anderson, M. H. Engelhard and J. W. Stevenson, *Electrochemical and Solid State Letters*, 2006, **9**, A478-A481.

39. J. Y. Kim, V. L. Sprenkle, N. L. Canfield, K. D. Meinhardt and L. A. Chick, *Journal of the Electrochemical Society*, 2006, **153**, A880-A886.
40. J. W. Fergus, *International Journal of Hydrogen Energy*, 2007, **32**, 3664-3671.
41. C. Sun, R. Hui and J. Roller, *Journal of Solid State Electrochemistry*, 2009.
42. R. A. De Souza and J. A. Kilner, *Solid State Ionics*, 1999, **126**, 153-161.
43. J. Larminie and A. Dicks, *Fuel Cell Systems Explained* John Wiley and Sons, 2003.
44. Y. Takeda, R. Kanno, M. Noda, Y. Tomida and O. Yamamoto, *Journal of the Electrochemical Society*, 1987, **134**, 2656-2661.
45. J. W. Stevenson, T. R. Armstrong, R. D. Carneim, L. R. Pederson and W. J. Weber, *Journal of the Electrochemical Society*, 1996, **143**, 2722-2729.
46. M. W. den Otter, L. M. van der Haar and H. J. M. Bouwmeester, *Solid State Ionics*, 2000, **134**, 259-264.
47. S. Wang, P. A. W. van der Heide, C. Chavez, A. J. Jacobson and S. B. Adler, *Solid State Ionics*, 2003, **156**, 201-208.
48. J. A. Lane and J. A. Kilner, *Solid State Ionics*, 2000, **136**, 997-1001.
49. R. Ganeshanathan and A. V. Virkar, *Journal of the Electrochemical Society*, 2006, **153**, A2181-A2187.
50. J. Crank, *Mathematics of diffusion*, Oxford University Press, London, 1956.
51. R. A. De Souza and J. A. Kilner, *Solid State Ionics*, 1998, **106**, 175-187.
52. H. J. M. Bouwmeester, M. W. Den Otter and B. A. Boukamp, *Journal of Solid State Electrochemistry*, 2004, **8**, 599-605.
53. J. Maier, *Physical Chemistry of Ionic Materials* Wiley, West Sussex, 2004.
54. C. C. Kan and E. D. Wachsman, *Journal of the Electrochemical Society*, 2009, **156**, B695-B702.
55. J. Nowotny, T. Bak, M. K. Nowotny and C. C. Sorrell, *Advances in Applied Ceramics*, 2005, **104**, 147-153.
56. M. Thompson, M. D. Baker, A. Christie and J. F. Tyson, *Auger Electron Spectroscopy*, John Wiley and Sons, Newyork, 1985.
57. G. E. Mcguire, *Auger Electron Spectroscopy Reference Manual*, Plenum, New York, 1979.

58. J. Goldstein, D. Newbury, D. Joy, C. Lyman, P. Echlin, E. Lifshin, L. Sawyer and J. Michael, *Scanning Electron Microscopy and X-ray Microanalysis* Springer, New York, 2003.
59. E. Bucher and W. Sitte, *Solid State Ionics*, 2010.
60. P. A. W. v. d. Heide, *SURFACE AND INTERFACE ANALYSIS*, 2002, **33**, 414–425.
61. M. M. Viitanen, R. G. von Welzenis, H. H. Brongersma and F. P. F. van Berkel, *Solid State Ionics*, 2002, **150**, 223-228.
62. V. E. Henrich, *Reports on Progress in Physics*, 1985, **48**, 1481-1541.
63. D. A. Porter and K. E. Eastering, *Phase Transformations in Metals and Alloys*, CRC press, FL, 1992.
64. B. Rahmati, J. Fleig, W. Sigle, E. Bischoff, J. Maier and M. Ruhle, *Surface Science*, 2005, **595**, 115-126.
65. R. Meyer, R. Waser, J. Helmbold and G. Borchardt, *Journal of Electroceramics*, 2002, **9**, 103-112.
66. K. Gomann, G. Borchardt, A. Gunhold, W. Maus-Friedrichs and H. Baumann, *Physical Chemistry Chemical Physics*, 2004, **6**, 3639-3644.
67. Y. L. Wang, K. Duncan, E. D. Wachsman and F. Ebrahimi, *Solid State Ionics*, 2007, **178**, 53-58.
68. K. Szot, M. Pawelczyk, J. Herion, C. Freiburg, J. Albers, R. Waser, J. Hulliger, J. Kwapulinski and J. Dec, *Applied Physics a-Materials Science & Processing*, 1996, **62**, 335-343.
69. H. Tanaka and M. Misono, *Current Opinion in Solid State & Materials Science*, 2001, **5**, 381-387.
70. L. C. Dufour, G. L. Bertrand, G. Caboche, P. Decorse, A. El Anssari, A. Poirson and M. Vareille, *Solid State Ionics*, 1997, **101**, 661-666.
71. S. N. Ruddlesden and P. Popper, *Acta Crystallographica*, 1957, **10**, 538-540.
72. M. Konigstein and C. R. A. Catlow, *Journal of Solid State Chemistry*, 1998, **140**, 103-115.
73. F. Tietz, A. Mai and D. Stover, *Solid State Ionics*, 2008, **179**, 1509-1515.
74. W. D. Copeland and R. A. Swalin, *Journal of Physics and Chemistry of Solids*, 1968, **29**, 313-&.

75. E. P. Murray, M. J. Sever and S. A. Barnett, *Solid State Ionics*, 2002, **148**, 27-34.
76. H. J. Hwang, M. B. Ji-Woong, L. A. Seunghun and E. A. Lee, *Journal of Power Sources*, 2005, **145**, 243-248.
77. F. Qiang, K. N. Sun, N. Q. Zhang, X. D. Zhu, S. R. Le and D. R. Zhou, *Journal of Power Sources*, 2007, **168**, 338-345.
78. H. Y. Jung, K. S. Hong, H. G. Jung, H. Kim, H. R. Kim, J. W. Son, J. Kim, H. W. Lee and J. H. Lee, *Journal of the Electrochemical Society*, 2007, **154**, B480-B485.
79. V. A. C. Haanappel, A. Mai and J. Mertens, *Solid State Ionics*, 2006, **177**, 2033-2037.
80. M. Sahibzada, S. J. Benson, R. A. Rudkin and J. A. Kilner, *Solid State Ionics*, 1998, **115**, 285-290.
81. S. P. Simner, J. R. Bonnett, N. L. Canfield, K. D. Meinhardt, J. P. Shelton, V. L. Sprengle and J. W. Stevenson, *Journal of Power Sources*, 2003, **113**, 1-10.
82. H. Uchida, S. Arisaka and M. Watanabe, *Solid State Ionics*, 2000, **135**, 347-351.
83. K. Yamahara, C. P. Jacobson, S. J. Visco, X. F. Zhang and L. C. de Jonghe, *Solid State Ionics*, 2005, **176**, 275-279.
84. D. Oh, D. Gostovic and E. D. Wachsman, *In preparation*, 2010.
85. A. A. Vance and S. McIntosh, *Journal of the Electrochemical Society*, 2008, **155**, B1-B7.
86. Y. K. Lee, J. Y. Kim, Y. K. Lee, I. Kim, H. S. Moon, J. W. Park, C. P. Jacobson and S. J. Visco, *Journal of Power Sources*, 2003, **115**, 219-228.
87. J. M. Serra, V. B. Vert, M. Betz, V. A. C. Haanappel, W. A. Meulenbergh and F. Tietz, *Journal of the Electrochemical Society*, 2008, **155**, B207-B214.
88. M. A. Pena and J. L. G. Fierro, *Chemical Reviews*, 2001, **101**, 1981-2017.
89. F. S. Baumann, J. Fleig, H. U. Habermeier and J. Maier, *Solid State Ionics*, 2006, **177**, 1071-1081.
90. M. J. L. Ostergard and M. Mogensen, *Electrochimica Acta*, 1993, **38**, 2015-2020.
91. A. Esquirol, N. P. Brandon, J. A. Kilner and M. Mogensen, *Journal of the Electrochemical Society*, 2004, **151**, A1847-A1855.
92. J. W. N. I. Chorkendorff, *Concepts of Modern Catalysis and Kinetics*, WILEY-VCH, 2003.

93. N. Miura, Y. Okamoto, J. Tamaki, K. Morinaga and N. Yamazoe, *Solid State Ionics*, 1995, **79**, 195-200.
94. J. A. Lane, S. J. Benson, D. Waller and J. A. Kilner, *Solid State Ionics*, 1999, **121**, 201-208.
95. J. Maier, *Solid State Ionics*, 1998, **112**, 197-228.
96. X. Montero, F. Tietz, D. Stover, M. Cassir and I. Villarreal, *Corrosion Science*, 2009, **51**, 110-118.
97. X. Montero, F. Tietz, D. Stover, M. Cassir and I. Villarreal, *Journal of Power Sources*, 2009, **188**, 148-155.
98. W. Z. Zhu and S. C. Deevi, *Materials Research Bulletin*, 2003, **38**, 957-972.
99. E. Konyshева, H. Penkalla, E. Wessel, J. Mertens, U. Seeling, L. Singheiser and K. Hilpert, *Journal of the Electrochemical Society*, 2006, **153**, A765-A773.
100. S. Taniguchi, M. Kadowaki, H. Kawamura, T. Yasuo, Y. Akiyama, Y. Miyake and T. Saitoh, *Journal of Power Sources*, 1995, **55**, 73-79.
101. S. P. Simner, M. D. Anderson, G. G. Xia, Z. Yang, L. R. Pederson and J. W. Stevenson, *Journal of the Electrochemical Society*, 2005, **152**, A740-A745.
102. S. G. Li, N. P. Xu, J. Shi, M. Z. C. Hu and E. A. Payzant, *Journal of Materials Science Letters*, 2001, **20**, 1631-1633.
103. D. Oh, D. Gostovic and E. Wachsman, *to be submitted for publication*.
104. S. P. Jiang, S. Zhang and Y. D. Zhen, *Journal of the Electrochemical Society*, 2006, **153**, A127-A134.
105. Ohbayash.H, T. Kudo and T. Gejo, *Japanese Journal of Applied Physics*, 1974, **13**, 1-7.
106. D. Waller, J. A. Lane, J. A. Kilner and B. C. H. Steele, *Materials Letters*, 1996, **27**, 225-228.
107. K. H. Kim, S. H. Lee and J. S. Choi, *Journal of Physics and Chemistry of Solids*, 1985, **46**, 331-338.
108. G. C. Kostogloudis and C. Ftikos, *Solid State Ionics*, 1999, **126**, 143-151.
109. D. Oh, E. Armstrong, D. Jung, J. Yoo and E. Wachsman, *to be submitted for publication*.
110. H. Yokokawa, T. Horita, N. Sakai, K. Yamaji, M. E. Brito, Y. P. Xiong and H. Kishimoto, *Solid State Ionics*, 2006, **177**, 3193-3198.

111. M. C. Tucker, H. Kurokawa, C. P. Jacobson, L. C. De Jonghe and S. J. Visco, *Journal of Power Sources*, 2006, **160**, 130-138.
112. I. H. Jung, *Solid State Ionics*, 2006, **177**, 765-777.
113. E. Povoden, A. N. Grundy and L. J. Gauckler, *International Journal of Materials Research*, 2006, **97**, 569-578.
114. S. P. Jiang, J. P. Zhang, L. Apateanu and K. Foger, *Journal of the Electrochemical Society*, 2000, **147**, 4013-4022.
115. S. P. Jiang, *Journal of Materials Science*, 2008, **43**, 6799-6833.
116. J. A. M. Vanroosmalen and E. H. P. Cordfunke, *Journal of Solid State Chemistry*, 1994, **110**, 109-112.
117. S. Piskunov, E. Spohr, T. Jacob, E. A. Kotomin and D. E. Ellis, *Physical Review B*, 2007, **76**, -.
118. Y. Matsuzaki and I. Yasuda, *Journal of the Electrochemical Society*, 2001, **148**, A126-A131.
119. M. Backhaus-Ricoult, *Solid State Ionics*, 2006, **177**, 2195-2200.
120. S. R. Bishop, K. L. Duncan and E. D. Wachsman, *Journal of the Electrochemical Society*, 2009, **156**, B1242-B1248.
121. K. Hilpert, D. Das, M. Miller, D. H. Peck and R. Weiss, *Journal of the Electrochemical Society*, 1996, **143**, 3642-3647.
122. Y. F. Chang, G. A. Somorjai and H. Heinemann, *Journal of Catalysis*, 1995, **154**, 24-32.
123. P. Decorse, G. Caboche and L. C. Dufour, *Solid State Ionics*, 1999, **117**, 161-169.
124. M. Shimada, H. Kokawa, Z. J. Wang, Y. S. Sato and I. Karibe, *Acta Materialia*, 2002, **50**, 2331-2341.
125. A. Mai, V. A. C. Haanappel, S. Uhlenbruck, F. Tietz and D. Stover, *Solid State Ionics*, 2005, **176**, 1341-1350.
126. H. Flood and T. Forland, *Acta Chemica Scandinavica*, 1947, **1**, 592-604.
127. M. W. den Otter, H. J. M. Bouwmeester, B. A. Boukamp and H. Verweij, *Journal of the Electrochemical Society*, 2001, **148**, J1-J6.
128. P. Trambouze, H. V. Landeghem and J.-P. Wauquier, Editions Technip, Paris, 1988.

129. G. Kim, S. Wang, A. J. Jacobson and C. L. Chen, *Solid State Ionics*, 2006, **177**, 1461-1467.
130. R. Ganeshanathan and A. V. Virkar, *Journal of the Electrochemical Society*, 2005, **152**, A1620-A1628.
131. J. Nowotny, T. Bak and C. C. Sorrell, *Advances in Applied Ceramics*, 2005, **104**, 174-180.
132. T. Ramos and A. Atkinson, *Solid State Ionics*, 2004, **170**, 275-286.
133. X. Chen, S. Wang, Y. L. Yang, L. Smith, N. J. Wu, B. I. Kim, S. S. Perry, A. J. Jacobson and A. Ignatiev, *Solid State Ionics*, 2002, **146**, 405-413.

BIOGRAPHICAL SKETCH

Dongjo Oh, as also known as DJ, was born in Haenam, South Korea and moved to Incheon at 5 years old. From very young ages, he liked a robot animation and so wanted to be a scientist. He graduated Bu-pyung elementary school, Bu-pyung seo middle school, and Bu-kwang high school. After he entered Inha University in Incheon and majored materials science and engineering. He voluntarily worked as undergraduate research assistance from sophomore and participated in lots of activity in the university. And he started military service from Oct. 2000 to Dec. 2002 as a KATUSA (Korean Augmentation to U.S. Army). In the army he learned leadership and professionalism. During that period, he wished to study abroad. After finishing the army service he prepared TOEFL and GRE during the senior and applied materials science and engineering program in the University of Florida. While at UF his knowledge on basic material science was improved significantly. In Dec 2008, Chanyoung Yun and DJ became a family and Michelle was born in Sep. 2009. Life in U.S. brought him not only scientific knowledge but also confidence. He is not fully fledged but ready to come true his dream of young ages. He always appreciates Jesus for giving this chance.